

**UNIVERSITÀ DEGLI STUDI DI NAPOLI
“FEDERICO II”**



Scuola Politecnica e delle Scienze di Base

Area Didattica di Scienze Matematiche Fisiche e Naturali

Dipartimento di Fisica “Ettore Pancini”

Laurea Magistrale in Fisica

**Characterization of a Triple-GEM detector prototype for
the CMS Muon System Upgrade**

*Caratterizzazione di un prototipo di rivelatore Triple-GEM per l’Upgrade del Sistema
Muonico di CMS*

Relatori:

Prof. Alberto Orso Maria Iorio
Dott. Biagio Rossi

Candidato:

Oriana D’Angola
Matr. N94000442

Anno Accademico 2020/2021

*Questo secolo oramai alla fine,
saturato di parassiti senza dignità,
mi spinge solo ad essere migliore,
con più volontà.*

*Emanciparmi dall'incubo delle passioni,
cercare l'Uno al di sopra del Bene e del Male,
essere un'immagine divina,
di questa realtà.*

— *F. Battiato, E ti vengo a cercare, Fisiognomica, 1988*

Contents

1	The Standard Model of Elementary Particle	9
1.1	Introduction	9
1.2	Elementary Particles	10
1.3	The Quantum Field Theory	12
1.3.1	Global and local invariance of the Lagrangian under $U(1)$	13
1.3.2	Local invariance of the Lagrangian under $SU(N)$	15
1.4	The Standard Model	16
1.4.1	The Electroweak Theory	17
1.4.2	Quantum Chromodynamics (QCD)	19
1.4.3	The Brout–Englert–Higgs mechanism	21
1.4.4	Fermions masses	24
1.5	Unsolved issues in the Standard Model	25
2	CMS experiment at LHC, CERN	27
2.1	Introduction	27
2.2	The Large Hadron Collider	27
2.2.1	Luminosity	30
2.2.2	LHC experiments and data taking activity	31
2.3	The CMS experiment	32
2.3.1	The coordinate frame at CMS	34
2.3.2	The CMS sub-detector layout	36
2.4	Muon system upgrade with Triple-GEM detectors	42
2.4.1	Improvement of the L1 muon trigger rate	45
2.4.2	Radiation Tolerance: background nature and rates	46
2.4.3	Muon reconstruction and identification	48
3	Gaseous Detector and CMS Triple-GEM detector systems	53
3.1	Introduction	53
3.2	Passage of Radiation Through Matter	53
3.2.1	Interaction of charged particles with matter: the Bethe-Bloch formula	54
3.2.2	Interaction of photons with matter	55
3.3	Gaseous Ionization Detectors	58
3.3.1	Ionization and Transport Phenomena in Gases	61
3.3.2	Charge amplification	64
3.4	The Gas Electron Multiplier	65

3.4.1	Basic Operating Principle	66
3.4.2	Triple-GEM detector	68
3.4.3	Gain of a Triple-GEM detector	70
3.4.4	Timing Resolution	71
3.5	Common features of CMS Triple-GEM detector systems	71
3.5.1	Readout Methods	72
3.5.2	Pulse Formation and Shape	74
3.5.3	Physics performances	74
4	PICO: a high voltage seven independent channel pico-ammeter	79
4.1	Description of the device	79
4.1.1	The internal and external structure of PICO	80
4.2	Characterization of PICO	81
4.2.1	Electronic noise of PICO	85
4.2.2	Evaluation of the resolution and of the thermal dependence of the output current	86
4.2.3	Evaluation of the resolution and of the thermal dependence of the output voltage	90
5	Characterization of a Triple-GEM detector	97
5.1	Experimental Setup	97
5.2	Triple-GEM detector prototype: main features	100
5.3	Optimization of Electric Field	104
5.4	Current voltage curve for GE1, GE2, GE3	106
5.5	Uniformity gain measurements	109
5.6	Calibration of Charge Sensitive Pre-Amplifier	113
5.7	Gain Curve of GE3 of the Triple-GEM detector prototype	116
	Bibliography	123

Introduction

The Standard Model of Particle Physics, currently, represent man's elegant and consistent effort supported by experimental evidence to address the question of what the universe is formed from. The main achievement of the Standard Model is the description of the interactions between fundamental particles and likewise the prediction of the particles to be searched for. The predictions of the SM, including all its particles as well as their properties, have been tested extensively during the years by experimental particle physics. Among the most important tools for such tests are the particle accelerators, machines able to accelerate elementary particles, like electrons, or composite particles, like protons, to collimate them into beams, and to collide them against fixed target or other beams. The Large Hadron Collider (LHC) is the most powerful particle accelerator ever built and it is designed to provide proton-proton collisions with a center-of-mass energy of 14 TeV. To extend the sensitivity for new physics searches, a major upgrade of the LHC has been decided and is being prepared, the High Luminosity LHC (HL-LHC). In order to meet the research needs of new physics, in this innovative and avant-garde context, changes are made to the detectors that constitute the main experiments at LHC. The Compact Muon Solenoid (CMS) experiment is one of the four great experiments at the LHC. Its main goals are to provide measurements at the TeV energy scale for the Standard Model, such as high precision tests of QCD, flavour physics, electroweak interactions, and the Higgs boson properties, and to explore potential new physics beyond the Standard Model.

One of the most important upgrades of the CMS detector interested the Muon System and it was designed to improve the muon trigger and tracking performance in the prospected high luminosity environment. The HL-LHC, in fact, will increase the projected integrated luminosity of 300 fb^{-1} by an order of magnitude, up to 3000 fb^{-1} in the coming two decades. After the phase II HL-LHC upgrade, the collision rate and the background rate will significantly increase particularly in the region close to the beam, the so called *forward region*. Consequently, additional muon detectors in the forward region are installed to increase redundancy and enhance the trigger and reconstruction capabilities. The technology chosen for the upgrade is that of the Micro Pattern Gaseous Detectors, and specifically the Gaseous Electron Multiplier or, more briefly, GEM. An unique feature of GEM devices is that, with an appropriate choice of the fields, the fraction of amplified electrons transferring to the gas gap following a first electrode can be injected and multiplied in a second foil, and yet again in a cascade of GEM electrodes. The noticeable advantage of multiple foils is that the overall gain needed for detection can be attained with each of the electrodes operated at a much lower voltage with respect to what would be needed by adopting a single stage of amplification, therefore such configuration is much less prone to discharges. This is the key feature of Triple-GEM detectors.

The Triple-GEM detectors deployed in the phase I upgrade of the CMS Muon Sys-

tem constitute a novel state-of-the-art technology that will require careful commissioning and dedicated studies. A precise monitoring of the currents through the three GEM foils in particular would allow an in-depth understanding of the gain of the chamber, and potentially allow to diagnose issues like electric discharges that might cause the chamber to malfunction. A suitable tool for carrying out such measurements is the multi-channel pico-ammeter.

In this work, the resolution of a multichannel pico-ammeter, named PICO, specifically developed for this task, was determined. The pico-ammeter was then employed to characterize in detail the Triple-GEM prototype for the CMS Muon System.

This work is organized as follows:

- In **Chapter 1** a brief introduction of the Standard Model and its main characteristics as well as the intrinsic limitations of the model is discussed.
- In **Chapter 2** the Large Hadron Collider and one of its 4 fundamental experiments are shown: the CMS experiment. The reasons and the fundamental characteristics of the Muon System Upgrade are also outlined.
- In **Chapter 3** an overview of the gas detectors and, in particular, of the Triple-GEM detectors is carried.
- In **Chapter 4** corrective factors have been derived as well as the voltage and current resolution of PICO.
- In **Chapter 5** the characterization of the Triple-GEM prototype is explained: the procedure for optimizing the electric fields inside the detector is then described. Considerations are made on the gain and its uniformity over the whole sensitive area of the Triple-GEM prototype.

Chapter 1

The Standard Model of Elementary Particle

1.1 Introduction

The Standard Model of Particle Physics, currently, represent man's elegant and consistent effort supported by experimental evidence to address the question of what the universe is formed from. The discovery of the atom paved the way for the concept of elementary particles as being the apparently structure-less fundamental units forming the universe. Investigating the nature of such particles does not merely imply some sort of basic classification; on the contrary, it is inevitably tied to the study of particles mutual interactions, occurring via the fundamental forces. Four of such forces are currently believed to exist:

- gravitation, whose theoretical formulation was given by Isaac Newton, in its classical form and, later, by Albert Einstein for General Relativity;
- electromagnetism, described in its classical form by James Clerk Maxwell's and by Richard Feynman's theories in quantum environment;
- the strong and the weak interactions, firstly described by Hideki Yukawa and Enrico Fermi's models, respectively.

While both gravitational and electromagnetic forces have a long enough interaction range to allow us to experience their direct effects at macroscopic scale, the strong and the weak forces exert their influence over very short distances and are therefore mainly involved in nuclear and sub-nuclear phenomenology. Pursuing the idea of a unified theory, physicists have made remarkable progress in finding similarities between three of the fundamental forces, so that nowadays the electromagnetic, the strong, and the weak interactions can be described through the same mathematical framework, that is Quantum Field Theory (QFT). More specifically, the form and the properties of interactions arise from requiring as valid *the principle of local gauge invariance*, which means that the equations describing particle physics phenomena keep the same form after applying a specific transformation to the particle fields, which dictates the properties of particles interactions. The Standard Model (SM) of the strong, weak and electromagnetic interactions is the simplest realization of such principle. Despite actually not providing a full unification to the three fundamental interactions it is involved with and despite gravitation being completely excluded

from the picture, the Standard Model has successfully predicted the existence of many particles, including the massive gauge bosons, Z and W, alongside with the Higgs boson, whose observation has confirmed the Standard Model to be a self-consistent theory.

1.2 Elementary Particles

The Standard Model treats both matter and force fields with the same formalism, since interactions are themselves regarded as mediated by particles. Each particle is described by a set of quantum numbers, often referred to as internal, since they do not deal with the kinematic state of the particle itself. The whole set of elementary particles can be split into two fundamental categories, according to a quantum number called spin, whose value shall be from now on expressed in units of Planck's constant \hbar :

- fermions, particles whose spin is a semi-integer number and which obey the Fermi-Dirac statistics;
- bosons, particles whose spin is an integer number and which obey the Bose-Einstein statistics.

Standard Model of Elementary Particles

	three generations of matter (elementary fermions)			three generations of antimatter (elementary antifermions)			interactions / force carriers (elementary bosons)		
	I	II	III	I	II	III			
mass	$\approx 2.2 \text{ MeV}/c^2$	$\approx 1.28 \text{ GeV}/c^2$	$\approx 173.1 \text{ GeV}/c^2$	$\approx 2.2 \text{ MeV}/c^2$	$\approx 1.28 \text{ GeV}/c^2$	$\approx 173.1 \text{ GeV}/c^2$	0	0	$124.97 \text{ GeV}/c^2$
charge	$\frac{2}{3}$	$\frac{2}{3}$	$\frac{2}{3}$	$-\frac{2}{3}$	$-\frac{2}{3}$	$-\frac{2}{3}$	0	0	0
spin	$\frac{1}{2}$	$\frac{1}{2}$	$\frac{1}{2}$	$\frac{1}{2}$	$\frac{1}{2}$	$\frac{1}{2}$	0	0	0
	u up	c charm	t top	\bar{u} antiup	\bar{c} anticharm	\bar{t} antitop	g gluon		H higgs
QUARKS	d down	s strange	b bottom	\bar{d} antidown	\bar{s} antistrange	\bar{b} antibottom	γ photon		
	$\approx 4.7 \text{ MeV}/c^2$	$\approx 96 \text{ MeV}/c^2$	$\approx 4.18 \text{ GeV}/c^2$	$\approx 4.7 \text{ MeV}/c^2$	$\approx 96 \text{ MeV}/c^2$	$\approx 4.18 \text{ GeV}/c^2$	0		
	$-\frac{1}{3}$	$-\frac{1}{3}$	$-\frac{1}{3}$	$\frac{1}{3}$	$\frac{1}{3}$	$\frac{1}{3}$	0		
	$\frac{1}{2}$	$\frac{1}{2}$	$\frac{1}{2}$	$\frac{1}{2}$	$\frac{1}{2}$	$\frac{1}{2}$	1		
	e electron	μ muon	τ tau	e^+ positron	$\bar{\mu}$ antimuon	$\bar{\tau}$ antitau	Z Z ⁰ boson		
LEPTONS	$\approx 0.511 \text{ MeV}/c^2$	$\approx 105.66 \text{ MeV}/c^2$	$\approx 1.7768 \text{ GeV}/c^2$	$\approx 0.511 \text{ MeV}/c^2$	$\approx 105.66 \text{ MeV}/c^2$	$\approx 1.7768 \text{ GeV}/c^2$	$\approx 91.19 \text{ GeV}/c^2$		
	-1	-1	-1	1	1	1	0		
	$\frac{1}{2}$	$\frac{1}{2}$	$\frac{1}{2}$	$\frac{1}{2}$	$\frac{1}{2}$	$\frac{1}{2}$	1		
	ν_e electron neutrino	ν_μ muon neutrino	ν_τ tau neutrino	$\bar{\nu}_e$ electron antineutrino	$\bar{\nu}_\mu$ muon antineutrino	$\bar{\nu}_\tau$ tau antineutrino	W^+ W ⁺ boson		W W boson
	$< 0.17 \text{ eV}/c^2$	$< 0.17 \text{ MeV}/c^2$	$< 18.2 \text{ MeV}/c^2$	$< 0.17 \text{ eV}/c^2$	$< 0.17 \text{ MeV}/c^2$	$< 18.2 \text{ MeV}/c^2$	$\approx 80.39 \text{ GeV}/c^2$		$\approx 80.39 \text{ GeV}/c^2$
	0	0	0	0	0	0	1		-1
	$\frac{1}{2}$	$\frac{1}{2}$	$\frac{1}{2}$	$\frac{1}{2}$	$\frac{1}{2}$	$\frac{1}{2}$	1		1

GAUGE BOSONS VECTOR BOSONS **SCALAR BOSONS**

Figure 1.1: The elementary particles and antiparticles, divided into quarks, leptons and, force-carrying, together with the scalar Higgs boson.

Fundamental fermions in the Standard Model are categorised as either quarks or leptons, which are divided into three families with different properties. Each family, or generation, is a doublet of particles associated to an isospin quantum number. Leptons are composed by three massive electric charged particles and three massless neutral ones. Leptons take part to electromagnetic and weak interactions but not to the strong one. As a general rule, to every particle corresponds a so-called antiparticle, a copy which differs only in the sign of its quantum numbers, first of all, the electric charge. In some cases, the particle cannot be distinguished from its antiparticle. In figure 1.1 a schematic illustration of Standard Model of Elementary Particles is given.

Matter is known to be made up of atoms: the atom is the result of negatively charged

electrons (e^-) being bound to positively charged nuclei by the electromagnetic force, which is a low-energy manifestation of Quantum Electrodynamics (QED). Both electrons and nuclei are capable of interacting electromagnetically as a result of their electric charge that is -1 for the electron and $+1$ for the proton in units of the elementary charge $e \simeq 1.6 \times 10^{-19} \text{C}$. Electrons are fermions with $s = \frac{1}{2}$ and belong to the lepton class. The nuclei are themselves a composite state of particles, protons and neutrons, held together by the nuclear strong force, the latter being a large manifestation at the nuclear distance scale of Quantum Chromodynamics (QCD). Looking at even smaller scales, protons and neutrons are found to be formed from half-spin fermions called quarks of type up and down. The notion of what an elementary particle has changed over the years as smaller and smaller distances have been accessed thanks to new technologies, which increased the power to investigate the internal structure of matter. More precisely, the higher the energy of the probe particle is, the smaller is the wavelength associated to the latter and, consequently, the resolution obtained in the measure. At the smallest distances currently probed by the highest-energy accelerators, leptons and quarks seem not to exhibit further internal structure: as far as we know, the world around us is entirely made of half-spin fermions, namely leptons and quarks, interacting via the electromagnetic and the strong forces.

In contrast to the strong force, the weak force is not intense enough to hold different particles together to produce bound states, i.e. matter particles; it is mainly involved in radioactive decays and nuclear fusion. Nevertheless, the weak force plays a crucial role in the Standard Model, appearing to be partially unified to the electromagnetic one in what is called electroweak force. In processes involving the weak force, another lepton is often produced: the neutrino (ν). The electron, together with the corresponding electronic neutrino (ν_e), belongs to a so-called lepton doublet. There exist three families, or generations, of lepton doublets: the first one is indeed composed of the electron and its neutrino, while the muon (μ^-) and the tau (τ^-) leptons, together with their own neutrinos (ν_μ and ν_τ), belong to the second and third generation, respectively. The masses of the charged leptons, whose electric charge is -1 , increase from the first to the last generation, whereas all neutrinos are nearly mass-less. It should be noted, however, that in the SM formalism, neutrinos are strictly massless, but the neutrino oscillation¹ is proof that they have mass. Neutrinos are also electrically neutral, therefore they can only interact via the weak force. Leptons and anti-leptons are respectively assigned a lepton number $L = 1$ and $L = -1$. In order not to be forbidden, a physical reaction must always ensure that the total lepton number equals zero. Each lepton doublet is also given a so-called family lepton number $L_l = 1$, with $l = e; \mu; \tau$ ($L_l = -1$ for anti-leptons), which empirically appears to be always conserved in physical processes. Lepton doublets participate in the arrangement of fermions generations together with quarks. Quarks are half-spin fermions, they can interact electromagnetically, as they carry fractional electric charges, strongly and weakly. They are organized into doublets, similarly to leptons, and each doublet containing a particle with an electric charge of $+\frac{2}{3}$ and a particle with an electric charge of $-\frac{1}{3}$: we have the up-quark and the down-quark (u and d) for the first generation, the charm-quark and

¹First predicted by Bruno Pontecorvo in 1957, neutrino oscillation has since been observed by a multitude of experiments in several different contexts and consist in a quantum mechanical phenomenon in which a neutrino created with a specific lepton family number can later be measured to have a different lepton family number.

the strange-quark (c and s) for the second generation, and the top-quark and the bottom- (or beauty-) quark (t and b) for the third generation. Quarks are given a baryon number $B = \frac{1}{3}$ ($B = -\frac{1}{3}$ for anti-quarks) to account for the experimental fact that they are only found within composite hadrons. The most abundant types of hadrons are composite states of three and two quarks. The former are named baryons, identified by $B = 1$ and an integer electric charge. Two quark states are made up by a pair of quark-antiquark, not necessarily of the same type, they are mesons, identified by $B = 0$ and an integer electric charge.

In modern particle physics, each force is described by a Quantum Field Theory and the interaction between charged particles are mediated by spin-1 force-carrying particles, also known as gauge bosons. The QFT on which electromagnetism is based is the Quantum Electrodynamics (QED) and the interaction is described by the exchange of a virtual photon, the gauge boson of the QED. In the case of strong interactions, the corresponding theory is called Quantum Chromodynamics (QCD) and the gauge bosons are called gluons which, like the photon, are massless. The weak charged-current interaction is mediated by the charged W^+ and W^- bosons, approximately eighty times more massive than the proton. There is also a weak neutral-current interaction, mediated by the electrically neutral Z boson. The final element of the Standard Model is the Higgs boson H. It plays a special role in the Standard Model because it is responsible of the bosons and fermions mass. It is a spin-0 particle, differently from the spin-half fermions and spin-1 bosons, and it is the quantum of the only one scalar field predicted in the Standard Model. The Higgs boson has been discovered by ATLAS and CMS experiments in 2012. This discovery earned Higgs and Englert the Nobel Prize in Physics in 2013 for the theoretical discovery of a mechanism that contributes to our understanding of the origin of mass of subatomic particles.

1.3 The Quantum Field Theory

The SM as a theoretical framework is, as mentioned in the previous Section 1.2, a quantum field theory in which the elementary particles are the quanta of fields. The rationale behind the formulation of a Quantum Field Theory of the interaction use a local gauge invariance principle: it can be shown that local gauge invariance is never possible for a free field theory but only for a theory of interacting fields. Therefore the gauge local invariance can be assumed as a principle for the development of gauge theories. Starting from free Lagrangians, the interaction will always be introduced through the request of local gauge invariance. The first step to build a quantum field theory is the quantization of the fields; this means that the field operators, that are functions of the space-time coordinates, are written as linear combination of operators that create or destroy a particle acting on a state vector of the system. These operators obey to the dynamical equation descending from a Lagrangian L by a variational principle. In quantum fields theory L is usually written as an integral over the space coordinates of a Lagrangian density \mathcal{L} . It is a function of the fields and of their gradients. The dynamical equations for the fields are obtained from the Euler-Lagrange equations for the Lagrangian density that came from the application of a variational principle. The interactions among the fields are introduced requiring an invariance of the theory under a local gauge symmetry group; starting from the Lagrangian \mathcal{L}_0 for the free fields, the request of the invariance for the total Lagrangian

\mathcal{L} produces the interaction term \mathcal{L}' :

$$\mathcal{L} = \mathcal{L}_0 + \mathcal{L}' \quad (1.1)$$

The construction of the Standard Model is based on a symmetry principle since the gauge invariance guarantees the renormalizability of the theory.

1.3.1 Global and local invariance of the Lagrangian under $U(1)$

Before going on through the description of the Higgs mechanism it is necessarily to introduce some local invariance concepts. A Lagrangian of a physical system can be invariant under a global transformation, in the sense that all fields simultaneously transform in a way that leads the Lagrangian to be unchanged. For example we can consider the Lagrangian of a non-interactive charged fermion, i.e. the Dirac Lagrangian:

$$\mathcal{L}_0 = i\bar{\psi}\gamma^\mu\partial_\mu\psi - m\bar{\psi}\psi \quad (1.2)$$

where:

$$\bar{\psi} = \psi^\dagger\gamma^0 \quad (1.3)$$

and γ^μ are the Dirac matrix, acting on the space 4×4 of the Dirac spinors, satisfying the anticommutation algebra rules:

$$\{\gamma^\mu, \gamma^\nu\} = \gamma^\mu\gamma^\nu + \gamma^\nu\gamma^\mu = 2g^{\mu\nu} \quad (1.4)$$

where $g^{\mu\nu}$ is the metric tensor. This Lagrangian is invariant under global phase transformation, forming the group $U(1)$:

$$\psi(x) \rightarrow \psi'(x) = e^{iq\theta}\psi(x) \quad (1.5)$$

$$\bar{\psi}(x) \rightarrow \bar{\psi}'(x) = e^{-iq\theta}\bar{\psi}(x).^2 \quad (1.6)$$

The study of the invariance properties of the Lagrangian yields to the identification of conserved quantities for the well-known Noether Theorem: this is a great advantage of the Lagrangian formulation. The global invariance under $U(1)$ guarantees the existence of a conserved current, the electromagnetic current, satisfying a conservation law:

$$\partial_\mu(q\bar{\psi}\gamma^\mu\psi) - \partial_\mu j^\mu = 0 \quad (1.7)$$

where j^μ is the quadri-current in the relativistic formalism. Since the electromagnetic charge can be written in terms of the the first component of the quadri-vector j^μ :

$$q = \int j^0 d^3x \quad (1.8)$$

and, from 1.7, we can obtain:

$$\partial_0 j^0 = -\partial_i j^i \quad (1.9)$$

²The set of all possible transformations of the kind 1.5 and 1.6, considering all possible values of θ , forms an Abelian Lie group called $U(1)$: it consists of unitary transformations and it is mono-dimensional.

that leads to:

$$\frac{dq}{dt} = - \int_V \partial_i j^i d^3x = - \int_S \mathbf{j} \cdot d\mathbf{s}. \quad (1.10)$$

Assuming that the fields at infinite go to zero quite quickly, we can write the conservation of the charge:

$$\frac{dq}{dt} = 0 \implies q = \text{constant}. \quad (1.11)$$

In summary, the *global* invariance of the Dirac Lagrangian density under $U(1)$ leads to the existence of a conserved current j^μ as a consequence of Noether's theorem. If the parameter θ defining $U(1)$ changes with x , the transformations of $U(1)$ are called *local* and \mathcal{L}_0 is no longer invariant under $U(1)$: $\mathcal{L}'_0 = \mathcal{L}_0 + j^\mu \partial_\mu \theta$. Since \mathcal{L}_0 is a scalar quantity, a term \mathcal{L}' can be added to ensure that $\mathcal{L} \equiv \mathcal{L}_0 + \mathcal{L}'$ is locally invariant under $U(1)$. For such invariance to be preserved, one can see that

$$\mathcal{L}' = -j^\mu A_\mu \quad (1.12)$$

with $A^\mu(x)$ being a quadri-vector field such that, when a local transformation $e^{-iq\theta(x)}$ of $U(1)$ is performed on $\psi(x)$, it undergoes the transformation:

$$A_\mu' = A_\mu + \partial_\mu \theta. \quad (1.13)$$

With these assumptions, $\mathcal{L} = \mathcal{L}_0 - j^\mu A_\mu$ satisfies the condition $\mathcal{L}' = \mathcal{L}$. It is of the utmost importance to notice that a massive term for the *gauge field* A_μ would break the gauge invariance for which A_μ was introduced in the first place. Hence, the particle associated with this new field is a *mass-less gauge boson*.

One can easily verify that the locally invariant Lagrangian \mathcal{L} can be written as

$$\mathcal{L} = i\bar{\psi}\gamma^\mu \mathcal{D}_\mu \psi - m\bar{\psi}\psi \quad (1.14)$$

where

$$\mathcal{D}_\mu = \partial_\mu + iqA_\mu. \quad (1.15)$$

Equation 1.15 is the so-called *minimal coupling* which is introduced in classical electrodynamics to describe charged particles in an electromagnetic field. We can therefore conclude that the gauge field A_μ is the quantum field associated with the quantum force-carrier of the electromagnetic force, the massless photon.

What has just been displayed is the principle of local gauge invariance, which can be summarized as the following: the request that \mathcal{L} to be locally invariant under a symmetry group makes it mandatory to introduce additional **mass-less boson fields**, the gauge fields, obeying appropriate transformation laws under the symmetry group. Furthermore, the same request determines the *form* of the interaction between the initial free fields and the gauge fields, this coupling always being of current-field type. As we have shown, the symmetry group for QED is $U(1)$, with A_μ being the quantum field describing the photon.

To ensure that A_μ is part of the dynamical system, gauge-invariant terms built upon A_μ itself and its derivatives must be included in the total Lagrangian \mathcal{L} . Adding the kinetic term $-\frac{1}{4}F^{\mu\nu}F_{\mu\nu}$, with $F^{\mu\nu} = \partial^\mu A^\nu - \partial^\nu A^\mu$ being the electromagnetic tensor, meets this request. It is noteworthy that $F_{\mu\nu}$ satisfies the relation which shall be later generalized:

$$[\mathcal{D}_\mu, \mathcal{D}_\nu] = iqF_{\mu\nu}. \quad (1.16)$$

In conclusion, the locally invariant Lagrangian is

$$\mathcal{L} = i\bar{\psi}\gamma^\mu\mathcal{D}_\mu\psi - m\bar{\psi}\psi - \frac{1}{4}F^{\mu\nu}F_{\mu\nu}. \quad (1.17)$$

1.3.2 Local invariance of the Lagrangian under $SU(N)$

Since the local gauge invariance principle turned out to be extremely successful in describing the QED, a similar approach involving non-Abelian Lie groups was pursued by Chen Ning Yang and Robert Mills in the early '50s in order to describe the remaining forces. In particular, the Yang-Mills theory focuses on $SU(N)$, a class of non-Abelian Lie groups of dimension $n = N^2 - 1$ consisting of unitary transformations such that their determinant equals +1. In 1972 Gerard 't Hooft proved Yang-Mills theory to be renormalizable.³

As a non-Abelian group, $SU(N)$ is such that its generators $\mathbf{T} = \{T_i\}_{i=1}^n$ and, therefore, all its elements, do not commute with each other; instead, they satisfy a commutation relation:

$$[T_i, T_j] = if_{ijk}T_k \quad (1.18)$$

where f_{ijk} are the so-called structure constants of the group. For the elements of the group to be unitary, the generators need to be hermitian: $T_i^\dagger = T_i$. An infinitesimal local transformation U of $SU(N)$ is conventionally written as

$$U(\epsilon(x)) = \mathbb{1} - ig\epsilon_i(x)T_i = \mathbb{1} - igvb * \epsilon(x) \cdot \mathbf{T} \quad (1.19)$$

where g is called a *coupling constant*.

Suppose we have a number D of Dirac spinor fields with the same mass m : $\psi = (\psi_1, \dots, \psi_D)^\top$. The corresponding free Lagrangian is:

$$\mathcal{L}_0 = i\bar{\psi}_a\gamma^\mu\partial_\mu\psi_a - m\bar{\psi}_a\psi_a = i\bar{\psi}\gamma^\mu\partial_\mu\psi - m\bar{\psi}\psi \quad (1.20)$$

In order to evaluate the action of $SU(N)$ on the *multiplet* ψ , we choose a D -dimensional representation of $SU(N)$ ⁴, which means that U is a $D \times D$ matrix depending on n parameters. The action of U on \mathcal{L}_0 leads to

$$\mathcal{L}'_0 = \mathcal{L}_0 + \bar{\psi}i\gamma^\mu(U^\dagger\partial_\mu U)\psi. \quad (1.21)$$

One can therefore define a new Lagrangian \mathcal{L}

$$\mathcal{L} = \mathcal{L}_0 - g\bar{\psi}\gamma^\mu T_i\psi W_\mu^{(i)} \equiv \mathcal{L}_0 - j^{(i)\mu}W_\mu^{(i)} = \mathcal{L}_0 - \mathbf{j}^\mu \cdot \mathbf{W}_\mu \quad (1.22)$$

where $\mathbf{W}_\mu = \{W_\mu^{(i)}\}_{i=1}^n$ are n gauge fields which are introduced to ensure the invariance of \mathcal{L} under infinitesimal local transformations of $SU(N)$ like 1.19:

$$\mathcal{L}' = \mathcal{L}_0 + \bar{\psi}i\gamma^\mu(U^\dagger\partial_\mu U)\psi - g\bar{\psi}'\gamma^\mu T_i\psi'W_\mu^{(i)} = \mathcal{L} = \mathcal{L}_0 - g\bar{\psi}\gamma^\mu T_i\psi W_\mu^{(i)}. \quad (1.23)$$

³A renormalizable theory is such that, when equations are written in terms of the *physical* parameters instead of the *bare* parameters (i.e. those included so far in the Lagrangian, such as m and q) the predicted quantities are finite.

⁴If the representation has dimension N , it is called the fundamental representation.

It can be shown that the request 1.23 is fulfilled when:

$$W_\mu'^{(k)} = W_\mu^{(k)} + \partial_\mu \epsilon_k - g f_{ijk} \epsilon_i W_\mu^{(j)} \quad (1.24)$$

which is the non-Abelian counterpart of condition 1.13. The existence of the last term of equation 1.24 is a consequence of the non-Abelian structure of the group.

After introducing the covariant derivative

$$\mathcal{D}_\mu = \partial_\mu + ig \mathbf{T} \cdot \mathbf{W}_\mu \quad (1.25)$$

the locally invariant Lagrangian can be again written as in equation 1.14. Generalizing equation 1.16, one can define n tensors $\mathbf{G}_{\mu\nu} = \{G_{\mu\nu}^{(i)}\}_{i=1}^n$ such that

$$[\mathcal{D}_\mu, \mathcal{D}_\nu] = ig G_{\mu\nu}^{(i)} T_i = ig \mathbf{G}_{\mu\nu} \cdot \mathbf{T}. \quad (1.26)$$

It can be shown that such tensors can be written as

$$G_{\mu\nu}^{(i)} = \partial_\mu W_\nu^{(i)} - \partial_\nu W_\mu^{(i)} - g f_{lki} W_\mu^{(l)} W_\nu^{(k)} \quad (1.27)$$

so that, finally, the locally invariant Lagrangian turns out to be

$$\mathcal{L} = i\bar{\psi}\gamma^\mu \mathcal{D}_\mu \psi - m\bar{\psi}\psi - \frac{1}{4} \mathbf{G}_{\mu\nu} \cdot \mathbf{G}^{\mu\nu}. \quad (1.28)$$

The last term of 1.27 allows for interactions between the gauge bosons associated with the gauge fields $W_\mu^{(i)}$. The latter are referred to as Yang-Mills fields and are always associated with mass-less gauge bosons with $s = 1$; moreover, the term which describes the gauge boson-particle coupling is always of a current-field type, as one can infer by looking at equation 1.22.

As in the Abelian case, the existence of $W_\mu^{(i)}$ ensures the local invariance of \mathcal{L} , whereas the currents $j_\mu^{(i)}$ arise as conserved quantities from the global gauge invariance.

1.4 The Standard Model

Bearing in mind the local gauge invariance principle as a starting point, the Standard Model can be built on the following steps:

- symmetry group G is chosen;
- the fields describing the particles are picked, alongside with their representations under G (i.e. the way the fields transform under G);
- the free Lagrangian of the fields is written;
- the request for the free Lagrangian being locally invariant under G gives rise to as many mass-less gauge fields as the number of generators of G ;
- the Brout–Englert–Higgs mechanism is applied in order to take the masses of some gauge bosons into account in a gauge-invariant way.

The symmetry group of the Standard Model is $G = SU(2)_L \otimes U(1)_Y \otimes SU(3)_c$. In particular:

- $SU(2)_L \otimes U(1)_Y$ is the gauge group of the weak isospin that describes the electroweak interaction and it is obtained from $SU(2)_L$ for the weak interaction and $U(1)_Y$ for the electromagnetic interaction, as results in the Glashow, Weinberg and Salam model.
- $SU(3)_c$ is the non-Abelian group of the color symmetry, that describes the strong interactions between quarks, through an octet of massless bosons, the gluons.

In the following section we will get acquainted with the fundamentals of the electroweak and the strong interactions, alongside with the Brout–Englert–Higgs mechanism and the model behind fermions masses.

1.4.1 The Electroweak Theory

The electroweak interaction is the unified description of electromagnetism and the weak interaction. The Electroweak Theory was first theorized by Glashow, Weinberg and Salam for which they were awarded the 1979 Nobel Prize in Physics. The local gauge group of the weak interaction, under which the Lagrangian must be invariant, is $SU(2)_L$ in the vector space of weak isospin I , where the L subscript refers to the fact that the fermions are left-handed. Left-handed and right-handed are referred to states that are eigenstates of the chirality. In the GWS model the fundamental fermions appear as doublets of the symmetry of weak isospin $SU(2)$, where the generic left-handed fermion f_L is written using the operator of left-handed chiral projection:

$$f_L = \frac{1}{2}(1 - \gamma^5)f. \quad (1.29)$$

The weak interaction does not couple to the quark mass eigenstates, d, s, b , but instead, linear combinations of them, d', s', b' , which are determined by CKM matrix:

$$\begin{pmatrix} d' \\ s' \\ b' \end{pmatrix} = V_{\text{CKM}} \begin{pmatrix} d \\ s \\ b \end{pmatrix}. \quad (1.30)$$

Under a generic transformation of $SU(2)$ a doublet transforms as following:

$$\begin{pmatrix} \nu_e \\ e^- \end{pmatrix}'_L = e^{-i\alpha\gamma/2} \begin{pmatrix} \nu_e \\ e^- \end{pmatrix}_L. \quad (1.31)$$

Only the left-handed components of the fundamental fermions contribute to the weak processes of charged current, due to the V-A (vectorial - axial) structure of the current which can be written in terms of a chiral left-handed projector. However, the right-handed components of the charged fermions react to neutral current processes, therefore they are singlets of $SU(2)$. Neutrinos, in the hypothesis of zero mass, are always left-handed. In Table 1.1 is reported an overview on the quantum numbers of the SM fermions in the

	Generation			Quantum numbers			
	I	II	III	I	I_3	Y	$Q[e]$
Leptons	$\begin{pmatrix} \nu_e \\ e^- \end{pmatrix}_L$	$\begin{pmatrix} \nu_\mu \\ \mu^- \end{pmatrix}_L$	$\begin{pmatrix} \nu_\tau \\ \tau^- \end{pmatrix}_L$	1/2	+1/2	-1	0
	e_R^-	μ_R^-	τ_R^-	0	0	-2	-1
	$\begin{pmatrix} e^+ \\ \bar{\nu}_e \end{pmatrix}_R$	$\begin{pmatrix} \mu^+ \\ \bar{\nu}_\mu \end{pmatrix}_R$	$\begin{pmatrix} \tau^+ \\ \bar{\nu}_\tau \end{pmatrix}_R$	1/2	+1/2	+1	+1
Antileptons	$\bar{\nu}_e$	$\bar{\nu}_\mu$	$\bar{\nu}_\tau$	1/2	-1/2	+1	0
	e_L^+	μ_L^+	τ_L^+	0	0	+2	+1
Quarks	$\begin{pmatrix} u \\ d' \end{pmatrix}_L$	$\begin{pmatrix} c \\ s' \end{pmatrix}_L$	$\begin{pmatrix} t \\ b' \end{pmatrix}_L$	1/2	+1/2	+1/3	+2/3
	u_R	c_R	t_R	0	0	+4/3	+2/3
	d'_R	s'_R	b'_R	0	0	-2/3	-1/3
Antiquarks	$\begin{pmatrix} \bar{d}' \\ \bar{u} \end{pmatrix}_R$	$\begin{pmatrix} \bar{s}' \\ \bar{c} \end{pmatrix}_R$	$\begin{pmatrix} \bar{b}' \\ \bar{t} \end{pmatrix}_R$	1/2	+1/2	-1/3	+1/3
	\bar{u}_L	\bar{c}_L	\bar{t}_L	1/2	-1/2	-1/3	-2/3
	\bar{d}'_L	\bar{s}'_L	\bar{b}'_L	0	0	-4/3	-2/3
			0	0	+2/3	+1/3	

Table 1.1: Overview of the quantum numbers of the Standard Model fermions in the GWS model. The right-handed neutrinos do weakly participate in the SM interactions and they are therefore not considered here.

GWS model and it summarizes the organization of fundamental fermions in doublets and singlets of $SU(2)$.

In order to encompass the electromagnetic and weak interactions, the complete gauge group is:

$$SU(2)_L \otimes U(1)_Y. \quad (1.32)$$

Here, Y is called *weak hyper-charge* and is related to electric charge Q by the *Gell-Mann-Nishima relation* that is $Q = Y/2 + I_3$ where I_3 is the 3rd component of weak isospin.

All members of the same $SU(2)$ multiplet have the same weak hyper-charge value, given by $Y_{multiplet} = 2\bar{Q}$, \bar{Q} is the average charge in the multiplet. Now, preserving local gauge invariance requires four massless fields be introduced: a weak-isospin triplet $\mathbf{W}^\mu \equiv (W_1^\mu, W_2^\mu, W_3^\mu)$ corresponding to $SU(2)$ symmetry and a weak-isospin singlet B^μ for the $U(1)$ symmetry. The mixing of these four fields gives the electroweak bosons γ, W^+, W^-, Z^0 .

The non-Abelian nature of the $SU(2)_L$ group gives rise to self interaction terms and allows W and Z bosons to couple to each other. However the $U(1)_Y$ group is Abelian, such the absence of photon-photon couplings in QED is maintained.

The generic transformation of the $SU(2)_L \otimes U(1)_Y$ group is:

$$\psi_L(x) \rightarrow \psi'_L(x) = e^{i\alpha^\alpha(x) \cdot T_\alpha + i\beta(x)Y} \psi_L(x) \quad (1.33)$$

$$\psi_R(x) \rightarrow \psi'_R(x) = e^{i\beta(x)Y} \psi_R(x) \quad (1.34)$$

where $\alpha^\alpha(x)$ e $\beta(x)$ are locale phases and T_α e Y are the generators of the $SU(2)_L$ and $U(1)_Y$ groups. Be requiring the invariance or the Lagrangian, four new vectorial fields are introduced and the interactions terms are included in the covariant derivative, defined as:

$$\mathcal{D}_\mu = \partial_\mu + i\frac{g}{2}W_\mu^\alpha T_\alpha + i\frac{g'}{2}B_\mu Y \quad (1.35)$$

where g e g' are the coupling constant of the two interaction.

The locally invariant to $SU(2)_L \otimes U(1)_Y$ Lagrangian is then

$$\mathcal{L} = i\bar{\psi}_L \gamma^\mu \mathcal{D}_\mu^L \psi_L + i\bar{\psi}_R \gamma^\mu \mathcal{D}_\mu^R \psi_R - \frac{1}{4}C^{\mu\nu}C_{\mu\nu} - \frac{1}{4}\mathbf{G}^{\mu\nu} \cdot \mathbf{G}_{\mu\nu} \quad (1.36)$$

where $C_{\mu\nu}$ and $\mathbf{G}_{\mu\nu}$ are tensors which satisfy:

$$C_{\mu\nu} = \partial_\mu B_\nu - \partial_\nu B_\mu \quad (1.37)$$

$$G_{\mu\nu}^{(i)} = \partial_\mu W_\nu^{(i)} - \partial_\nu W_\mu^{(i)} - g(\mathbf{W}_\mu \times \mathbf{W}_\nu)^{(i)}. \quad (1.38)$$

1.4.2 Quantum Chromodynamics (QCD)

The QCD is the theory of the strong interaction between quarks and gluons inside the hadrons. It is a non-Abelian local gauge theory based on $SU(3)_c$, where the subscript c stands for color, the quantum number for the strong charge. The color charge is the QCD counterpart of the electromagnetic charge and was proposed in 1964 by Greenberg and Han-Nambu, independently. They theorized three different "values" for the color charge, so that the field representing a quark of flavour f would be

$$\psi^f(x) = \begin{pmatrix} \psi_R^f(x) \\ \psi_G^f(x) \\ \psi_B^f(x) \end{pmatrix} \quad (1.39)$$

with $\psi_i^f(x)$ being Dirac spinors: each quark flavour was theorized to exist into three different color states and $SU(3)$, with its fundamental representation consisting of 3×3 matrices acting on color triplets, was designated as the symmetry group of the strong interaction. $SU(3)_c$ transformations are generated by the eight Gell-Mann matrices λ_i :

$$\psi_i'^f(x) = e^{ig_s \frac{\lambda}{2} \cdot \boldsymbol{\theta}} \psi_i^f(x) \quad (1.40)$$

where $g_s = \sqrt{4\pi\alpha_s}$ is the strong coupling constant. The local gauge invariance principle gives rise to eight massless gauge fields $A_\mu^{(i)}(x)$, which are directly associated with the strong interaction massless carriers, the gluons. The QCD Lagrangian turns out to be

$$\mathcal{L}_{\text{QCD}} = i\bar{\psi}_i^f(x) \gamma^\mu \mathcal{D}_\mu \psi_i^f(x) - \frac{1}{4}\mathbf{G}^{\mu\nu} \cdot \mathbf{G}_{\mu\nu} \quad (1.41)$$

where

$$\mathcal{D}_\mu = \partial_\mu + ig_s \frac{\boldsymbol{\lambda}}{2} \cdot \mathbf{A}_\mu \quad (1.42)$$

$$G_{\mu\nu}^{(i)} = \partial_\mu A_\nu^{(i)} - \partial_\nu A_\mu^{(i)} - g_s f_{ijk} A_\mu^{(j)} A_\nu^{(k)} \quad (1.43)$$

with f_{ijk} being the SU(3) structure constants.

Since an octet arises from the $3 \otimes \bar{3}$ direct product, each gluon is associated with a color-anticolor combination, so that gluons are said to be bi-coloured: differently from the photon, gluons carry the strong charge. A consequence of this is that they are capable of self-interactions, a feature that is taken account of by the non-Abelian nature of the symmetry group, due to which auto-interactions terms arising from 1.43 appear in the QCD Lagrangian.

Studying the quark-antiquark interaction and the three quarks interaction from a perturbative theory approach, one can find that the short-distance potential is in both cases attractive, provided that the system is in a singlet state of SU(3)_c. Mesons (quark-antiquark) and baryons (three quarks) being SU(3)_c singlets is consistent with the experimental fact that no color charge is observed for composite hadrons. Indeed, QCD exhibits a peculiar property, the so-called *color confinement*, which is itself a consequence of another distinctive feature of the quantum chromo-dynamics: the *asymptotic freedom*.

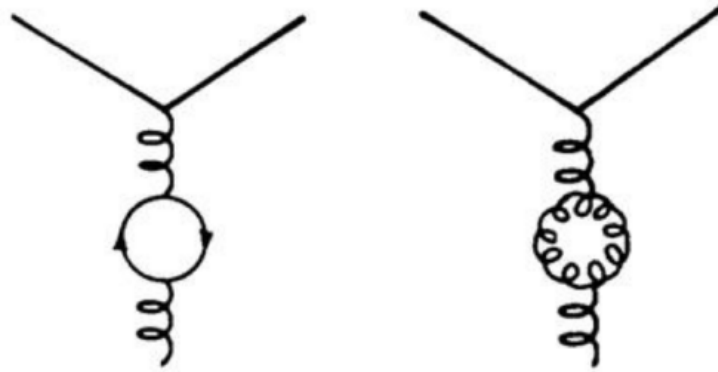


Figure 1.2: QCD Feynman diagrams containing a fermion (left) and a gluon (right) loop. The combination of both amplitudes results in the asymptotic freedom of the QCD.

The *asymptotic freedom* arises from the non-Abelian structure of SU(3)_c. Both QED and QCD predictions can be obtained by means of a perturbation approach, so that a given quantity is actually the sum of all the terms of a perturbation series. High order terms of the series are involved with Feynman diagrams containing loops like those in figure 1.2. The existence of such loops results in the theory providing infinite values of the predictions; fortunately, Yang-Mills theories are proved to be renormalizable, meaning that divergences are taken care of by substituting the bare parameters with physical parameters, including the renormalized coupling constant. In the QCD case, due to the auto-interaction terms of the Lagrangian coming from the non-Abelian structure of SU(3)_c (terms that are therefore absent from the QED picture), higher order Feynman diagrams containing quark-antiquark and gluon loops result in the strong coupling constant g_s depending on the distance in such a way that the closer the quarks are, the weaker the intensity of the interaction is, to the point that they can actually be considered *free*. In contrast, distant quarks undergo such an intense attraction that separating two quarks would require an energy much larger than the energy necessary to create new particles. Therefore, as the quark-quark distance increases, the color field creates additional quarks

and anti-quarks, which bind to the original quarks in such a way that no free quark can be observed in the final state.

1.4.3 The Brout–Englert–Higgs mechanism

In 1962, Goldstone, Salam and Weinberg showed that if there is a continuous symmetry transformation under which the Lagrangian is invariant, then either the vacuum state is also invariant under such transformation, or there must exist as many spinless particles of zero mass (Goldstone bosons) as the generators of the continuous group. This concept is at the heart of the *spontaneous symmetry breaking*: the fact that the system falls into a ground state that does not exhibit the same symmetry of the Lagrangian results in that very symmetry being hidden or *broken*. Two years later, Peter Higgs and, independently, Robert Brout and Francois Englert applied the spontaneous symmetry breaking concept to a locally invariant to U(1) Lagrangian, showing that the massless gauge boson arising from the gauge principle could acquire mass in a gauge invariant way at the expense of the Goldstone scalar boson.

The asymmetric ground state, on whose existence the spontaneous symmetry breaking lies, can be realised by requiring that the expectation value of some field be non-zero.

Let us therefore consider a complex scalar field

$$\phi = \frac{1}{\sqrt{2}}(\phi_1 + i\phi_2). \quad (1.44)$$

The Lagrangian of this field is made invariant under U(1) by means of the covariant derivative 1.15:

$$\mathcal{L} = (\mathcal{D}_\mu \phi)^*(\mathcal{D}^\mu \phi) - \frac{1}{4}F^{\mu\nu}F_{\mu\nu} - V(\phi) \quad (1.45)$$

where $V(\phi) = \mu^2 \phi^\dagger \phi + \lambda(\phi^\dagger \phi)^2$ is the potential term. For the vacuum state of the system to be stable (i.e. for V to exhibit a minimum value), the condition $\lambda > 0$ is essential. If $\mu^2 < 0$, the values of ϕ for which V is minimum define a circle (in the complex plane) of radius v such that

$$v^2 = 2\phi_{\text{vac}}^* \phi_{\text{vac}} = -\frac{\mu^2}{\lambda} \quad (1.46)$$

One can therefore write ϕ_{vac} as

$$\phi_{\text{vac}} = \frac{v}{\sqrt{2}}e^{i\alpha} \quad (1.47)$$

with α being an arbitrary phase factor. Whereas \mathcal{L} is invariant to U(1) by definition, ϕ_{vac} is not: the action of a U(1) transformation on 1.47 leads to a different point of the circle. Let us suppose that the vacuum state which the system falls spontaneously into is defined by $\alpha = 0$. One can think of the field ϕ as an expansion around this vacuum state, namely

$$\phi = \frac{v + H(x)}{\sqrt{2}}e^{i\frac{\theta(x)}{v}} \quad (1.48)$$

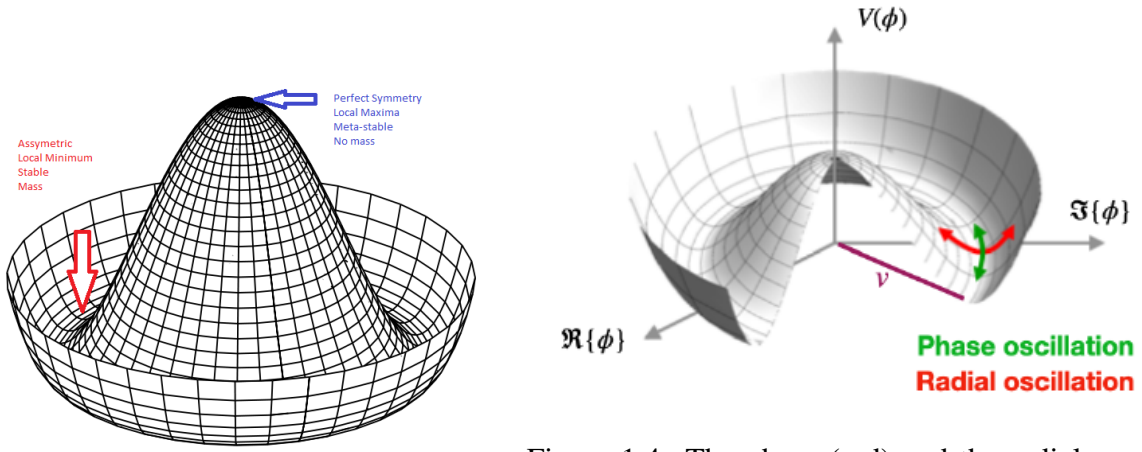


Figure 1.3: Higgs potential for a complex scalar field.

Figure 1.4: The phase (red) and the radial oscillations (green) around the vacuum state are displayed.

where $H(x)$ and $\theta(x)$ take account of the radial and phase oscillations around $\phi_{\text{vac}} = v/\sqrt{2}$, respectively (Figure 1.4).

Substituting 1.48 in 1.45, one can find that, while the Goldstone boson $\theta(x)$ remain massless, massive terms for both the scalar boson field $H(x)$ and the gauge field A_μ arise, so that the system seems to gain one extra degree of freedom. Actually, the local gauge invariance of \mathcal{L} allows for a U(1) transformation such that

$$\phi' = e^{-iq\beta(x)}\phi = \frac{(v + H(x))}{\sqrt{2}}. \quad (1.49)$$

In doing so, one degree of freedom belonging to the Goldstone boson $\theta(x)$ is *gauged away*, letting the gauge boson A_μ acquire mass while preserving gauge invariance.

After Glashow proposed $SU(2)_L \otimes U(1)_Y$ as the electroweak symmetry group, Weinberg and Salam probed the Brout-Englert-Higgs mechanism in the case of a weak isospin doublet of complex scalar fields with $Y = 1$ (namely, the Higgs field)

$$\phi = \begin{pmatrix} \phi^+ \\ \phi^0 \end{pmatrix} = \frac{1}{\sqrt{2}} \begin{pmatrix} \phi_1 + i\phi_2 \\ \phi_3 + i\phi_4 \end{pmatrix} \quad (1.50)$$

by adding the term

$$\mathcal{L}_H = (\mathcal{D}_\mu^L \phi)^\dagger (\mathcal{D}^{L\mu} \phi) - V(\phi) \quad (1.51)$$

to the Lagrangian 1.36. Here, \mathcal{D}_μ^L is the covariant derivative

$$\mathcal{D}_\mu^L = \partial_\mu + ig \frac{\boldsymbol{\sigma}}{2} \cdot \mathbf{W}_\mu + ig' Y B_\mu \quad (1.52)$$

while the potential $V(\phi)$ is

$$V(\phi) = \mu^2 \phi^\dagger \phi + \frac{\lambda}{4} (\phi^\dagger \phi)^2. \quad (1.53)$$

Again, picking one quadruplet ϕ_1, \dots, ϕ_4 among the set of all the (physically) equivalent vacuum states, writing the Higgs field as an expansion around the chosen ϕ_{vac} after a gauge transformation such that the massless Goldstone bosons are gauged away, and substituting such a ϕ in the Lagrangian, one finds (as the gauge fields and the Higgs field are concerned):

$$\begin{aligned} \mathcal{L}_{G\phi} = & \frac{1}{2} \partial_\mu H \partial^\mu H - \lambda v^2 H^2 \\ & - \frac{1}{4} (\partial_\mu W_\nu^{(1)} - \partial_\nu W_\mu^{(1)}) (\partial^\mu W^{(1)\nu} - \partial^\nu W^{(1)\mu}) + \frac{1}{8} g^2 v^2 W_\mu^{(1)} W^{(1)\mu} \\ & - \frac{1}{4} (\partial_\mu W_\nu^{(2)} - \partial_\nu W_\mu^{(2)}) (\partial^\mu W^{(2)\nu} - \partial^\nu W^{(2)\mu}) + \frac{1}{8} g^2 v^2 W_\mu^{(2)} W^{(2)\mu} \\ & - \frac{1}{4} (\partial_\mu W_\nu^{(3)} - \partial_\nu W_\mu^{(3)}) (\partial^\mu W^{(3)\nu} - \partial^\nu W^{(3)\mu}) - \frac{1}{4} C^{\mu\nu} C_{\mu\nu} \\ & + \frac{1}{8} v^2 (g W_\mu^{(3)} - g' B_\mu) (g W^{(3)\mu} - g' B^\mu). \end{aligned}$$

The first line refers to the massive Higgs field ($m_H = \sqrt{2\lambda}v$); the second and third lines contain the kinetic and the massive terms of $W_\mu^{(1)}$ and $W_\mu^{(2)}$ ($M_W = gv/2$); the fourth line takes account of $W_\mu^{(3)}$ and B_μ kinetic terms, while the last line is a massive term of a combination of $W_\mu^{(3)}$ and B_μ . Given the Weinberg angle θ_W such that

$$\cos \theta_W = \frac{g}{\sqrt{g^2 + g'^2}}, \quad \sin \theta_W = \frac{g'}{\sqrt{g^2 + g'^2}} \quad (1.54)$$

one can define the gauge fields Z_μ and A_μ

$$Z_\mu = W_\mu^{(3)} \cos \theta_W - B_\mu \sin \theta_W \quad (1.55)$$

$$A_\mu = W_\mu^{(3)} \sin \theta_W + B_\mu \cos \theta_W \quad (1.56)$$

Rearranging the Lagrangian in terms of these fields, A_μ is found to be massless, while Z_μ has mass $m_Z = m_W / \cos \theta_W$; in addition, $W_\mu^{(1)}$ and $W_\mu^{(2)}$ turn out to be mixed into two fields $W_\mu^{(+)}$ and $W_\mu^{(-)}$ (with the same mass as before) such that

$$W_\mu^{(\pm)} = \frac{W_\mu^{(1)} \mp i W_\mu^{(2)}}{\sqrt{2}}. \quad (1.57)$$

Last but not least, in order to obtain the proper electromagnetic covariant derivative, the following condition must be true:

$$q = g \sin \theta_W. \quad (1.58)$$

Equation 1.58 encodes the essence of the electroweak unification.

In summary, the gauge fields responsible for the electroweak interaction are A_μ , $W_\mu^{(+)}$, $W_\mu^{(-)}$ and Z_μ , whose quanta are the massless photon γ and the massive bosons W^+ , W^- and Z^0 , respectively. The existence of the weak neutral current (mediated by Z^0) was proven in 1973 by the Gargamelle collaboration; ten years later, the UA1 and the UA2 collaborations provided the observation of the W and Z bosons at the Super Proton Synchrotron.

1.4.4 Fermions masses

Up until now, we have taken fermion masses into account by adding a Dirac mass term $m\psi\bar{\psi}$ to the Lagrangian, like in equation 1.14. This term can actually be written as

$$m\psi\bar{\psi} = m(\psi_L\bar{\psi}_R + \psi_R\bar{\psi}_L). \quad (1.59)$$

Even though equation 1.59 is invariant under U(1), this is not the case for the Standard Model symmetry group $SU(2)_L \otimes U(1)_Y \otimes SU(3)_c$: more precisely, ψ_L and ψ_R undergo different transformations under $SU(2)_L$, so that the Dirac term 1.59 results in not being invariant. In order to take account of fermion masses in a gauge invariant way, an interaction term between the fermion field and the Higgs field can be added to the Lagrangian, so that mass terms arise by means of the spontaneous symmetry breaking mechanism. This additional term is referred to as Yukawa interaction term and has the form

$$\mathcal{L}_{\text{Yukawa}} = -G_l^{ij} \bar{L}_L^i \phi l_R^j - G_d^{ij} \bar{Q}_L^i \phi d_R^j - G_u^{ij} \bar{Q}_L^i \phi_C u_R^j + \text{h.c.} \quad (1.60)$$

where L_L^i and Q_L^i ($i = 1, 2, 3$) are leptons and quarks $SU(2)_L$ doublets, l_R^j , u_R^j , d_R^j ($j = 1, 2, 3$) are leptons and quarks $SU(2)_L$ singlets, ϕ is the Higgs field 1.50 and ϕ_C is the conjugate $SU(2)_L$ doublet of ϕ , defined as

$$\phi_C = i\sigma_2 \phi^* = \begin{pmatrix} \phi^{0*} \\ -\phi^- \end{pmatrix} = \frac{1}{\sqrt{2}} \begin{pmatrix} \phi_3 - i\phi_4 \\ -(\phi_1 - i\phi_2) \end{pmatrix}. \quad (1.61)$$

As usual, the hermitian conjugate takes account of the anti-fermion terms of the Lagrangian. The 3×3 matrices G_l^{ij} , G_d^{ij} , G_u^{ij} are known as Yukawa matrices and define the coupling constant and the mixing of the quarks generation. Operating the symmetry breaking mechanism, i.e. choosing a specific vacuum state, writing the Higgs field as expansion terms around ϕ_{vac} and applying a $SU(2)_L$ transformation to ϕ such that the Goldstone bosons are gauged away, the fermion masses values are obtained. For instance, the mass term for the electron field is:

$$\mathcal{L}_e = -\frac{G_e}{\sqrt{2}} v (\bar{e}_L e_R + \bar{e}_R e_L) - \frac{G_e}{\sqrt{2}} (\bar{e}_L e_R + \bar{e}_R e_L) H = -m_e \bar{e}e - \frac{m_e}{v} \bar{e}e H \quad (1.62)$$

where $m_e = \frac{G_e v}{\sqrt{2}}$ is the electron mass.

The coupling constant G_e is not fixed and the actual electron mass is not predicted. The Lagrangian has also an interaction term that couples the Higgs field to the electron field and this term is proportional to the electron mass.

The masses of the other fermions are generated in the same way except for the neutrinos that are considered massless according to the Standard Model. In particular the coupling among Higgs and quarks mass eigenstates is not diagonal. To obtain a diagonal matrix four unitary transformations are needed, in order to transform the interaction eigenstates in the mass eigenstates. These transformations effectively modify the current: in the case of charge current, these transformations put in evidence a violation of the charge conjugation symmetry and of the parity symmetry (CP).

1.5 Unsolved issues in the Standard Model

The success of the Standard Model in describing the wide range of precise experimental measurements is a remarkable achievement. The recent precision tests of the SM and the discovery of the Higgs boson have firmly established the validity of the theory at energies up to the electroweak scale. The features of the weak neutral current is successfully predicted by the SM likewise the existence of the W and Z bosons as well as their masses. Similarly, further prediction consist in the charm quark c , as required by the GIM mechanism, and in the existence of the top quark: its measurable contributions to radiative corrections, driven by its large mass, are a further validation of the mathematical-consistence of renormalizable field theory. Despite this success, there are many unanswered questions. One of the main open questions regards the number of free parameters in the model: if the neutrino is a normal Dirac fermion the Standard Model has 25 (or 26) free parameters that have to be input by hand. They are the masses of the twelve fermions (or perhaps more correctly the twelve Yukawa couplings to the Higgs field), the three coupling constants describing the strengths of the gauge interactions (g' , g_W and g_S), the two parameters describing the Higgs boson (ν and m_H) and the eight mixing angles of the PMNS and CKM matrices. In principle, there is one further parameter in the Standard Model: the Lagrangian of QCD can contain a phase that would lead to CP violation in the strong interaction. Experimentally, this strong CP phase is known to be extremelly small and is usually taken to be zero. If CP is counted, then the Standard Model has 26 parameters that has to be fixed from the outside. This large number of free parameters is symptomatic of the SM being just a model where the parameters are chosen to match the observations, rather than coming from a higher theoretical principle. There are also other problems, relating some aspects of the Physics that are not explain by the Standard Model; some of them summarized here:

- Gravity: the SM does not include in any way General Relativity, and there is no obvious explanation of the large difference between the Planck and the SM interaction scales.
- Matter-antimatter asymmetry: the sole SM CP -violation in the quark sector is not enough to justify the actual matter-antimatter asymmetry measured in the universe.
- Hierarchy in fermion masses: there is no explanation of varies in fermion masses that changed, for example, over 5 order of magnitudes between the top quark and the electron. Even more mysterious are the neutrinos, which are many orders of magnitude lighter still.
- Higgs mass fine tuning: fine tuning is required to deal with divergences in the Higgs sector.
- Flavour changing neutral current: the SM does not predict the observed suppression of flavour changing due to neutral currents.
- Dark matter: from astrophysical observations it is found that the orbits followed by galaxies are different from which expected considering the gravitational effects of the usual matter and it is does not interact via electromagnetic force.

- Dark energy: from cosmological observations, in particular from the red shift measurement, it is discovered that the Universe is accelerated; this phenomenon has no explanation in the SM framework.

Because of these reasons and indeed others not discussed here, it is a widely held opinion within the scientific community that the SM is an effective theory which we currently probe at low energy. The general theory will begin to become accessible when the predictions of the SM start to become incorrect. More precise determination of the free parameters of the SM will allow the scale at which this happens to be better understood.

Chapter 2

CMS experiment at LHC, CERN

2.1 Introduction

The main achievement of the SM is the description of the interactions between fundamental particles and likewise the prediction of the particles to be searched, as we have seen in Chapter 1. The predictions of the SM, including all its particles as well as their properties, have been tested several times, during the years, by experimental particle physics. Among the most important tools for such tests are the particle accelerators, machines able to accelerate elementary particles, like electrons, or composite particles, like protons, to collimate them into beams, and to collide them against fixed target or other beams. A fundamental motivation of the Large Hadron Collider (LHC) is, in fact, to provide an explanation of the nature of electroweak symmetry breaking for which the Higgs mechanism is responsible. The experimental study of the Higgs mechanism can also shed light on the mathematical consistency of the SM at energy scales above about 1 TeV. The Large Hadron Collider (LHC) is the most powerful particle accelerator ever built: it is able to collide two proton beams at the design energy in the centre of mass equal to $\sqrt{s} = 13 \text{ TeV}$.¹ Four great experiments have been designed at LHC: Compact Muon Solenoid (CMS), A Toroidal LHC ApparatuS (ATLAS), A Large Ion Collider Experiment (ALICE), LHC-beauty (LHC-b) as we can see in Figure 2.1. In this chapter an overview of the LHC machine and operation and a detailed description of the CMS experiment are given.

2.2 The Large Hadron Collider

The Large Hadron Collider at CERN (Conseil européen pour la recherche nucléaire) near Geneva, consists of two 27 km circumference rings of superconducting magnets and accelerating structures. The tunnel is located between 45 m and 170 m below the ground level and it spans the Swiss-French border. The machine is designed to provide proton-proton collisions with a center-of-mass energy of 14 TeV, with an instantaneous luminosity² of $10^{34} \text{ cm}^{-2} \text{ s}^{-1}$; these features makes LHC the highest energy collider ever built.

¹This is the energy in the centre-of-mass reached during Run-II while LHC is designed to provide proton-proton collisions with a center-of-mass energy of 14 TeV

²see Section 2.2.1.

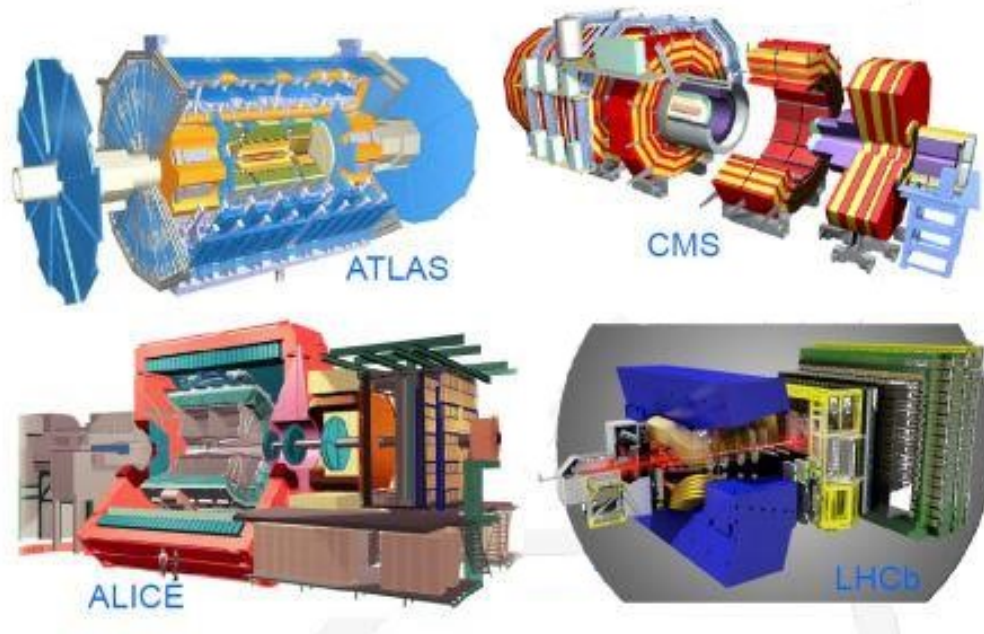


Figure 2.1: The four great experiments at LHC.

It can also collide heavy (Pb) ions with an energy of 2.8 TeV per nucleon and a peak luminosity of $10^{27} \text{ cm}^{-2} \text{ s}^{-1}$. During his history, the CERN has built several particle accelerator in order to constantly increase the collision energy. LHC is the last stage of a complex of different accelerators: each machine brings the energy of the particle beams to a certain threshold before injecting them into the next stage. Over this history, usually when a new machine was realized, the one previously built acted as injector. The protons source is a simple tank of hydrogen gas in which electrons are stripped from hydrogen atoms by electric fields to yield protons. Consequently, protons are injected into a complex series of different accelerators:

- Linac 2, a linear accelerator, which accelerates them up to 50 MeV of energy;
- Proton Synchrotron Booster (PBS), which brings them to 1.4 GeV ;
- Proton Synchrotron (PS), which accelerates them to 25 GeV ;
- Super Proton Synchrotron (SPS), which raises the energy to 450 GeV before finally injecting the beam into LHC.

A schematic view of LHC can be seen in figure 2.2.

LHC uses radio frequency cavities to accelerate beams by 485 KeV at each turn. The beams have 2808 circulating proton bunches each and are arranged in 3 or 4 trains of 72 bunches. The trains are spaced by 25 ns each, which means that there are 8 empty bunches between two trains. At every bunch crossing occur the collisions between the beams so the resulting maximum collisions rate is 40 MHz . The accelerator complex is

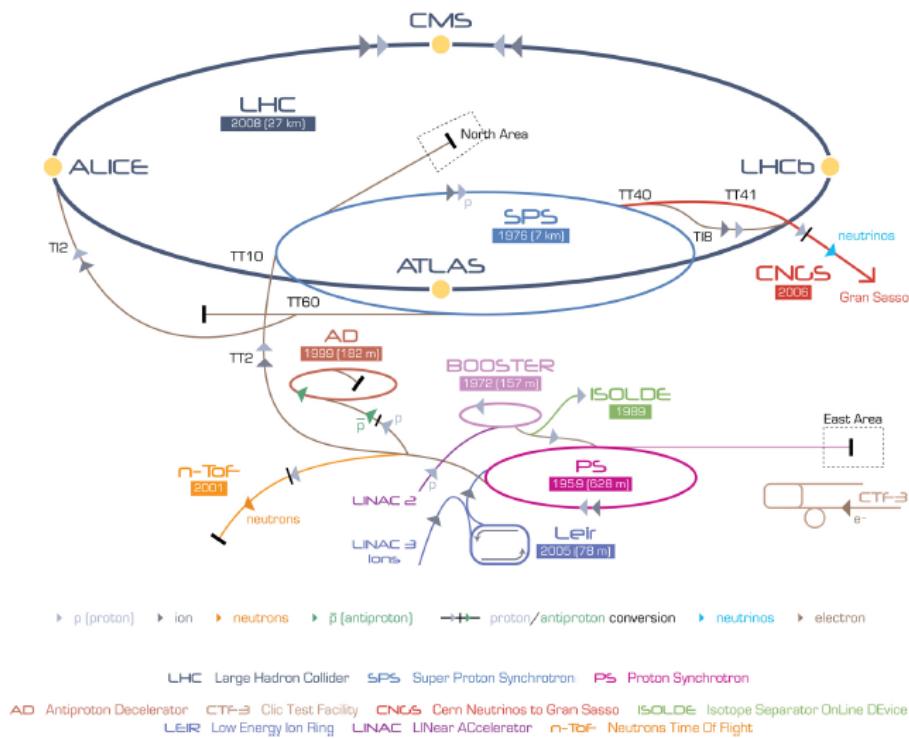


Figure 2.2: The CERN accelerating complex.

also composed of superconducting magnets, in particular 1232 dipoles which allows to keep the beams in the circular ring and 392 quadrupoles which are employed to focus the beams and sextupole, octupole and decapole for spool piece corrections. The dipoles are powered by an electric current of 11.700 A in order to generate a magnetic field with a nominal strength of 8.33 T. The entire magnetic system is based on the niobium-titanium (NbTi) Rutherford cables technology and works at a temperature of 2 K, obtained using the superfluid helium. In order to allow two protons beams circulating in opposite directions, every structure of LHC is built with a sophisticated twin-bore design. The particular design also allows to use only one cryogenic structure for the proton rings in the same cryostat, but this ultimately requires the presence of oppositely oriented magnetic fields to allow the coexistence of two proton beams along the same circumference. The two beams are kept on parallel orbits and are brought together in a single beam pipe only near the interaction point (IP). The vacuum is also required in the LHC for three main reason: the insulation of the cryomagnets, the helium distribution and a the beam vacuum. The requirements for the beam vacuum are very stringent to guarantee the beam lifetime and to minimise the background at the experiments. The typical vacuum at cryogenic temperatures in the IP requires a pressure in the range 10^{10} to 10^{11} mbar. The protons beams rotate for many hours in the LHC beam pipes before they are brought in collision in the IPs; in correspondence of that points particle detectors are located, in order to analyse the products of the collision. The accelerator complex includes also other facilities like Antiproton Decelerator and the Online Isotope Mass Separator (ISOLDE) and feeds different physics project like the CERN Neutrinos to Gran Sasso (CNGS) and the Compact Linear Collider test area.

2.2.1 Luminosity

An important parameter for a particle accelerator is the *instantaneous luminosity* $\mathcal{L}(t)$ that links the cross section³ of a given process with the number of expected events N per unit of time in the collisions:

$$\frac{dN_{event}}{dt} = \mathcal{L}\sigma_{event} \quad (2.1)$$

where σ_{event} is the cross section for the process under study. By integrating the 2.1 one can obtain the number of events for a process with given cross section in a known amount of time:

$$N_{process} = L \cdot \sigma_{event} \quad (2.2)$$

where L is called *integrated luminosity* and it is defined as:

$$L = \int \mathcal{L} dt. \quad (2.3)$$

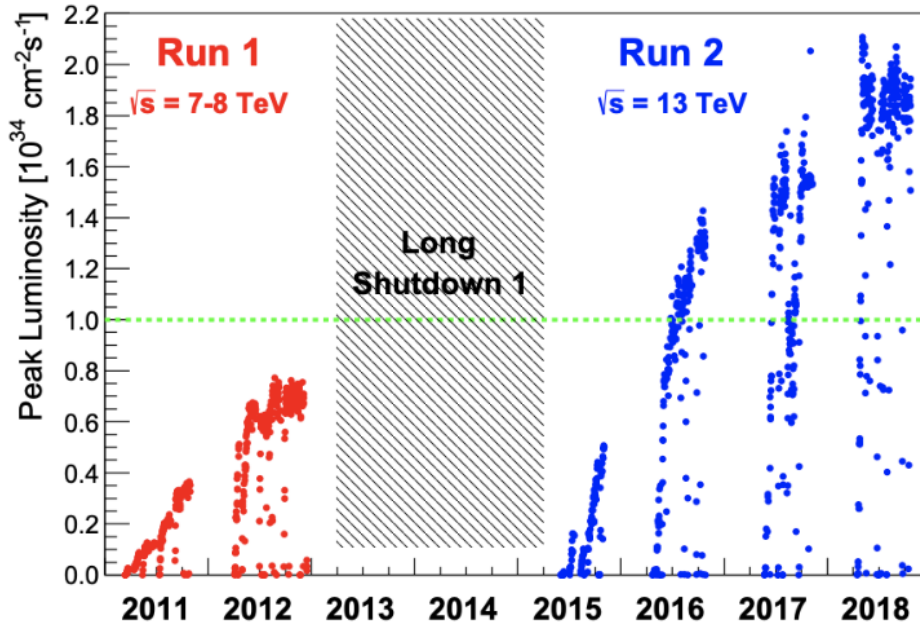


Figure 2.3: LHC peak luminosity for the 2011-2018 period.

The machine luminosity depends only on the beam parameters and can be written, for circular proton-proton accelerators and assuming a Gaussian beam distribution, as:

$$L = \frac{N_b^2 \gamma_r f_{rev} n_b}{4\pi \epsilon_n \beta^*} F, \quad (2.4)$$

where N_b is the number of particles per bunch, n_b the number of bunches per beam, f_{rev} the revolution frequency, γ_r the relativistic gamma factor, ϵ_n the normalised transverse

Parameter	Value
N_b	1.15×10^{11}
n_b	2556
f_{rev}	40 MHz
γ_r	4260
β^*	0.3 - 0.25 m
ϵ_n	2.0 μm
θ_c	320 - 260 μrad
σ_z	9.4 cm
σ^*	19 μm

Table 2.1: The LHC machine parameters.

beam emittance, β^* the beta function at the collision point, and F the geometric luminosity reduction factor due to the crossing angle at the interaction point.

The geometric luminosity reduction can be written as follow:

$$F = \left(1 + \left(\frac{\theta_c \sigma_z}{2\sigma^*} \right)^2 \right)^{1/2}, \quad (2.5)$$

where θ_c is the full crossing angle of the beams at the interaction point, σ_z is the bunch length and σ^* is the transverse RMS beam size at the interaction point. For the 2018 operating period, the values of the above parameters are summarized in Table 2.1.

The trend of the LHC peak luminosity between 2011 and 2018 is shown in figure 2.3, where notably the peak luminosity achieved has already reached its design value of $4.0 \times 10^{34} \text{cm}^{-2}\text{s}^{-1}$.

2.2.2 LHC experiments and data taking activity

The Large Hadron Collider has four main experiments as we can see in 2.1:

- ALICE: *A Large Ion Collider Experiment* is a dedicated ion experiment; it works with $\sqrt{s} = 2.67$ TeV lead-lead ion collisions aiming at a peak luminosity of $L = 10^{27} \text{cm}^{-2}\text{s}^{-1}$.
- ATLAS: *A Toroidal LHC ApparatuS* is a general-purpose detector whose targets are precision measurements of SM, the search and the study of Higgs boson and mechanisms due to new physics. It is 46 m long and has a 25 m diameter and it is the biggest experiment at LHC.
- CMS: *Compact Muon Solenoid* is described in following section.
- LHCb: *LHC-beauty* is an experiment designed and optimised for the study of the b quark properties and its production mechanism.

³The collision or interaction of two particles is generally described in terms of *cross section* that gives a measure of the probability for a reaction to occur and may be calculated if the form of the basic interaction between two particles is known.

The LHC activity started in 2009 with a run at $\sqrt{s} = 0.9$ and $\sqrt{s} = 2.56$ TeV. In 2010, p-p collisions with a centre-of-mass energy at $\sqrt{s} = 7$ TeV were produced until 2011; in 2012/2013 the p-p collisions were at $\sqrt{s} = 8$ TeV. The 2010-2013 activity is called LHC Run I. In 2013 LHC stopped for the upgrade of the detectors in view of the $\sqrt{s} = 13$ TeV p-p collisions. In 2015 the LHC activity started again with $\sqrt{s} = 13$ TeV p-p collisions until 2018. This last period is called LHC Run II. The total integrated luminosity of CMS data collected during the years are reported in Table 2.2.

Period	Year	\sqrt{s} [TeV]	LHC delivered [fb ⁻¹]	CMS Recorded [fb ⁻¹]	CMS Validated [fb ⁻¹]
Run I	2010	7	40.22×10^{-2}	40.76×10^{-2}	34.68×10^{-2}
	2011	7	6.13	5.55	5.09
	2012	8	23.30	21.79	19.79
Run II	2015	13	4.22	3.81	2.39
	2016	13	40.82	37.76	35.92
	2017	13	49.79	44.98	41.53
	2018	13	67.86	63.67	59.7

Table 2.2: The cumulative luminosity delivered by LHC, recorded by CMS and certified as Good for physics analysis, during each period of activity.

2.3 The CMS experiment

The Compact Muon Solenoid experiment is one of the four great experiments at the LHC. Its main goals are to provide measurements at the TeV energy scale from the SM, such as high precision tests of QCD, flavour physics electroweak interactions and the Higgs boson properties, and to explore new physics beyond SM through searches in channels like Supersymmetry (SUSY), a theory based on the same SM fields but that introduce new interactions, or searches for new vector bosons and quarks, the so-called exotic searches. For these reasons, the CMS experiment is defined general-purpose-detector, meaning its research program includes most of the physics at the LHC, from the SM measurements, with particular focus on the Higgs boson, to new physics searches.

CMS is equipped with a huge superconducting magnet, as shown in Figure 2.4 which produces a solenoidal magnetic field of 3.8 T, from which the experiment takes its name. CMS has a component where the sensitive surfaces of the detectors run coaxial to the beam, named Barrel, and two components that close the barrel, named Endcaps, where the sensitive surfaces are orthogonal to the beam axis instead. CMS has a cylindrical symmetry and it is 21.6 m long with a diameter of 14.6 m and a total weight of about 14000 tons.

The detector, therefore, is composed by different sub-detectors (Figure 2.5), with high momentum resolution in a large range of energy. Each sub-detector is designed to work at high luminosities, therefore in a high radiation environment, maintaining good performances over the course of several years. It is also required an high spatial resolution,

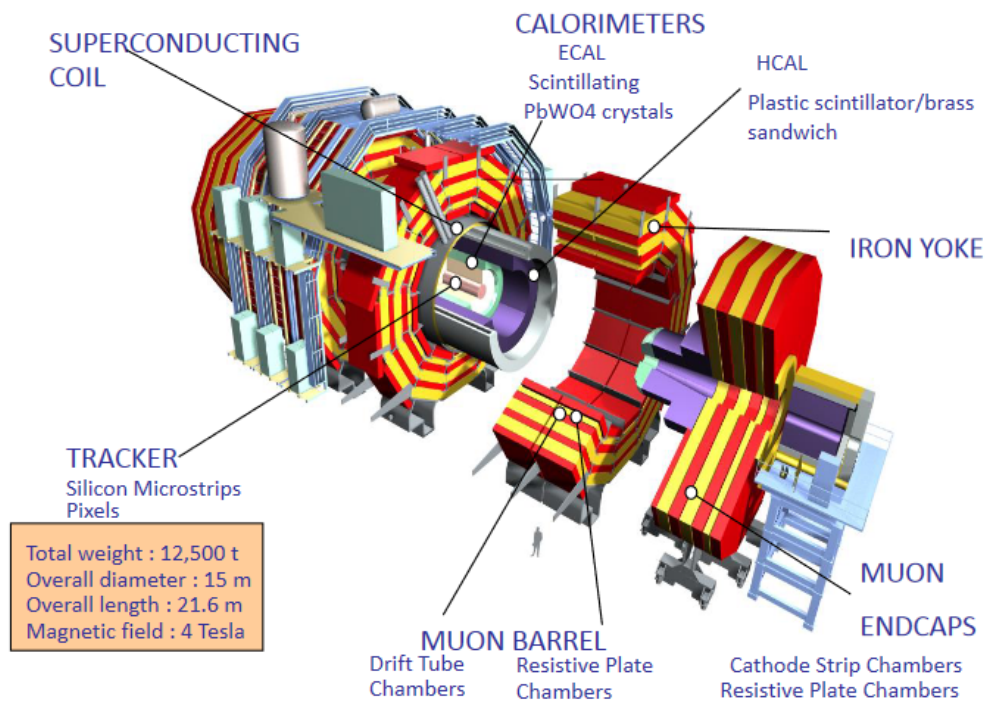


Figure 2.4: The CMS experiment.

or high granularity, for the sub-detectors, to reduce the pile-up. The pile-up is the overlapping between two particles of the same event or from different events in the same bunch-crossing, reconstructed as one particle. The same problem occurs if the time resolution is not good and the detector's response is slower than the time interval between two bunch-crossings.

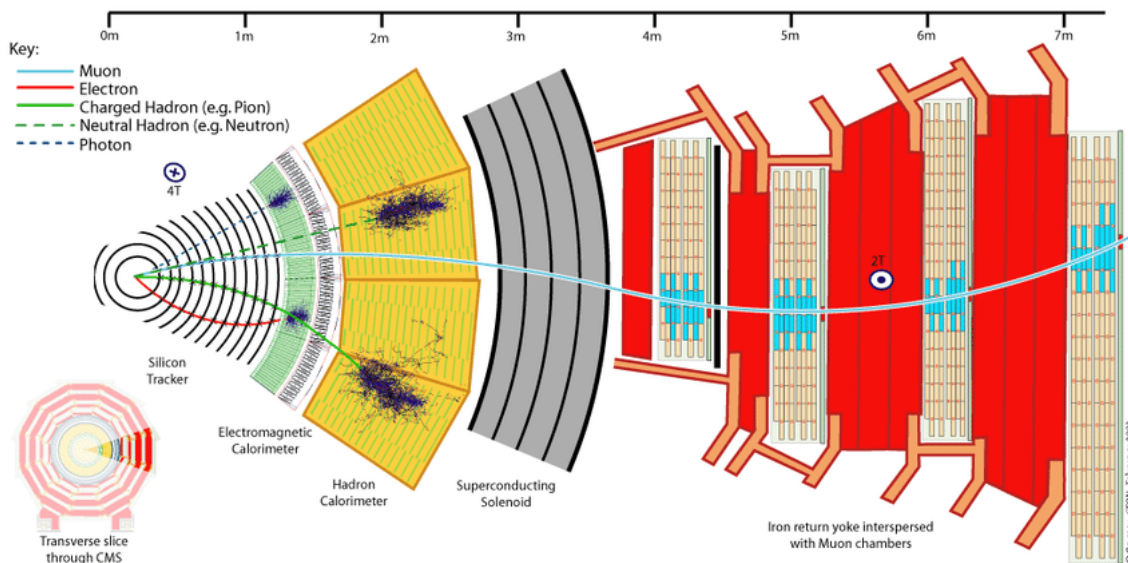


Figure 2.5: The CMS subdetectors system.

In order to cope with these challenges, CMS was designed to have:

- **Geometrical coverage:** full azimuthal coverage is required to make the detector hermetic. In this way it is possible the kinematic closure of the events in the plane transverse to the beams axis and therefore the measurement of the missing transverse energy (MET) is possible.
- **Trigger efficiency:** the huge number of events that happen in a bunch crossing has to face with limitations in the bandwidth at which data can be transferred to the storage facilities; this implies a reduction which has to be performed with an electronic triggering system.
- **High granularity and good time resolution:** the huge amount of particles to be detected requires detectors with high granularity in order to avoid, or at least to limit, the overlap between different particles of the same event or coming from interactions in the same bunch crossing. The effect of this pile-up can be reduced also using fast electronic elements.
- **Radiation endurance:** Radiation endurance: the high-rate radiation implies consequence on the detectors which have to sustain a severe amount of radiation, and have to maintain good performances over the course of several years of data taking.

2.3.1 The coordinate frame at CMS

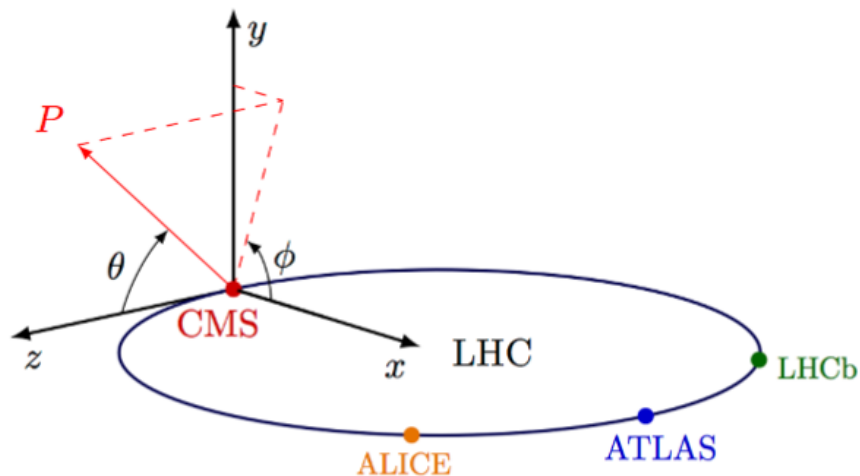


Figure 2.6: The coordinate system in CMS experiment.

The CMS coordinate system used to describe the detector is a right-handed Cartesian frame, centred in the interaction point and with the z axis along the beam line. Particularly, to describe the collision events:

- x - axis is chosen to be horizontal and pointing towards the centre of the LHC ring;
- y - axis is vertical and pointing upwards;

- z - axis has longitudinal direction, i.e. along the beam line.

The $x - y$ plane is called *transverse plane*. Given the cylindrical symmetry of the CMS design, usually a (ϕ, θ) cylindrical coordinate system is used in the reconstruction of the tracks of particle, Figure 2.6. The azimuthal angle ϕ lays in the $x - y$ plane, it is measured from the x axis in mathematical positive direction (i.e the y axis is at $\phi = 90^\circ$) and the radial coordinate in this plane is referred to as r . The polar angle θ is measured from the z axis towards the $x - y$ plane and can be translated into the *pseudorapidity* η by:

$$\eta = -\ln\left(\tan\frac{\theta}{2}\right) \quad (2.6)$$

A longitudinal view of the CMS detector displaying the segmentation in η of the sub-detectors is shown in Figure 2.7.

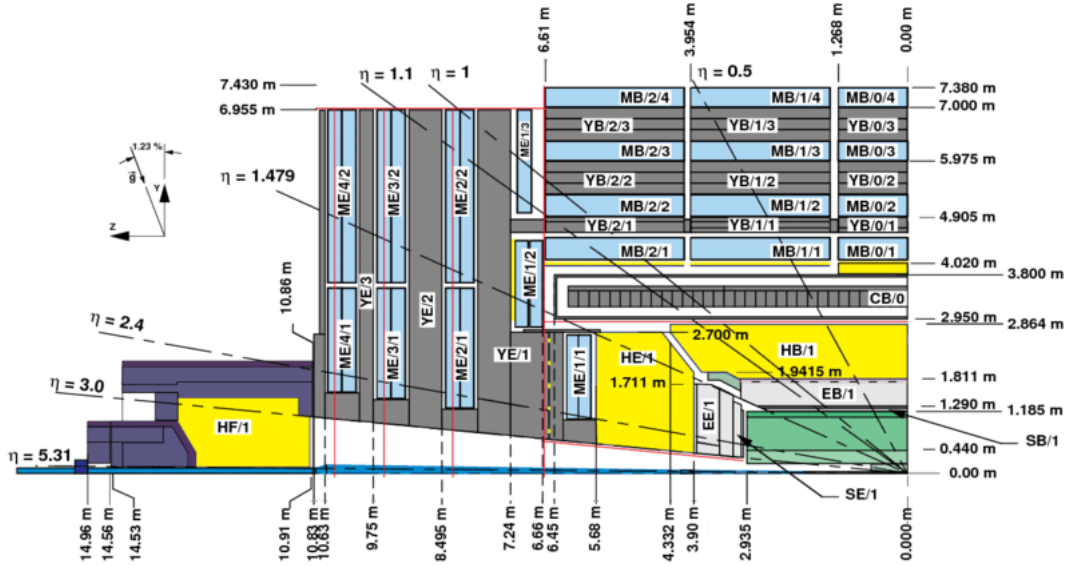


Figure 2.7: Longitudinal view of the CMS detectors.

Referring to this system, the distance between two particle direction can be written as Lorentz invariant variable, in the following way:

$$\Delta R = \sqrt{(\Delta\phi)^2 + (\Delta\eta)^2} \quad (2.7)$$

Referring to the Cartesian system, the momentum of a particle can be divided in two components: the longitudinal momentum p_z and the transverse momentum p_T , defined as:

$$\vec{p}_T = \sqrt{\vec{p}_x^2 + \vec{p}_y^2} \quad (2.8)$$

Usually, another important variable, referred to the Cartesian system, is defined as:

$$E_T = E \sin \theta \quad (2.9)$$

and is called *transverse energy*.

The magnet bends charged tracks on the ϕ plane, so that the curvature of the tracks allows for measurements of the particles p_T . For a particle of energy E (measured in GeV), the variable *rapidity* (y) is also introduced as:

$$y = \frac{1}{2} \ln \left(\frac{E + p_z c}{E - p_z c} \right) \quad (2.10)$$

For ultra relativistic particles rapidity can be approximated by pseudorapidity. Both rapidity and p_T are used because the centre-of-mass of parton-parton collisions can be boosted along the z direction; both these quantities have invariance properties under this kind of boost.

2.3.2 The CMS sub-detector layout

The CMS sub-detector system consist of:

- **The inner tracking system:** designed to provide a precise and efficient measurements of the trajectories of charged particles emerging from the LHC collisions.
- **The electromagnetic calorimeter (ECAL):** essential for accurate electron and photon energy measurements.
- **The hadron calorimeter (HCAL):** it manages to distinguish between charged and neutral particles thanks to the tracker. It is crucial for energy measurements of jets and missing energy, provides energy measurements for charged and neutral hadrons.
- **The superconducting solenoid:** the coil generating an internal constant magnetic field of 3.8T in the direction of the beam axis.
- **The iron yoke:** sustain the structure and it is studied to allow magnetic field lines of the solenoid.
- **The Muon System:** designed to have the capability of reconstructing the momentum and charge of muons over the entire kinematic range of the LHC.

The tracking system

The tracker is designed to measure the position of charged particles arising from the collision [1]. It is the closest sub-detector to the IP, so to allow to best-possible accuracy in the reconstruction of the secondary vertices of interaction. The tracker has a diameter of 2.5 m and a length of 5.8 m, with an acceptance in η of $|\eta| < 2.5$. It has an active area of 200 m² and is composed of the inner tracker, made of silicon pixel detectors (that ensuring an accurate measurement of the vertex positions), and the outer tracker, made of silicon strip

detectors (SST, used for accurate track reconstruction). The inner detector has an accuracy of $10 \mu\text{m}$ and of $20 \mu\text{m}$ respectively for the radial and transverse positions and was designed with 60 millions pixels distributed in three barrel layers and the two endcaps. After an upgrade, performed between the years 2016 and 2017, it now features 124 millions of pixel detectors distributed in four barrel layers and three endcaps. Additionally, the outer tracker has an accuracy between $35 \mu\text{m}$ and $52 \mu\text{m}$ for the radial position and $530 \mu\text{m}$ in the transverse position. It is composed of 4 barrel layers and 3 endcaps layer. The intermediate region, going outwards with respect to the interaction point, is consist of 4 barrel of Silincon Strip layers parallel to the beam axis, Tracker Inner Barrel (TIB), and 3 disks of Silincon Strip at each end of the TIB, the Tracker Inner Disks, called TID. The outer volume, outside the TIB/TID, is also composed by SST but with different thick and pitches and s called Tracker Outer Barrel, TOB. At both ends of the TOB are located other Tracker EndCaps named TEC+ and TEC-, whose signs indicate the location along the $z - axis$. A schematic overview of the CMS tracking system is shown in Figure 2.8.

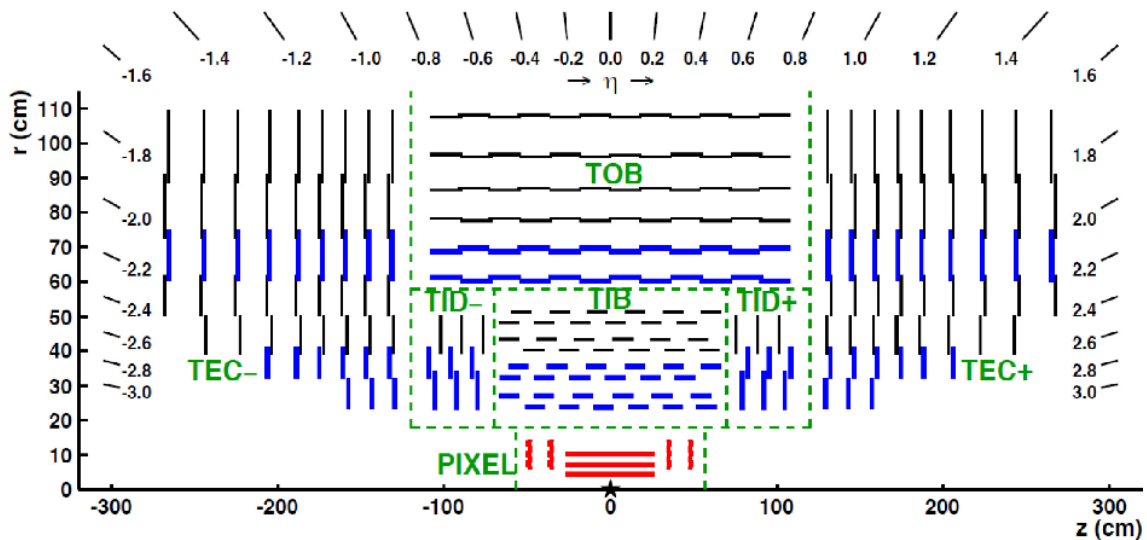


Figure 2.8: Schematic overview of the CMS tracking system.

The electromagnetic calorimeter

The ECAL [2] is an hermetic and homogeneous calorimeter made up of 75848 scintillating crystals of lead tungstate ($PbWO_4$). The design and the material chosen guarantee some important properties for a calorimeter: high granularity, fast radiation, radiation hardness, a very compact structure thanks to the high density of crystals (8.28 g/cm^3), a small Molière radius (2.2 cm) and a short radiation length ($X_0 = 0.89 \text{ cm}$). The crystals are arranged in a barrel section, forming the ECAL barrel (EB), and two endcaps, the ECAL EndCaps EE+ and EE- (the sign indicates the location along the $z - axis$). The barrel covers the pseudorapidity range $|\eta| < 1.479$ and each crystal in this part has a cross section of $\sim 22 \times 22 \text{ mm}^2$ and 23 cm corresponding to $25 X_0$. The endcap part cover a pseudorapidity range from 1.479 to 3.0, in order to allow high precision energy measurements up to $|\eta| = 2.6$. In this region crystals have a cross section of $\sim 33 \times 33 \text{ mm}^2$ and 22cm corresponding to $24.7 X_0$; they are grouped in 36 units of 1700 crystals each, called

supercrystals. The entire ECAL structure is maintained at the temperature of 0.1°C in order to maximize the yield of light. The photons are collected by photodetectors, converted to an electrical signal and then amplified in two different ways: in the barrel region, avalanche photodiodes (APDs) are used, since they are able to provide the higher gain in presence of high transverse magnetic field; in the endcaps the amplification is provided by vacuum phototriodes (VPTs) since the radiation in this region is too high to use silicon photodiodes.

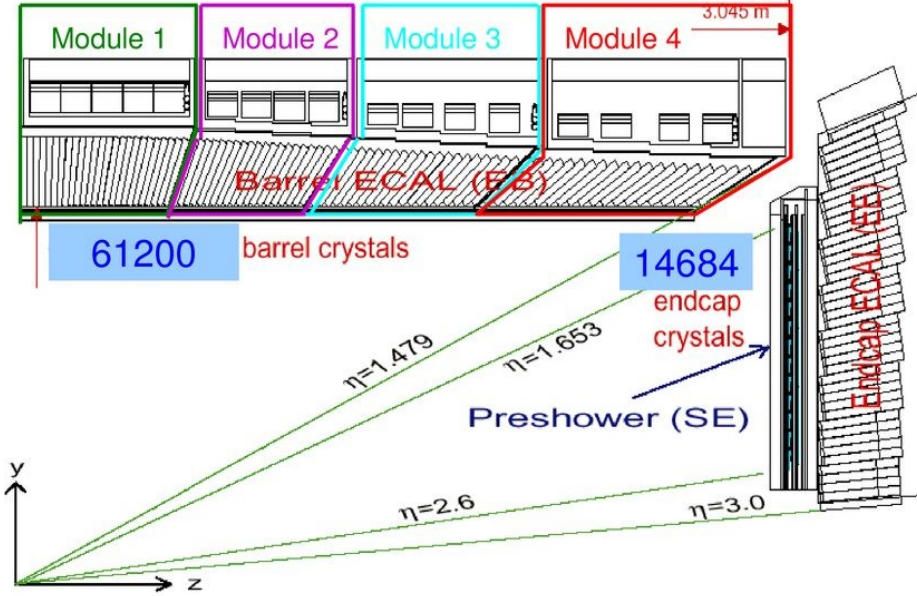


Figure 2.9: Schematic overview of the CMS ECAL.

The ECAL is also equipped with a Preshower detector, installed in front of the endcaps, for three main aims: to increase precision in the position determination, to distinguish between single high-energy photons and close pairs of low-energy photons and therefore to prevent false signals. It is made up of two lead planes followed by silicon sensors strip arranged in a grid in order to cover the crystal endcap.

One of the most important properties of an ECAL is the energy resolution that can be parametrized as:

$$\left(\frac{\sigma}{E}\right)^2 = \left(\frac{a}{\sqrt{E}}\right)^2 + \left(\frac{b}{E}\right)^2 + (c)^2 \quad (2.11)$$

where:

- a represents the stochastic term: it takes in account the statistical fluctuations of the signal in the shower containment such as fluctuations in the number of primary particles and/or the number of photons which includes fluctuations in the shower containment collected by a photomultiplier;
- b is the noise term which contains the contributions from electronic noise and pile-up energy;

- c is a constant term which considers calibration errors, the non-full containment of the shower and energy leakage.

At the CMS experiment, the energy resolution of the Electromagnetic Calorimeter is:

$$\left(\frac{\sigma}{E}\right)^2 = \left(\frac{2.8\%}{\sqrt{E}}\right)^2 + \left(\frac{0.12}{E}\right)^2 + (0.30\%)^2 \quad (2.12)$$

A schematic overview of the ECAL system is shown in Figure 2.9.

The Hadron Calorimeter

The main aim of the Hadron Calorimeter is to measure the energy of hadrons such as protons, neutrons, pions, and kaons. It is also addicted to look for hints of almost non-interacting particles such as neutrinos. The HCAL is a sampling calorimeter that allows to determine the position, energy and arrival time of particles and it is also an hermetic calorimeter to ensure the capture of every emerging particle from the collisions. The HCAL is composed by alternating layers of active material, fluorescent scintillators, and of absorber, layers of brass. The layers of active material are made up of fluorescent scintillators, while the absorber used is cartridge brass (C26000). This cartridge brass is composed by 70% of Cu and by 30% of Zn, that, with a density of 8.83 g/cm^3 , provides a radiation length of $X_0 = 1.49 \text{ cm}$ and with a nuclear interaction length of $\lambda_I = 16.42 \text{ cm}$. The different sections that compose the HCAL are: the Hadron Calorimeter Barrel (HB and HO), the Endcap (HE) and the Forward (HF) section. The HB and HE regions cover respectively the pseudorapidity range of $|\eta| < 1.3$ and of $1.3 < |\eta| < 3$. The Forward sections (HF) are located 11.2 m away from the interaction point, covering the pseudorapidity range $3 < |\eta| < 5.2$. It is made up of quartz fibres embedded within a 165 cm long steel absorber and uses a Cherenkov-based technology. The Hadron Calorimeter Outer (HO) is composed by additional scintillators that are placed outside the solenoid to ensure adequate sampling depth and to measure late shower development. In Figure 2.10 a schematic view of the HCAL is given.

Also for HCAL it is possible to refer to the energy resolution in terms of 2.11. At the CMS experiment the energy resolution for the Hadronic Calorimeter is:

$$\left(\frac{\sigma}{E}\right)^2 = \left(\frac{0.8470}{\sqrt{E}}\right)^2 + (7.4\%)^2 \quad (2.13)$$

The superconducting magnet

The magnet is a superconductive coil surrounding the tracker and calorimeters, which provides the detector with a 3.8 T magnetic field. The purpose of the magnet is to bend the trajectory of charged particles in the detector, so to measure the respective transverse momentum. An iron return yoke is located around the magnet to avoid border effects, and to bend the lines of force in a way to provide a circa constant magnetic field of 1.8 T magnitude also outside of the Solenoid bore.

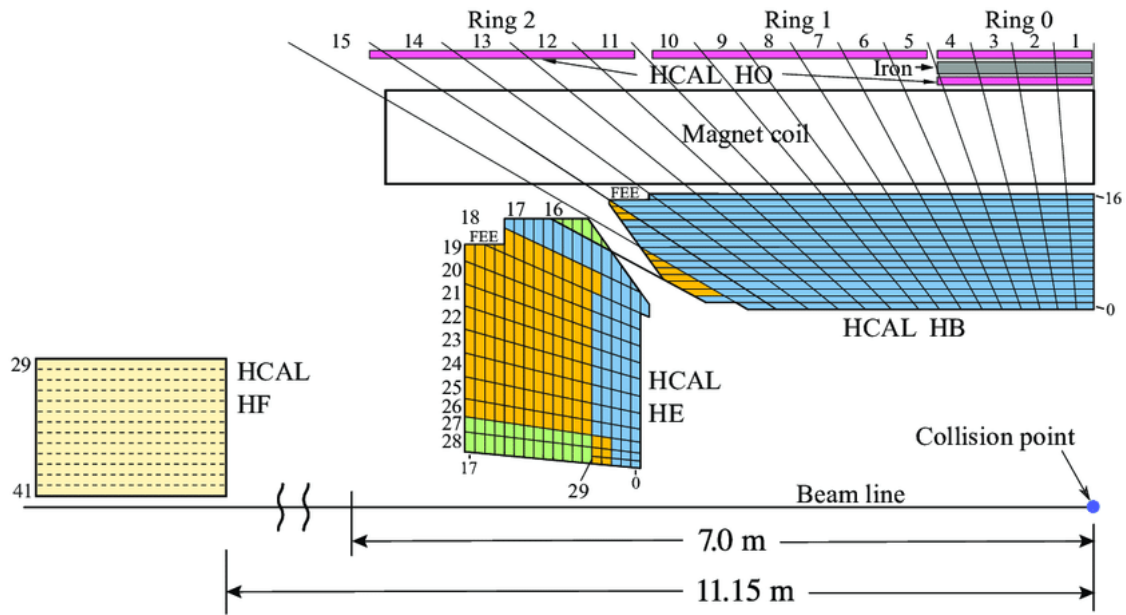


Figure 2.10: Schematic overview of the CMS HCAL.

The Muon System

The CMS muon detection system could be considered the flagship of the entire CMS detector. The collection of information of muons coming from proton-proton collisions is crucial in particles analyses since they appear in many SM as well as new physics model, and have a clean signature with respect to other particles. The Muon System has 3 functions: muon identification, momentum measurement, and triggering. Good muon momentum resolution and trigger capability are enabled by the high-field solenoidal magnet and its flux-return yoke. The latter also serves as a hadron absorber for the identification of muons. The Muon System is located in the region outside the magnet: the presence of the return yoke allows the presence of an approximately constant magnetic field of 1.8 T in the opposite direction with respect to the one inside the magnet. Muons with energy below the TeV scale lose energy mainly due to ionization, so they can penetrate several meters with few interactions with the matter in the tracker and in the calorimeters: this is the main reason of the particular position of the Muon System. However, muons are charged particles so they leave a trail in the tracking system. In this way, by combining the hits coming from the muon system and the tracker, it is possible to perform an optimal reconstruction of the muon path and to perform a precise measurement of their momentum. The muon system covers an area of about 25000 m², therefore the detectors of choice have to be reliable, robust and of contained costs. The original design of CMS used three different kinds of gas detector: Drift Tubes (DTs), Cathode Strip Chambers (CSCs), and Resistive Plate Chambers (RPCs). Subsequently further gas detectors were introduced, which will be discussed in detail in Section 2.4.

- **The Drift Tubes** are placed in the barrel and they cover a pseudorapidity range up to 1.2. The DTs are divided into 4 stations. In the first 3 stations, there are 2 layers of 4 chambers each, that measure the $r - \phi$ coordinate of the muon, and one layer of 4 chambers to measure the z coordinate. To avoid dead spots, each cell of the

chamber is divided by an half-cell width with respect their neighbour

- **The Cathode Strip Chambers** are placed in the two endcaps and cover the range $0.9 < |\eta| < 2.4$. The CSCs have a good segmentation, a fast response time, and an high radiation resistance, these properties are needed in the endcaps, where muon and background rates are higher and the magnetic field is not uniform. The cathode strips of each chamber provide position measurements in the $r - \phi$ plane. The anode wires allow to measure the pseudorapidity and the beam-crossing time of every muon. In each endcap there are four stations of CSCs.
- **The Resistive Plate Chambers** are placed both in the barrel and the endcaps. The RPCs provide an high time resolution, while the spatial resolution is lower than th DTs and CSCs. The RPCs are double-gap chambers, operated in avalanche mode to ensure good operation at high rates. In the barrel muon system there are 6 layers of RPCs, while in the endcaps there is one layer for each of the four stations. In the first two stations of the barrel two layers of RPCs are located, while just one in the last two station of DTs.

A characteristic of the DT and CSC subsystems is that they can each trigger on the p_T of muons with good efficiency and high background rejection, independent of the rest of the detector. The Level-1 trigger p_T resolution is about 15% in the barrel and 25% in the endcap. Due to the fast response of the RPCs, even low p_T tracks, that may stop before reaching the outer two stations, could be triggered.

The Trigger System

The entire amount of informations coming from all the LHC collision events is characterized by a high interaction rates that makes impossible, at LHC, to store the huge amount of data. Is required, hence, to select only the potentially interesting events reducing the rate to a few hundred events per second. The event selection is performed by the Trigger System in two steps called Level-1 (L1) Trigger and High-Level Trigger (HLT). The L1 Trigger is implemented with a wide use of programmable electronics, while the HLT uses a software filter system working on about one thousand of commercial processors. Together they manage to reduce the rate by a factor of 10^6 . The Figure shows the scheme of the overall architecture of the CMS Trigger system. The Level-1 Trigger system has the hard task to provide a fast and automatic event selection by looking for simple signs of interesting physics (e.g. particles with a large amount of energy). The trigger is based coarsely segmented data coming from the calorimeters and the muon system; the high-resolution data are holded in pipelined memories in the front-end electronics while the trigger is working. The Level-1 trigger is organized in local, regional and global components (see Figure 2.11).

The local components are also called Trigger Primitive Generators (TPG), and they are based on energy deposits in calorimeter trigger towers and track segments or hit patterns in muon chambers. The regional triggers use a pattern logic to sort trigger objects like electron, photon or muon, in limited spatial regions. The global components, Global Calorimeter and Global Muon Triggers, determine the highest-rank calorimeter and the number of trigger objects across the entire experiment and transfer them to the Trigger

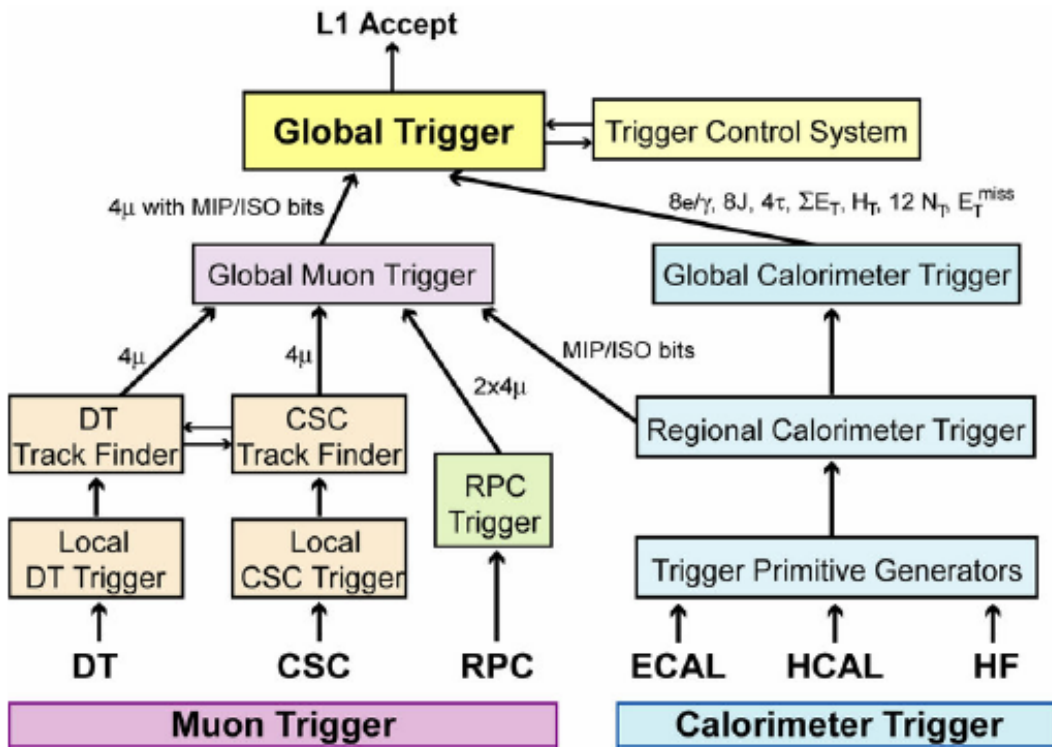


Figure 2.11: Architecture of the Level-1 Trigger.

Control System (TCS). This last module takes the final decision based on algorithm calculations and on the readiness of the sub-detectors and the DAQ. The Level-1 Accept (L1A) decision is communicated to the sub-detectors through the Timing, Trigger and Control (TTC) system. The architecture of the L1 Trigger can be seen in Figure 2.11. The allowed L1 Trigger latency, between a given bunch crossing and the distribution of the trigger decision to the detector front-end electronics, is $3.2 \mu\text{s}$. The processing must therefore be pipelined in order to enable a quasi-deadtime-free operation. The final decision to reject or to accept an event is taken by the HLT. It has the access to the complete read-out data and it performs an analysis based on the physical objects present in the event. For example events with bad vertices reconstruction or events with final objects characterized by a too low momenta are immediately refused by the HLT.

2.4 Muon system upgrade with Triple-GEM detectors

The CMS detector has been running smoothly at world-record proton-proton center-of-mass energies up to 13 TeV, with an LHC luminosity exceeding $10^{34} \text{ cm}^{-2}\text{s}^{-1}$, as described in Section 2.3. The SM was tested in an unprecedented energy regime and with high precision. To extend the sensitivity for new physics searches, a major upgrade of the LHC has been decided and is being prepared, the High Luminosity LHC (HL-LHC). The integrated luminosity will increase tenfold with respect to the original design values, as shown in Table 2.3, which summarizes some key parameters at LHC and HL-LHC for proton-proton running.

The projected evolution of instantaneous and integrated luminosity with time is shown

	LHC Design	HI-LHC Design	HI-LHC Ultimate
Peak Luminosity ($10^{34} \text{cm}^{-2} \text{s}^{-1}$)	1.0	5.0	7.5
Integrated Luminosity (fb^{-1})	300	3000	4000
Number of Pileup event	~ 30	~ 140	~ 200

Table 2.3: Characteristic parameters for HL-LHC data taking in comparison to original design values.

in Figures 2.12 and 2.13, for the design scheme and also for an ultimate scenario, which can possibly be reached by exploiting all LHC margins.

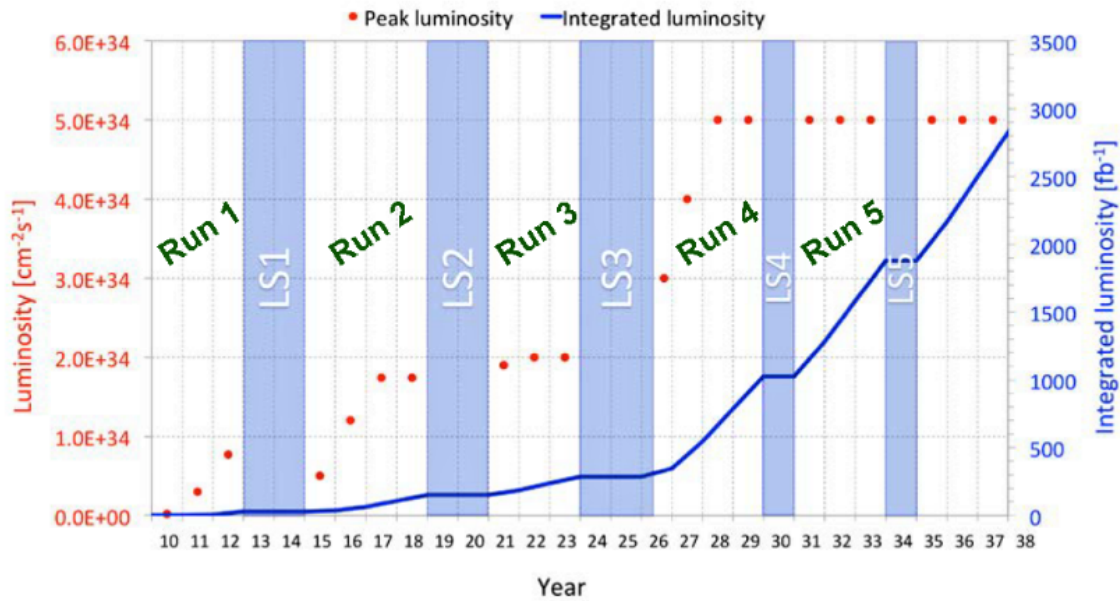


Figure 2.12: The LHC schedule and the design values for instantaneous and integrated luminosity. The data taking periods in between the long shutdowns (LS) are labeled Run 1, Run 2, etc.

The high luminosity data taking period with the upgraded LHC[3] is called *Phase 2* and is expected to last from 2026 till 2038. The HL-LHC will increase the projected integrated luminosity of 300fb^{-1} by an order of magnitude to 3000fb^{-1} in the coming two decades, for both the CMS and ATLAS detectors. This upgrade program is necessary to fully exploit the physics potential of the LHC. For example, the searches for new physics will be extended to exotic models, with challenging signatures from the experimental point of view: long-lived particles decaying leptonically, final states with low p_T muons, heavy slowly moving charged particles, or highly boosted dimuons, requiring improved muon detection and trigger capabilities. The HL-LHC upgrade of the accelerators and of the LHC detectors will be implemented mainly during the *Long Shutdown 3* (LS3) but some installation had taken place during earlier LHC shutdowns. One of the most important upgrades of the CMS detector during the long shutdown 2 (LS2) interested the muon system and it was designed to improve the muon trigger and tracking performance in the prospected high luminosity environment. There are three types of muon upgrades proposed for Phase-II:

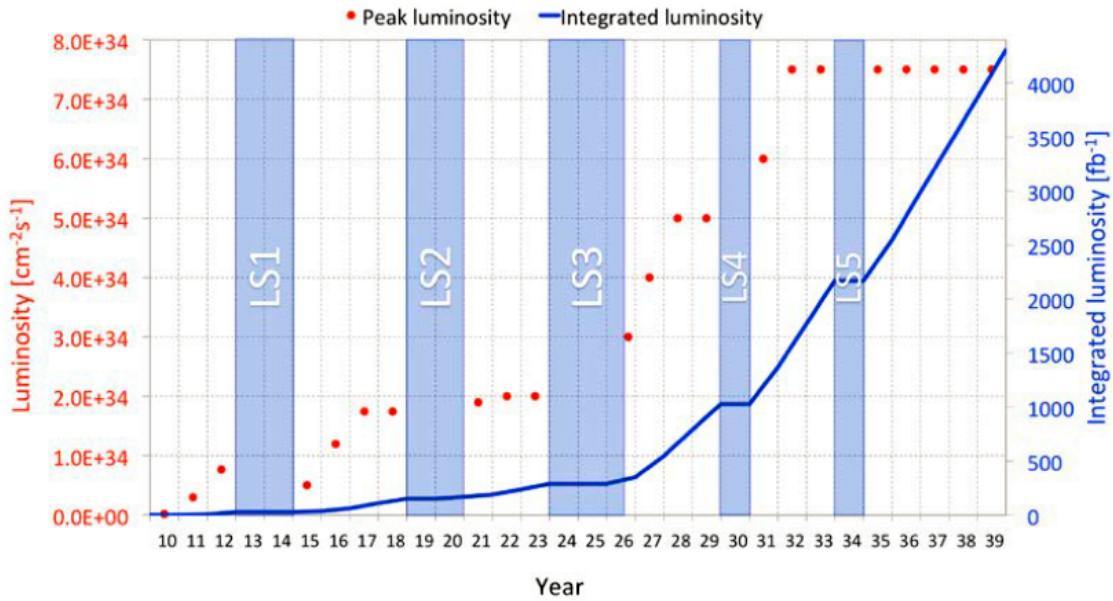


Figure 2.13: The ultimate figures for instantaneous and integrated luminosity.

- upgrades of existing muon detectors and associated electronics that ensure their longevity and good performance;
- additional muon detectors in the forward region $1.6 < |\eta| < 2.4$ to increase redundancy and enhance the trigger and reconstruction capabilities;
- extension of muon coverage up to $|\eta| = 3$ or more behind the new endcap calorimeter to take advantage of the pixel tracking coverage extension.

In this section, we focus on the first and second type of upgrade proposed. The technology chosen for the upgrade is that of the Micro Pattern Gaseous Detectors (MPGDs), and specifically the Gaseous Electron Multiplier or, more briefly, GEM⁴. As shown in section 2.3, the DT and CSC provide precise measurement points for muon identification and triggering for $|\eta| < 2.4$. In addition, the RPC provide an extra muon trigger for $|\eta| < 1.6$. The main task of the GEM detectors is to add redundancy to the muon system in the $1.6 < |\eta| < 2.4$ pseudorapidity region, where the amount of detection layers is lowest while the background rates are highest and the bending of the muon trajectories is small due to weaker CMS magnetic field. The GEM detectors are the most suitable thanks to their fast response and the reduced avalanche size.

The first station installed in the CMS detector is the so-called **GE1/1**[5], shown in the quadrant cross-section of CMS in Figure 2.14. Since forward RPCs were envisioned in the original conception of the CMS muon system, there is space available within CMS for installation of a sufficiently compact (thin) detector to respect the tight geometrical limitations. The proposed GE1/1 detector utilising GEM technology is an excellent choice for this region, due to its thin profile and the ability of operating well at particle fluxes far above those expected in the forward region under HL-LHC conditions. The denomination GE1/1 refers to the CMS terminology, used for the muon stations: the letter G

⁴see Chapter 3, Section 3.4

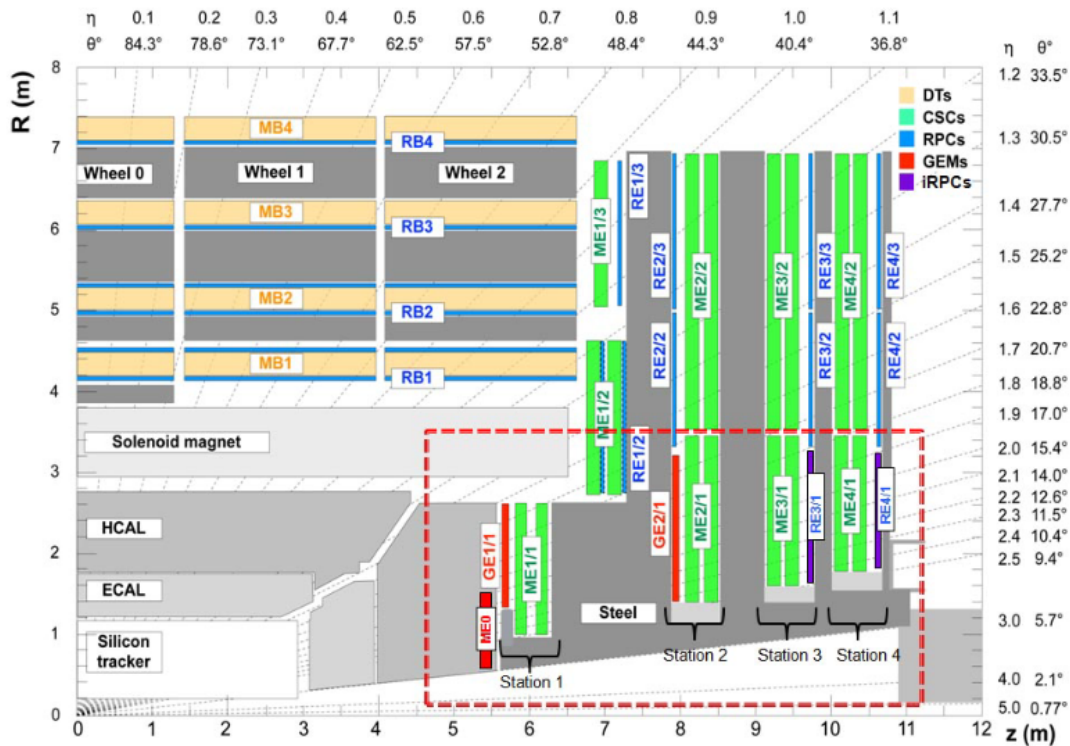


Figure 2.14: A quadrant of the muon system, showing DT chambers (yellow), RPC (light blue), and CSC (green). The locations of new forward muon detectors for Phase-II are contained within the dashed box and indicated in red for GEM stations (ME0, GE1/1, and GE2/1) and dark blue for improved RPC stations (RE3/1 and RE4/1) [4]

indicates the GEM technology, the letter E indicates this is an endcap muon station, the first '1' indicates that it is part of the first muon station encountered by particles from the interaction point, the second '1' indicates that it is the first ring of muon chambers going outward in radius from the beam line. Furthermore, the CMS plans include the installation of two more detectors [6]: **GE2/1** and **ME0**, utilizing GEM technology likewise. GE2/1 is part of the second muon station encountered by particles from the IP. The label ME0 uses 'ME' to indicate a muon endcap system and '0' to indicate that this new muon station is located in front of the original muon endcap system, i.e. closer to the IP than any other muon detector in the endcap. The ME0 detector aims to take advantage of the extension of the CMS inner tracking capabilities in order to extend efficient muon identification and triggering capabilities up to $|\eta| \sim 2.8$. In Figure 2.15 the steps related to the muon system upgrade are illustrated. Finally, in the 3rd and 4th muon stations, improved RPC (**iRPC**) detectors, denoted RE3/1 and RE4/1, will provide much-needed redundancy at modest cost, with benefits to neutron-induced background reduction for the trigger and offline reconstruction (see Figure 2.14).

2.4.1 Improvement of the L1 muon trigger rate

For good performance of the muon trigger and offline muon identification in the presence of background, delta rays, bremsstrahlung, etc., it is important to record a sufficient num-

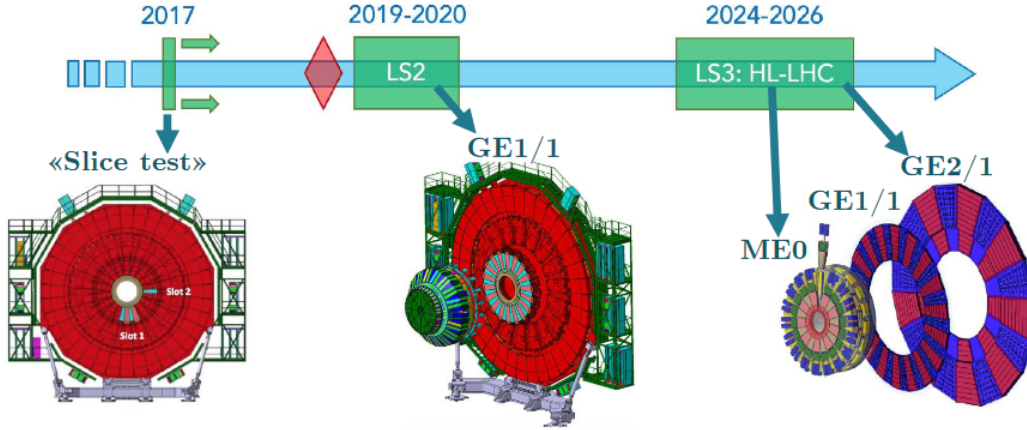


Figure 2.15: From left to right: test installation of 5 GE1/1 detectors (Slice Test); installation of GE1/1 during LS2 consisting on 144 Triple-GEM detectors to cover $1.55 < |\eta| < 2.2$ pseudorapidity region and, finally, installation of ME0 and GE2/1 detectors during LS3 that covers respectively $1.6 < |\eta| < 2.4$ and $2.0 < |\eta| < 2.8$ pseudorapidity region.

ber of muon detector hits on each track. Consequently, among the challenges associated with the forward region of the muon system, maintaining an efficient and reliable triggering is the most difficult one. With no upgrades, the muon trigger rates would increase significantly at the HL-LHC luminosities, particularly in the region $|\eta| > 1.6$. High muon trigger rates in the forward part of the detector are driven by the fast drop in the magnetic field towards high $|\eta|$, which results in a decreased bending of muon trajectories as they traverse the CMS muon system. As the measurement of muon transverse momentum by the Level-1 muon trigger is based on the observed bending of muon trajectories, the degradation of transverse momentum resolution in the forward region leads to an increased probability of low transverse momentum particles being reconstructed as high transverse momentum muons. The GE1/1 muon station offers an improvement of the L1 muon trigger rate. This is justified considering that the bending of muons within the CMS solenoid is largest at the position of the first muon station and the longer path length traversed by muons within the first muon stations (GE1/1 and CSC station ME1/1) drastically reduces the large contribution to the overall L1 muon trigger rate coming from the higher rate at increasing $|\eta|$. Figure 2.16 shows the impact of the GE1/1 muon station on the reduction of the L1 trigger rate with respect to the current muon system. In particular, the L1 muon trigger thresholds can be maintained at low p_T values, so that the efficiency for capturing interesting physics processes featuring soft leptons, ranging from Higgs precision measurements to new physics searches, can be kept high.

2.4.2 Radiation Tolerance: background nature and rates

During Run-I the CMS muon system operated well inside its design radiation tolerance and no aging effects were observed: all muon subsystems performed very stably and with high efficiency ($> 95\%$). Given the conditions foreseen HL-LHC, the muon detectors and their associated electronics must operate at much higher luminosities, therefore an upgrade is necessary, as we have seen in the previous section 2.4. Background radiation

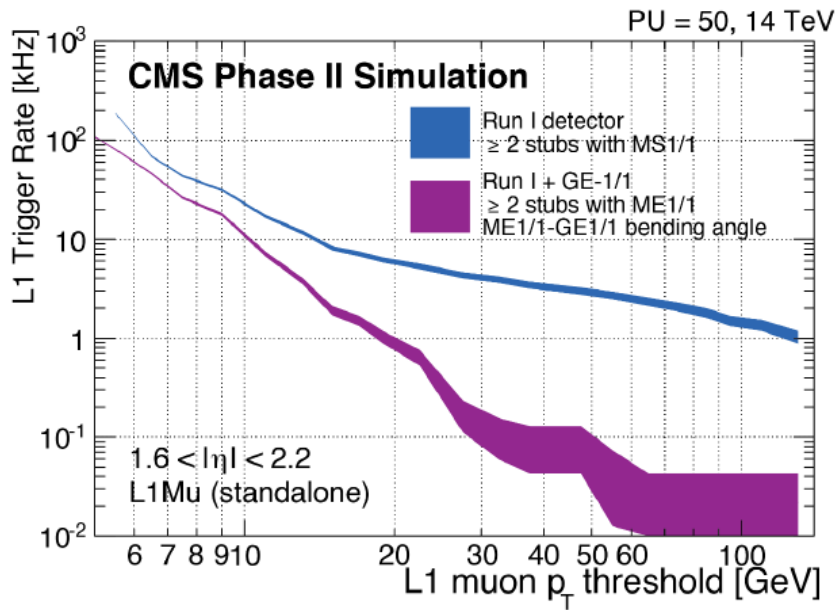


Figure 2.16: Level 1 muon trigger rates before and after the GE1/1 upgrade at a luminosity of $2 \times 10^{34} \text{ cm}^{-2}\text{s}^{-1}$ for constant efficiency of 94%. MS1/1 denotes the first endcap muon station Level 1 trigger in both cases, i.e. with CSC-only or with the combination CSC and GEM trigger information. With the addition of GE1/1, the bending angle between the two stations can be used and the trigger rate is greatly reduced.

in the muon system arises from low-energy gamma rays and neutrons from p-p collisions, low-momentum primary and secondary muons, punch-through hadrons from the calorimeters, muons and other particles produced in the interaction of the beams with collimators, residual gas and beam-pipe elements. All major background sources affect mostly detectors at the highest pseudorapidity. In the most forward region ($|\eta| > 1.6$) of CMS, where the neutron flux is highest, the total flux for neutrons with $E > 100 \text{ KeV}$ will be about $6 \times 10^{11} \text{ cm}^{-2}$, after ten years of operation at the LHC design luminosity of $10^{34} \text{ cm}^{-2}\text{s}^{-1}$. At the HL-LHC neutron fluences are expected to be five times larger than at LHC, over ten years of operation at $5 \times 10^{34} \text{ cm}^{-2}\text{s}^{-1}$. Even considering an upgrade of the detector background shielding, such extremely high radiation background will still exceed the design tolerances of several components of the muon system. Thus, it is necessary to require a new assessment of the detector and electronics longevity (radiation tolerance, aging of components, long-term behavior) and performance (rate capability, detection efficiency, pattern recognition, resolution) under accelerated aging tests. During LHC Run-I, background rates in the muon detectors have been measured at 8 TeV for several luminosity values up to $\sim 7 \times 10^{33} \text{ cm}^{-2}\text{s}^{-1}$. In the CSC system, the measured rates extrapolated linearly to the LHC design luminosity of $10^{34} \text{ cm}^{-2}\text{s}^{-1}$ and 14 TeV center-of-mass energy, will reach 900 Hz/cm^2 at the innermost part of the ME1/1 chambers. Similar measurements have been done with the RPCs, both endcap and barrel, and barrel DT chambers (Table 2.4).

Detector	Bck. rate LHC	Bck. rate HL-LHC	Max. rate tested	Max int. charge 3000 fb^{-1}	Max int. charge tested
----------	------------------	---------------------	---------------------	---	---------------------------

DT	5	25	100	0.15 C/cm	0.48 C/cm
CSC	900	4500	20000	0.3 C/cm	0.35 C/cm
RPC	50	250	300	0.27 C/cm	0.05 C/cm

Table 2.4: Expected maximum background rates at $\sqrt{s}=14$ TeV and LHC design luminosity of 10^{34} cm⁻²s⁻¹ and at HL-LHC peak luminosity of 5×10^{34} cm⁻²s⁻¹, and maximum rates and maximum integrated charge reached in past aging tests. Rates are given in Hz/cm².

The background in the GEM regions of CMS, instead, has been computed using the CMS-FLUKA simulation tool, including the latest CMS geometry, the detector upgrades, and the new beam pipe geometry. Additionally, the sensitivity of triple-GEM detectors to the different background contributions and energies has been modelled with the GEANT4 framework. The results of the simulation, shown in Table, indicate that the background hit rate is dominated by photons with an energy around 1 MeV.

Detector	Max. neutron flux	Max. neutron induced hit rate	Max. photon hit rate	Max. total hit rate	Total acc. charge after 10 HL-LHC years [mC/cm ²]
GE1/1	0.277	499	847	1469	6
GE2/1	0.191	343	273	672	3
ME0	3.28	5910	33900	47510	283

Table 2.5: Expected background components and their corresponding hit rates in the GE1/1, GE2/1, and ME0 regions. The total accumulated charge is calculated from the total hit rate at a typical detector gain of 2×10^4 . Flux and hit rate are expressed in Hz/cm².

2.4.3 Muon reconstruction and identification

For the measurement of muons, the single most important aspect is the 3.8 T solenoidal magnet. The magnetic flux generated by the strong central field is large enough to saturate the steel in the return yoke. The standard muon reconstruction is performed using the all-silicon inner tracker at the center of the detector and up to four stations of gas-ionization muon detectors installed outside the solenoid and sandwiched between the layers of the steel return yoke. This provides two measurements of the trajectory of each muon, resulting in a good level of redundancy and excellent momentum resolution, varying from one to few percent at 100 GeV, depending on $|\eta|$, without making stringent demands on spatial resolution and the alignment of muon chambers. The present detector and the favorable length to radius ratio allows efficient muon measurement up to a pseudorapidity of $|\eta| < 2.4$. The strong magnetic field also enables an efficient first-level trigger with an acceptable rate.

Muon reconstruction

In the standard CMS reconstruction for pp collisions, tracks from muons are reconstructed both in the inner tracker (*tracker track*) and in the muon system (*standalone-muon track*). Two reconstruction approaches are used in CMS: *Global Muon reconstruction (outside-in)* and *Tracker Muon reconstruction (inside-out)*.

In the first case, for each standalone-muon track, a matching tracker track is found by comparing parameters of the two tracks propagated onto a common surface. A global-muon track is then fitted combining hits from the tracker track and standalone-muon track, using the Kalman-filter technique. At large transverse momenta, $p_T > 200$ GeV, the global-muon fit (as well as a set of dedicated high- p_T refits combining information from tracker and muon chambers with different logics) can improve the momentum resolution compared to the tracker only fit. The standalone muon reconstruction algorithm has been updated to use also the hits coming from all the new forward muon detectors (GEM and iRPC): the test was carried out on simulations. Consequently also the Global Muon reconstruction includes those hits.

In the second approach, all tracker tracks with $p_T > 0.5$ GeV and total momentum $p > 2.5$ GeV are considered as possible muon candidates and are extrapolated to the muon system taking into account the magnetic field, the average expected energy losses, and multiple Coulomb scattering in the detector material. If at least one muon segment matches the extrapolated track, the corresponding tracker track qualifies as a Tracker Muon. For the Phase-2 era the Tracker Muon algorithm is used to match the tracker tracks also to the new segments provided by the GEM subsystem. This has several benefits: it improves the Tracker Muon performance in the overlap region with the existing muon subdetectors from the point of view of the fake rejection and redundancy of the muon system. Moreover, it allows also to extend the eta coverage up to $|\eta| = 2.8$. Track-to-segment matching is performed in a local (chamber) coordinate system, where local x is the best-measured coordinate (in the $r - \phi$ plane) and local y is the coordinate orthogonal to it for DT and CSC. Within ME0 the matching is performed in global ϕ and η coordinates. This is important for ME0 as the η granularity is much coarser than the ϕ granularity. Using local- x matching would result in a lots of mixing from the much less precise η measurements. Moreover, since ME0 provides a bending angle measurement, a track-segment match in p_T is required. All the matching criteria in ME0 become tighter with increasing muon momentum.

Muon identification definition and efficiency

The combination of different approaches provides robust and efficient muon reconstruction. The selection criteria used during Run 2 have been updated to exploit the information coming from the new forward detectors, and are optimized for the conditions expected in the HL-LHC era. The performance of the following two basic muon identification algorithms is presented:

- *Loose Muon selection.* The candidate is required to be reconstructed either by the Tracker Muon or the Global Muon algorithm. In order to extend the pseudorapidity acceptance the muon candidate is required also to be loosely identified in the ME0 detector with a selection on the track-segment matching in global η , global ϕ and in the bending angle tuned for muons of p_T between 2 and 4 GeV.

- *Tight Muon selection.* For this selection, the candidate must be reconstructed both as a Global Muon and a Tracker Muon. The Global-Muon track fit must have a $\chi^2/d.o.f$ less than 10 and must include measurements in more than five inner-tracker layers, including at least one pixel hit, and at least one muon chamber hit. In addition, the Tracker Muon algorithm must find matching segments in at least two muon stations. In order to extend the $|\eta|$ acceptance the muon candidate is required also to be clearly identified in the ME0 detector with a selection on the track-segment matching in global η , global ϕ and in the bending angle tuned for muons with p_T between 3 and 5 GeV.

The muon reconstruction and identification efficiency is calculated as the fraction of simulated muons that are associated to a reconstructed muon passing a given identification selection criteria. The association between simulated and reconstructed muons is performed by matching the simulated signals on each detector layer to the corresponding reconstructed hits, used to fit the muon track. Figure 2.17 shows instead the identification

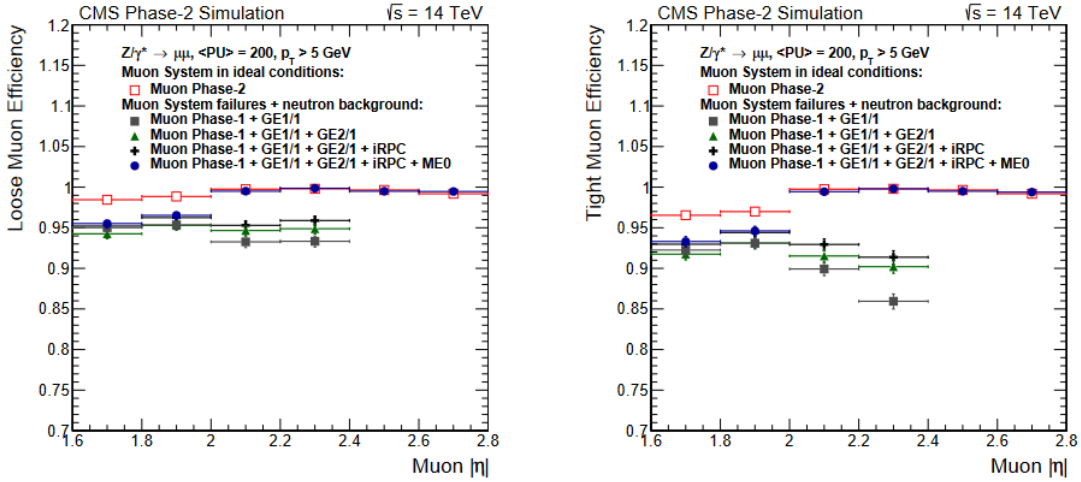


Figure 2.17: Loose (left) and Tight (right) Muon reconstruction and identification efficiency in DY events as a function of the simulated muon $|\eta|$, at pileup 200, obtained including the simulation of muon system aging and neutron background. The performance is measured applying several upgrade scenarios incrementally, from the Phase-1 detector (with the addition of GE1/1) to the full scope of the muon system upgrade.

efficiency of Loose and Tight Muons at pileup 200 when the muon system degradation and the neutron background hits are both simulated. The upgraded detector allows for the identification of muons at high pileup with the same efficiency as the Phase-1 detector with lower pileup. The aged detector shows a drop in efficiency of approximately from 5 to 15%. The impact of the new muon detectors in the forward region is clearly visible, up to the $|\eta|$ coverage provided by ME. Finally, it is useful to make a comparison between the muon reconstruction efficiency during Phase-1 and the aforementioned upgrade phase. Figure 2.18 shows Tag-and-probe⁵ efficiency for muon reconstruction and identification in 2015 data, simulation and ratio for loose and tight muons with $p_T > 20$ GeV.

⁵The tag and probe method is a data-driven technique for measuring particle detection efficiencies. It is based on the decays of known resonances to pairs of the particles being studied.

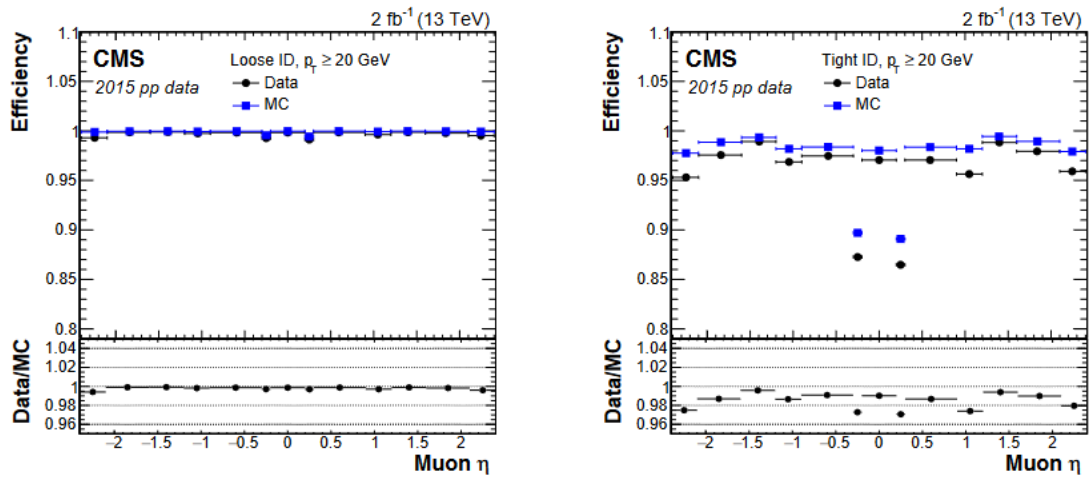


Figure 2.18: Tag-and-probe efficiency for muon reconstruction and identification in 2015 data (circles), simulation (squares), and the ratio (bottom inset) for loose (left) and tight (right) muons with $p_T > 20$ GeV. The statistical uncertainties are smaller than the symbols used to display the measurements.

Chapter 3

Gaseous Detector and CMS Triple-GEM detector systems

3.1 Introduction

For the experimental nuclear or particle physicists, knowledge of the interaction that occurs when particle or radiation encounter matter is of paramount importance, as well as the effects produced by these processes. Penetrating radiation, of course, sees matter in terms of its basic constituents, i.e., as an aggregate of electrons and nuclei and, of the constituents of the latter (nucleons). Depending on the type of radiation, its energy and, the type of material, reaction with the atoms, nuclei, or nucleons may occur through whatever channel are possible. For charged particles and photons, the most common processes are by far the electromagnetic interactions, in particular, inelastic collisions with the atomic electrons. The identification of particles created in collisions or other particles' decays is a task performed by particle detectors. While the history of nuclear and elementary particle physics has seen the development of many different types of detector, all are based on the fundamental principle: the transfer of part or all of radiation energy to the detector mass where it is converted into some other form more accessible to human perception. The gaseous detectors, for example, are designed to directly collect the ionization electrons to form an electric current signal. In this chapter an overview of the passage of radiation through matter and gaseous detector are given. In particular, at the end of this chapter a details description of the gaseous detectors used in the CMS Muon System upgrade is specified: the Triple-GEM detector.

3.2 Passage of Radiation Through Matter

Radiation contains two types of particles: charged particles (electrons, protons, muons, alpha particles, and other heavy charged ions) and neutral particles (photons, neutrons, etc). In general, two principal features characterize the passage of charged particles through matter: a loss of energy by the particle and a deflection of the particle from its incident direction. These effects are primarily the result of two processes:

- inelastic collision with the atomic electrons of the material;
- elastic scattering from nuclei.

These reactions occur many times per unit path length in matter, and it is their cumulative result which accounts for the two principal effects observed. These, however, are by no means the only reactions which can occur. Other processes include, for example, emission of Cherenkov radiation, nuclear reactions, bremsstrahlung. Hence, charged particles interact with matter primarily through Coulomb force. Coulomb interactions between the passing charged particle and the medium lead to excitation and ionization of the atoms of the medium itself. In a gaseous medium, the particles passing by can immediately create an ionization path and thus release electrons from the gas molecules. But it could also be that first an intermediate excited species is created. If the excitation energy of this species A is higher than the ionization energy of another species B present in the gas, then A can de-excite by liberating electrons from the B-molecules in the gas. All these created electrons are called primary electrons. These electrons can still lose their excessive energy by further ionizing the gas, creating secondary electrons. Other electromagnetic interactions like Bremsstrahlung, Cherenkov radiation, or nuclear reactions are negligible.

3.2.1 Interaction of charged particles with matter: the Bethe-Bloch formula

The electromagnetic energy loss of a heavy ($m > m_e$) charged particle traversing a medium even with thin materials is a statistical process resulting from the succession of many discrete interactions. As it penetrates the material the particle scatters inelastically upon molecules, electrons and nuclei. If the energy deposit is larger than the binding energy of the atom, ionization takes place. Otherwise the collision leads to an excitation of the atoms in the material. Bethe and Bloch derived in the framework of relativistic quantum mechanics an expression for the average differential energy loss due to electromagnetic interaction and, known in fact as the *the Bethe-Bloch formula*:

$$-\frac{dE}{dx} = 2\pi N_a r_e^2 m_e c^2 \rho \frac{Z}{A} \frac{z^2}{\beta^2} \left[\ln \left(\frac{2m_e \gamma^2 v^2 W_{max}}{I^2} \right) - 2\beta^2 - \delta - 2\frac{C}{Z} \right] \quad (3.1)$$

where

- $2\pi N_a r_e^2 m_e c^2 = 0.1535 \text{ MeVcm}^2/\text{g}$,
- $r_e = 2.817 \times 10^{-13} \text{ cm}$ is classical electron radius,
- m_e is the electron mass,
- N_a is Avogadro's number,
- I is the mean excitation potential,
- Z is the atomic number of absorbing material,
- A is the atomic weight of absorbing material,
- ρ is the density of absorbing material,

- z is the charge of incident particle in unit e ,
- $\beta = \frac{v}{c}$ is that of the incident particle,
- $\gamma = \frac{1}{\sqrt{1-\beta}}$,
- δ is the density correction,
- C the shall correction,¹
- W_{max} the maximum energy transfer in a single collision.

The minimum of $\frac{dE}{dx}$ can be found at $\beta \approx 0.95$, almost independently of the medium. In practical cases, most relativistic particles have energy-losses close to this minimum. They are called minimum ionizing particles, or MIPs. For higher energies the energy-loss rises slightly, due to large energy transfers to a few electrons. At lower energies we enter a range of very high energy-loss. Photoelectrons with energies of a few KeV (e.g. from X-rays) or α -particles of a few MeV (e.g. from ^{90}Rn) are examples of these heavily ionizing particles. In a mixture the energy losses in the different gas types can be added taking into account the appropriate weight factors, or the percentage of the respective gases.

3.2.2 Interaction of photons with matter

The behavior of photons in matter is dramatically different from that of charged particles. In particular, the photon's lack of an electric charge makes impossible the many inelastic collisions with atomic electrons characteristic of charged particles. Instead, the main interactions of x -rays and γ -rays in matter are:

- Photoelectric Effect;
- Compton Scattering (including Thomson and Rayleigh Scattering);
- Pair Production.

The attenuation suffered by a photon beam traversing a medium of thickness x and with N molecules per unit volume can be shown to be exponential with respect to the thickness, i.e.,

$$I(x) = I_0 \exp(-\sigma N x) = I_0 \exp(-\mu \rho x) \quad (3.2)$$

where I_0 is the incident beam intensity, x the thickness of absorber, μ is the absorption coefficient, ρ the medium density, σ is the total cross section for photon-matter interaction and determines the probability of absorption. This total cross section is the sum of the cross section for all the individual processes that might occur: photoelectric absorption, Compton scattering and pair production. The processes above each dominate in a specific energy range, which depends strongly on the atomic number (Z), as can be seen in Figure 3.1. In the low energy range considered in this work, up to several KeV, photo-electric

¹The quantities δ and C are corrections which are important at high and low energies respectively. The *density effect* arises from the fact that the electric field of particle also tends to polarize the atoms along its path. Because of this polarization, electrons far from the path of the particle will be shielded from the full electric field intensity.

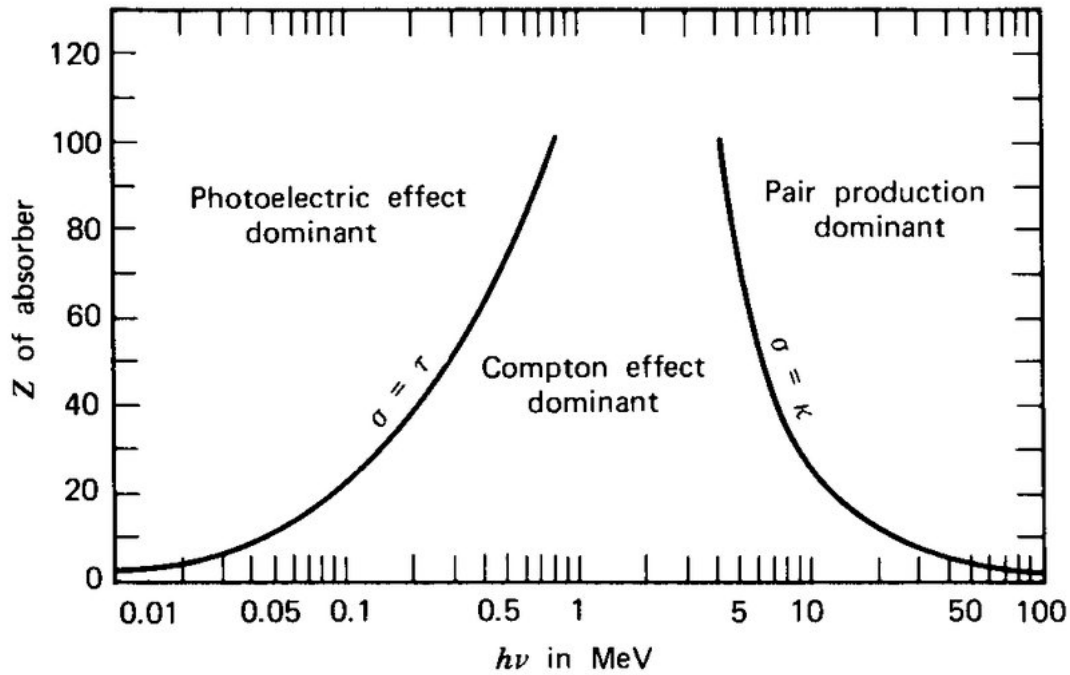


Figure 3.1: Relative importance of the photoelectric effect, the Compton effect and the production of pairs in different absorbing media (Z) and at different energies.

absorption is the most important process. The mass attenuation coefficient is related with the absorption coefficient:

$$\mu = \frac{N_A}{N} \sigma_{tot} = \frac{N_A}{N} (\sigma_{PA} + \sigma_{CS} + \sigma_{pp}) \quad (3.3)$$

with N_A Avogadro's number, and A the mass number of the absorber material.

Photoelectric Effect

The photoelectric effect is a quantum process that involves one or more transitions across the electron shells of an atom. If the energy of the incident photon $E_\gamma = h\nu$ exceeds the binding energy E_i of the electrons in the shell i , the photon is completely absorbed (see Figure 3.2). Energy and momentum are transferred to the interaction partner (a bound electron) and ionization and excitation of the atom take place. The cross section of this process has a maximum at the absorption edges and then decreases rapidly. In a gas detector an electron is emitted in a preferential direction, depending on the photon energy. Up to about 20 KeV the direction is nearly orthogonal to the direction of the incident photon, which limits the spatial resolution for photons in such a detector. The excited atom can return to its ground state through 2 competing mechanisms:

- **fluorescence:** transition of an electron from a shell with energy $E_j < E_i$ to the i -shell, with emission of a photon with energy $E_i - E_j$.
- **radiationless transition or Auger effect:** an internal rearrangement involving electrons from several lower-energy shells, resulting in the emission of an electron with an energy close to E_i .

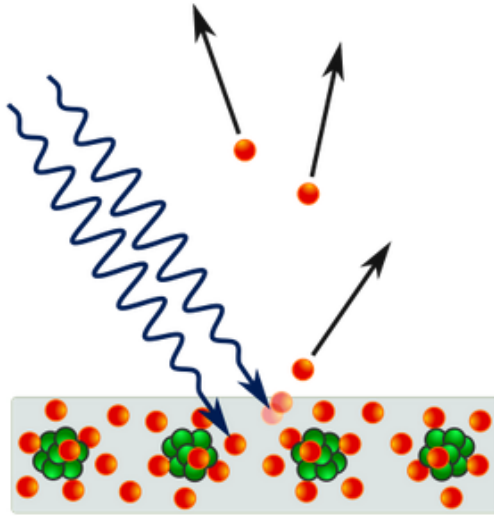


Figure 3.2: The photoelectric absorption process.

The fraction of de-excitations producing the emission of a photon is called the fluorescence yield. For the K-shell the fluorescence increases with the atomic number. In argon, for example, 15% of the photoelectric absorptions are followed by an emission of a photon of an energy just under that of the K -shell. The secondary photon with an energy just below the K -edge has a very long absorption length and can therefore escape the volume of detection. This creates the characteristic escape peak of argon, at an energy $E_\gamma - E_K$. In 85% of the cases, two electrons are emitted, one of them being an Auger.

Compton scattering

In this process, the incoming γ -ray photon interacts with the electron in the absorbing medium. A photon transfers partial energy to the electron, and hence the photon as well as electron scattered with different angles respect to its original direction. The energy transfer to the electron depends upon the angle of the scattering of the photon which can vary from zero to a large value. The equation which relates the energy transfer of the photon to the electron is simply obtained by the energy and momentum conservation according to the image shown in the Figure 3.3. In this process, an incident photon of energy $h\nu$ interacts with an electron having rest mass m_0 . The photon scatters at an angle ϕ with respect to the original direction with the transfer of a portion of its energy to the electron. The electron recoils through an angle θ with respect to the direction of the incoming photon. The equation of the energy of a scattered photon is given by:

$$h\nu' = \frac{h\nu}{1 + \frac{h\nu}{m_0c}(1 - \cos\theta)} \quad (3.4)$$

where c is speed of light. The energy transferred to the electron is given by:

$$E_{e^-} = h\nu' - h\nu \quad (3.5)$$

The maximum energy is transferred by a photon to the electron when it scatters at an angle of 180° , and no energy is transferred when it passes without interaction i.e. at 0°

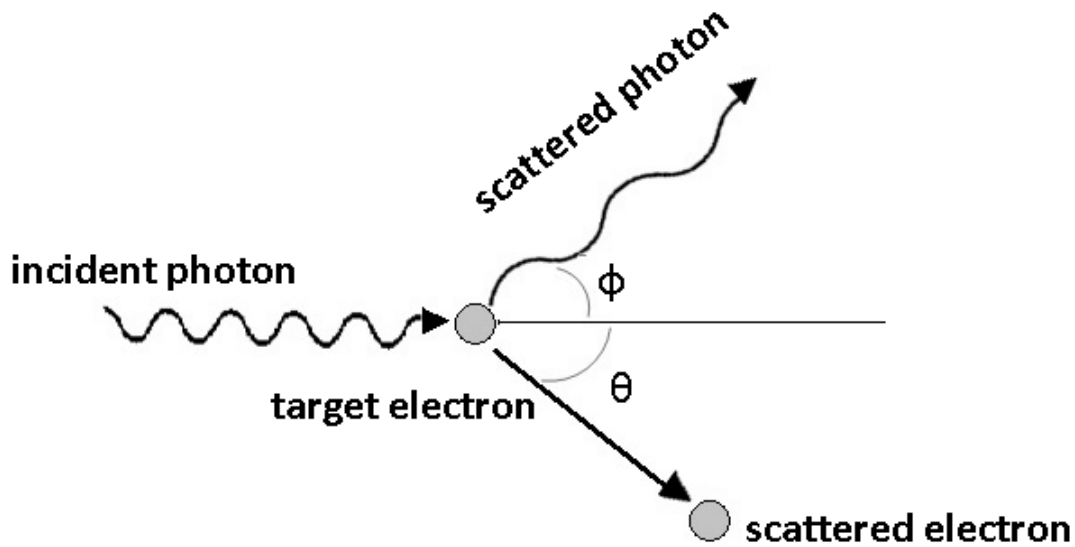


Figure 3.3: The Compton scattering process.

angle. The probability of Compton scattering increase linearly with Z i.e. the number of electrons available at the scattering target. The Klein-Nishina formula for the differential cross-section $\frac{d\sigma}{d\Omega}$ describes the angular distribution of scattered γ -ray photons as:

$$\frac{d\sigma}{d\Omega} = \frac{r_e^2}{2} \frac{1}{[1 + \gamma(1 - \cos\theta)]^2} \left(1 + \cos^2\theta + \frac{\gamma^2(1 - \cos\theta)^2}{1 + \gamma(1 - \cos\theta)} \right) \quad (3.6)$$

where r_e is the classical electron radius. Integrating of this formula over the solid angle $d\Omega$ than, gives the total probability per electron for a Compton scattering to occur.

Pair Production

The process of production of electron and positron pair from a γ -ray photon in the vicinity of the nucleus is called pair production. This reaction is only energetically possible when the energy of the gamma-ray photon is at least twice the rest mass energy of the electron (1.022 MeV). All the excess energy carried by the photon above the 1.022 MeV converts into kinetic energy shared by the positron and electron. Normally two annihilated photons produced in the slowing down process of the positron as a secondary product of their interaction as shown in Figure 3.4. The probability of pair production increases with the increase in the incoming energy of the incident γ -ray photon as well as varies approximately as the square of the atomic number of the absorber.

3.3 Gaseous Ionization Detectors

Ionization detectors were the first electrical devices developed for radiation detection. These instruments are based on the direct collection of the ionization electrons and ions produced in a gas by passing radiation. The greater mobility of electrons and ions with

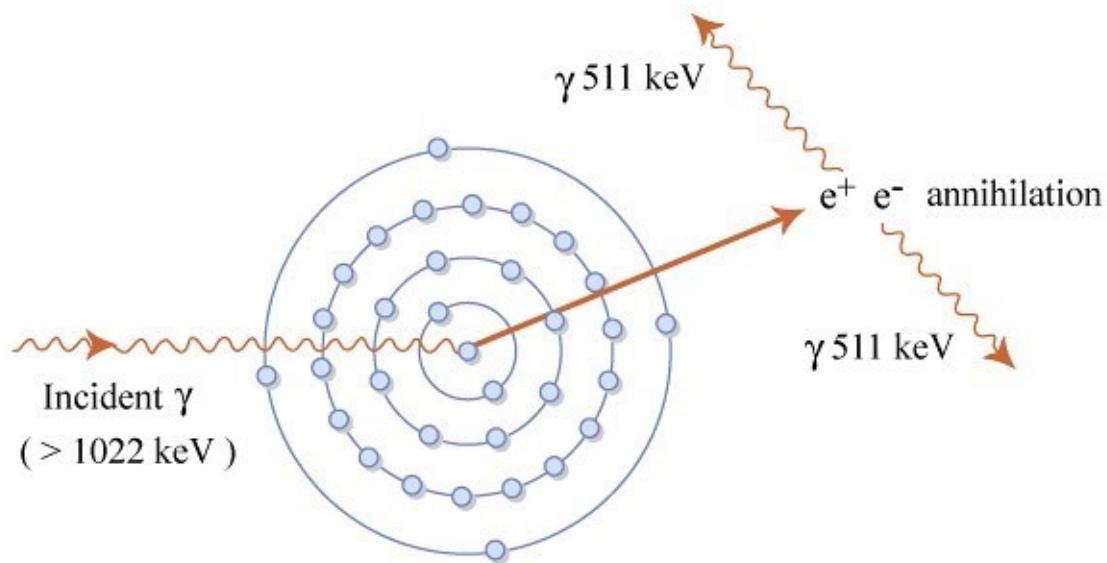


Figure 3.4: The pair production process.

reference to other mediums implies that a gas is the obvious medium to use for the collection of ionization from radiation. An example of the basic configuration of a gas device (see Figure 3.5) is given in the following. It consists of a container, a cylinder for simplicity, with conducting walls and a thin end window. The cylinder is filled with a suitable gas, usually a noble gas as argon. Along its axis is suspended a conducting wire to which a positive voltage, $+V_0$, relative to the walls is applied. A radial field is thereby established:

$$E = \frac{1}{r} \frac{V_0}{\ln(b/a)} \quad (3.7)$$

where r is the radial distance from axis; b the inside radius of cylinder; a the radius of a central wire. If radiation now penetrates the cylinder, a certain number of electron-ion pairs will be created, either directly, if the radiation is a charged particle, or indirectly through secondary reactions if the radiation is neutral. The mean number of pairs created is proportional to the energy deposited in the counter. Under the action of the electric field, the electrons will be accelerated towards the anode and the ions towards the cathode where they are collected. The current signal observed, however, depends on the field intensity as shown in Figure 3.6. At zero voltage, of course, no charge is collected and the ion-electron pairs recombine under their own electrical attraction (region I). As the voltage is raised, however, the ion-electron pairs are collected before they can recombine. In the low electric field region, in fact, some effects must be taken into account: recombination occurs when no separation of charges is observed. Other effects are attachment and charge exchange. In the first case, electrons can be captured by electronegative gases producing slow negative ions, hence, noble gases such as argon are used. A quencher is added to the

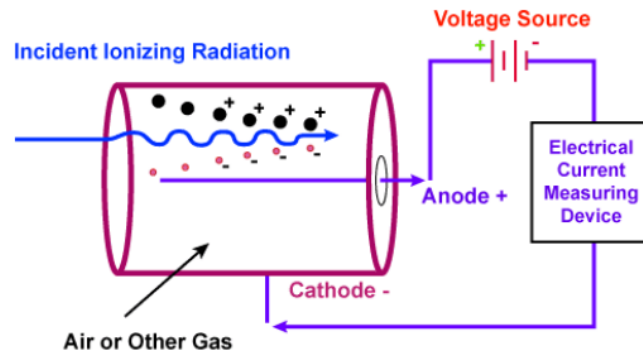
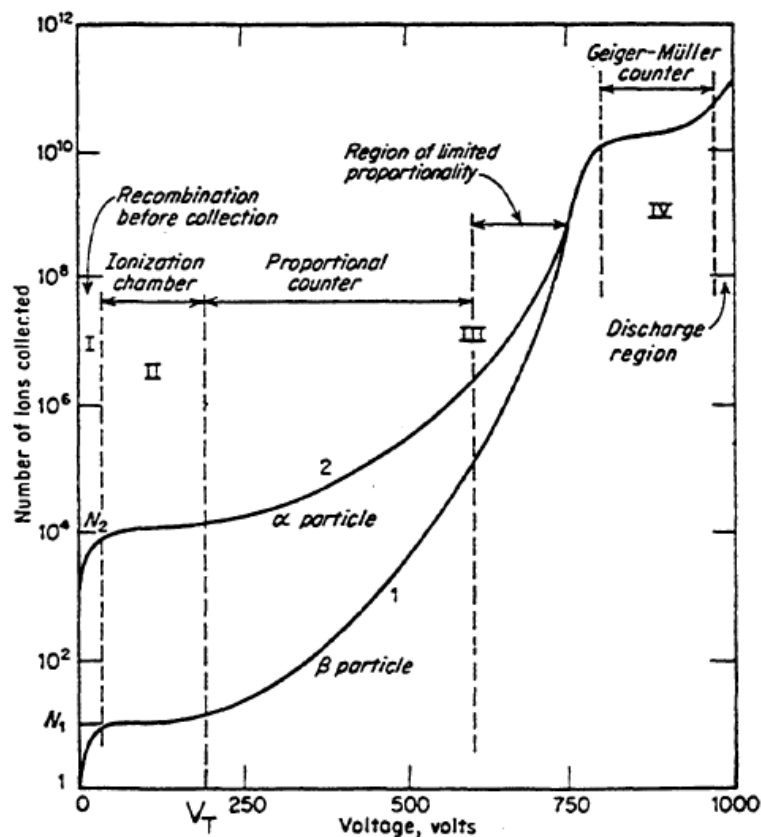


Figure 3.5: Basic construction of a simple gas ionization detector.

Figure 3.6: Number of ions collected as function of V .

argon which absorbs the high-energy photons possibly produced by atomic de-excitation and which can give rise to charges far from the trace, thus losing information on the same. In charge exchage, instead, positive ions can exchange charge with quencher's polyatomic molecules. These molecules neutralize in contact with the cathode, regain electrons and de-energize by dissociating rather than producing photons. At some point, all created pairs will be collected and further increase in voltage show no effect. This corresponds to the first flat region in Figure 3.6. A detector working in this region (II) is called an *ionization chamber* since it collects the ionization produced directly by the passing radiation. The signal current is small and must usually be measured with an electrometer. As

the voltage increases beyond region II, the current increases again with the voltage. In this regime, the electric field is strong enough to accelerate freed electrons to an energy where they are capable of ionizing gas molecules in the cylinder. The electrons liberated in these secondary ionization then accelerate to produce ionization themselves, and the process keeps on repeating itself. This results in an ionization *avalanche* or *cascade*. The number of ion-electron pairs in the avalanche is directly proportional to the number of primary electrons. What results then is a proportional amplification of the current, with a multiplication factor depending on the working voltage V . This factor can be as high as 10^6 so that the output signal is much larger than that from ionization chamber, but still in proportion to the original ionization produced in the detector. This region (III) is known as a *proportional chamber*. If the voltage is now increased beyond point III, the total amount of ionization created through multiplication becomes sufficiently large that the space charge created distorts the electric field nearby the anode. Proportionality thus begins to be lost. This is known as the *region of limited proportionality*. Increasing V even higher, the energy becomes so large that a discharge occurs in the gas. What happens physically is that instead of a single, localized avalanche at some point along the anode wire, a chain reaction of many avalanches spread out along the entire length of the anode is triggered. These secondary avalanches are caused by photons emitted by de-exciting molecules which travel to other parts of the counter to cause further ionizing events. The output current thus becomes completely saturated, always giving the same amplitude regardless of the energy of the initial event. In order to stop the discharge, a *quenching* gas must be present in the medium to absorb the photons and drain their energy into other channels. These quenchers are usually polyatomic gases, like CO_2 which can dissipate a considerable amount of energy, because they can have radiationless transitions into their excited vibrational and rotational modes. Detector working in this region are called *Geiger-Muller* or *breakdown* counters. This region (IV) is characterized by a plateau depends on the efficacy of the quencher in the gas. Finally, if the voltage is increased further a continuous breakdown occurs with or without radiation. This region, of course, is to be avoided to prevent damage to the counter.

3.3.1 Ionization and Transport Phenomena in Gases

The electrons and ions created by an incident radiation directly interacting with the gas are known as *primary* ionization. The ejected electrons can sometimes have enough energy (larger than ionization potential of the absorber and known as δ -rays) to further ionize the gas. The newly created electrons are *secondary* electrons. A second mechanism of ionization in gases is the *Penning Effect*: in certain atoms, metastable states are excited which are unable to de-excite immediately to the ground state by the emission of a photon. In such atoms, a de-excitation may occur through a collision with a second atom resulting in the ionization of the latter. A third mechanism which occurs in noble gases is the formation of molecular ions. In this process, a positive gas ion interacts with a neutral atom of the same type to form a molecular ion. Since the occurrence of the ionizing reactions above is statistical in nature, two identical particles will not produce the same number of ion-electron pairs. The number of primary ion-electron pairs is given by the

Poisson distribution:

$$P(n) = \frac{\bar{n}}{n!} e^{-\bar{n}} \quad (3.8)$$

that is the probability of obtain n primary ion-electron pairs if \bar{n} is the average numbers of primary ionizations. For gases, this average turns out to be on the order of 1 ion-electron pair per 30 eV of energy lost. The average total number of pairs formed is given by:

$$\bar{n}_{tot} = \frac{\Delta E}{W_i}. \quad (3.9)$$

where ΔE is the energy loss per unit length (~ 2 KeV/cm for a MIP in Ar) and W_i is the average energy to produce a ion-electron pair, that is different from ionization potential I_0 . Table 3.1 gives a comparison of the measured values for this average for several types of gas used in ionization detectors.

Gas	Z	A	E_{ex}	E_i	I_0	W_i	dE/dx	n_p
Ar	18	39.9	11.6	15.7	15.8	26	2.44	29.4
Kr	36	83.8	10.0	13.9	14.0	24	4.60	22
Xe	54	131.3	8.4	12.1	12.1	22	6.76	44
CO ₂	22	44	5.2	13.7	13.7	33	3.01	34
CH ₄	10	16		15.2	13.1	28	1.48	16
C ₄ H ₁₀	34	58		10.6	10.8	23	4.50	46

Table 3.1: Comparison of different values for several types of gas: E_{ex} (eV) is the minimum excitation energy, E_i (eV) minimum ionization energy, I_0 (eV) average effective ionization potential per atomic electron, W_i (eV) average energy loss to produce a ion-electron pair, dE/dx (KeV/cm) energy loss for a MIP, n_p number of primary pairs (*i.p./cm*).

Lastly, the value \bar{n}_{tot} is important since it determines the efficiency² and the energy resolution of the detector, that is given by

$$\frac{\Delta E}{E} = \frac{2.35}{\sqrt{\bar{n}_{tot}}} \quad (3.10)$$

if the incident radiation is not completely absorbed. Conversely, if the radiation is completely absorbed, the energy resolution is defined as:

$$\frac{\Delta E}{E} = 2.35 \sqrt{\frac{F}{\bar{n}_{tot}}} \quad (3.11)$$

where F is the Fano factor for the gas medium. When the energy of the incident radiation is completely released, the total number of ionizations produced is bound by the value of the total energy. Therefore, ionization events are not independent and Poisson statistic

²The efficiency is one of the main properties of any detector. Is it usually defined as the ratio between the number of events detected by the device under test and the total number of events happened in a certain time interval.

cannot be applied. The Fano factor, hence, is a correction factor that links the variance of a Poisson statistic to the experimentally measured variance. F is an intrinsic constant of the absorber medium and is a function of all the processes that lead to the deposit of energy in a detector.

Diffusion

Electrons and ions in a gas subject only to an electric field move on average along the electric field lines. Individual electrons do deviate from the average due to scattering on the atoms of the gas. Scattering leads to variations in velocity, called *longitudinal diffusion* and to lateral displacements, called *transverse diffusion*. The scattering process in each direction can be considered Gaussian on a microscopic scale. In the absence of other effects, the Gaussian law for diffusion of a localized charge distribution is the following (1-D):

$$\frac{dN}{N} = \frac{1}{\sqrt{4\pi Dt}} e^{-\frac{(x-x_0)^2}{4Dt}} dx \quad (3.12)$$

where dN/N is the fraction of charges found in the element dx at a point x after a time t . D in this equation is nothing else than the diffusion coefficient, which depends on the gas and the temperature. The standard deviation of this distribution is given by:

$$\sigma_x = \sqrt{2Dt} \quad (3.13)$$

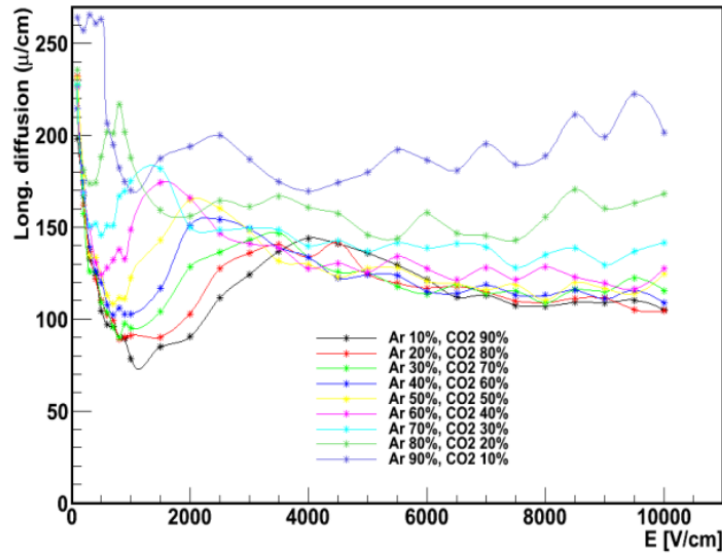


Figure 3.7: The longitudinal diffusion of Ar mixtures for different percentages.

The standard deviation can also be used to present the relative difference in diffusion between different gases. In Graph 3.7[7] the longitudinal diffusion is shown in different Ar – CO₂ mixtures.

Drift

In the presence of an electric field, a net movement of the ions along the field lines is observed. The electrons also move, instead of randomly as in the case of diffusion, in an orderly fashion along these field lines, but in the opposite direction. This phenomenon is called *drift*. Because of the higher mass of the ions, their drift speed is about three orders of magnitude smaller than that of the electrons. The easiest way to represent the drift velocity is by the mobility. In absence of other forces, we then simply get the relation:

$$\vec{u} = \mu \vec{E} \quad (3.14)$$

The speed is thus parallel to the electric field. The presence of static magnetic fields can change the drift speed. In the time between two collisions the Lorentz force then superposes a circular motion to the linear drift motion. Also electron capture in electronegative gases can occur, which then causes the total number of electrons to decline. The depen-

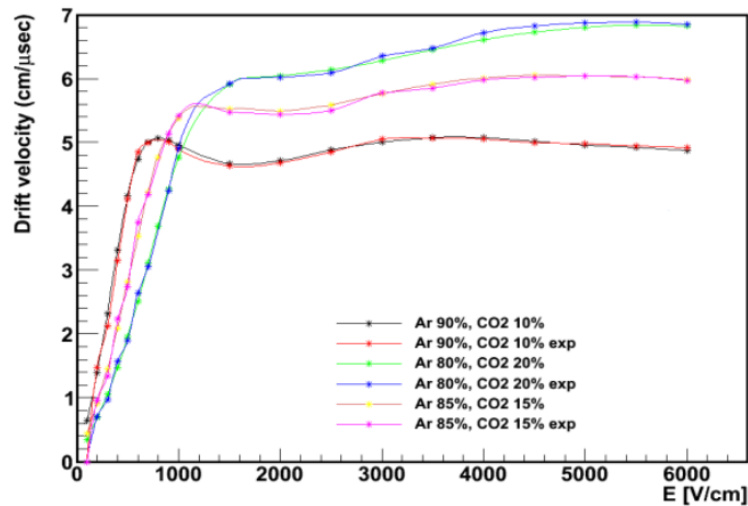


Figure 3.8: The drift velocity of Ar mixtures for different percentages.

endency of the drift velocity on different gases is also given in Graph 3.8. The effect of the gas mixture is more difficult to interpret than that of the transverse diffusion, since it now depends strongly on the fields too.

3.3.2 Charge amplification

In the previous section (see 3.3.1) we looked at electric field strengths which allow transportation and collection of the liberated electrons; different operating regimes of a gas detector have been distinguished. Summing up, three important regions can be found in the multiplication area: the proportional region, the Geiger-Muller region and, the discharge region.

A ionization produced by an electron is a statistical process which depends on the electron energy as well as on the average distance an electron has to travel for such a collision to occur. This average distance is defined as *mean free path*.³ An electron, free

³Mean free path is an average distance over which a moving particle (such as an atom, a molecule, a

to move in a region where a uniform electric field is present, will produce one electron pair after a mean free path α^{-1} . Thus two electrons will start drifting and these will create two electron-ion pairs and like this a chain of multiplication occurs. If n is the number of electrons at a certain position, then the increase in this quantity will be after a distance dx :

$$dn = n \cdot \alpha \cdot dx. \quad (3.15)$$

The first Townsend coefficient α is defined as the inverse of the mean free path and is a strongly-depending function of the reduced electric field E/p with p the pressure. Therefore it will depend severely on the position in a non-uniform electric field. The multiplication factor M can then be derived:

$$M = \frac{n}{n_0} \exp \left(\int_{x_1}^{x_2} \alpha(x) dx \right) \quad (3.16)$$

M can also be called *gain*. Usually this integral is not calculated exactly but only an approximate method is used. Most important is that the strength of the signal remains proportional to the energy of the incoming photon.

At higher fields, the proportionality is gradually lost, because of electric field distortions due to the large space-charge. The positively charged ions move slowly and cause a long dead time because of this. At even higher fields, the proportionality is completely lost and the charge collected per ionizing event is essentially independent of the number of primary ion pairs. At this moment the gas breakdown really needs to be stopped before a new event can be measured. Therefore the electronics need to be adapted or a quencher needs to be added.

At really high fields, secondary processes, like photon emission and the space-charge deformation of the electric field (strong at the front of the avalanche) will lead to streamer formation and a spark breakdown. The Raether limit is the physical limiting value of the multiplication factor or gas gain in an ionization avalanche process (Townsend avalanche):

$$\alpha x \approx 20 \quad (3.17)$$

or $M \approx 10^8$. The statistical distribution of the electron energy usually does not even allow to work at gains higher than 10^6 if one wants to avoid breakdown. Also the gap thickness, between electrodes, has a clear influence. The Raether limit will be met at decreasing values of α as the thickness increases.

3.4 The Gas Electron Multiplier

High-energy physics, as anticipated in the previous chapter, has always had the fundamental objective of building increasingly powerful accelerators as well as more performing detectors. In 1968, Georges Charpak invented the Multiwire Proportional Chamber (MWPC), a gaseous detector outperforming by orders of magnitude the rate capability of contemporary devices. The MWPC hosts a grid of thin and parallel anode wires between

photon) substantially changes its direction or energy (or, in a specific context, other properties), typically as a result of one or more successive collisions with other particles.

two cathode planes. The application of suitable voltages enables the device to collect and amplify, by avalanche multiplication, the tiny ionization clusters released in a gas by ionizing radiation, permitting detection with electronics means. Despite their successful use in particle physics experiments, MWPCs have several limitations, intrinsic in their conception: the creation in the multiplication process of large amounts of positive ions, slowly receding towards the cathodes, causes a modification of the applied electric field, and results in a drop of gain and efficiency. The Micro-Strip Gas Counter (MSGC), introduced by Anton Oed in 1988, seemed to overcome some of the above mentioned limitations. MSGC consist of a set of thin parallel metallic strips laid on an insulating substrate, alternatively connected as anodes and cathodes. MSGCs provide rate capabilities two orders of magnitude higher than MWPCs and a tenfold improvement in the multi-track resolution. However, the device appeared to be rather susceptible to irreversible degradation due to occasional but destructive discharges. Many of the problems encountered with MSGCs are connected to the use of fragile electrodes exposed to the high electric fields needed to achieve the gains, typically around 10^4 , needed for detection of small ionization yields. Under these condition, the occurrence in the gas of rare but highly ionizing events, due for example to neutron or gamma conversions, may lead to the creation of a local charge density exceeding the Raether limit leading to the formation of a streamer, and eventually to a discharge.

Introduced in 1997 by Fabio Sauli, the **Gas Electron Multiplier** (GEM) constitutes a powerful addition to the family of fast radiation detectors; originally developed for particle physics experiments, the device has spawned a large number of developments and applications.

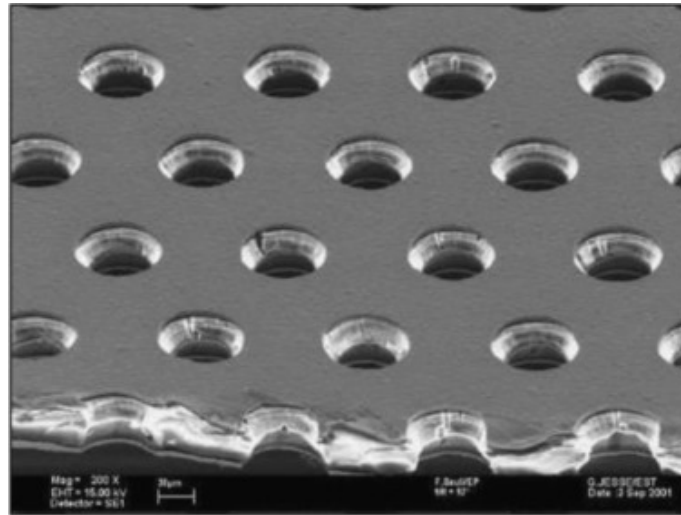


Figure 3.9: Electron microscope picture of a section of typical GEM electrode, $50 \mu\text{m}$ thick. The holes pitch and diameter are 140 and $70 \mu\text{m}$, respectively.

3.4.1 Basic Operating Principle

The Gas Electron Multiplier (GEM) electrode is a thin polymer foil, metal-coated on both sides and characterized of a high density of holes. The holes have, roughly, a diameter of $50\text{-}100 \mu\text{m}$. Typically, the insulating polymer used is Kapton, with a thickness of

50 μm coated on both sides from 5 μm of copper. The holes are initially engraved on the two copper layers with a optical lithography technique⁴; the channels in the Kapton are subsequently opened with the use of a specific solvent, using copper as a mask. Due to the chemical process used which dissolves the polymer on both sides, the holes have a biconical shape with the internal diameter of the insulation slightly lower than the external one on the metal surface. Figure 3.9 shows a picture of a section of typical GEM electrode. Inserted between a drift and a charge collection electrode and with the application of appropriate potentials, the GEM electrode develops near the holes field lines and equipotential as shown in Figure 3.10. The large difference of potential applied between

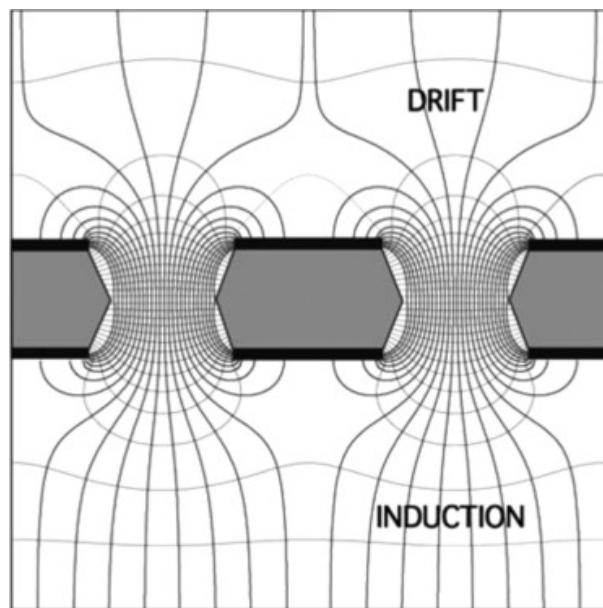


Figure 3.10: Electric field in the region of the holes of a GEM electrode.

the two sides of the foil creates a high field (60-100 kV/cm) in the holes; electrons released in the upper region drift towards the holes and acquire sufficient energy to cause ionizing collisions with the molecules of the gas filling the structure. A sizeable fraction of the electrons produced in the avalanche's front leave the multiplication region and transfer into the lower section of the structure, where they can be collected by an electrode, or injected into a second multiplying region. Figure 3.11 shows schematically a single GEM detector, with a two-dimensional patterned charge detection anode. Unlike other gaseous counters, the (negative) signal on the anode is generated only by the collection of electrons, without a contribution from the slow positive ions, making the device potentially very fast and minimizing space charge problems. Moreover, the low field gap between multiplying and sensing electrodes reduces the probability of the propagation of a discharge to the fragile front-end readout electronics. The equal and opposite charges sensed on the bottom GEM electrode can be used as energy trigger, permitting the detection and localization of events caused by neutral radiation. Replicated in a cascade of GEM foils, the pre-amplification and transfer process permit one to attain very high

⁴Photolithography is a patterning process in which a photosensitive polymer is selectively exposed to light through a mask, leaving a latent image in the polymer that can then be selectively dissolved to provide patterned access to an underlying substrate.

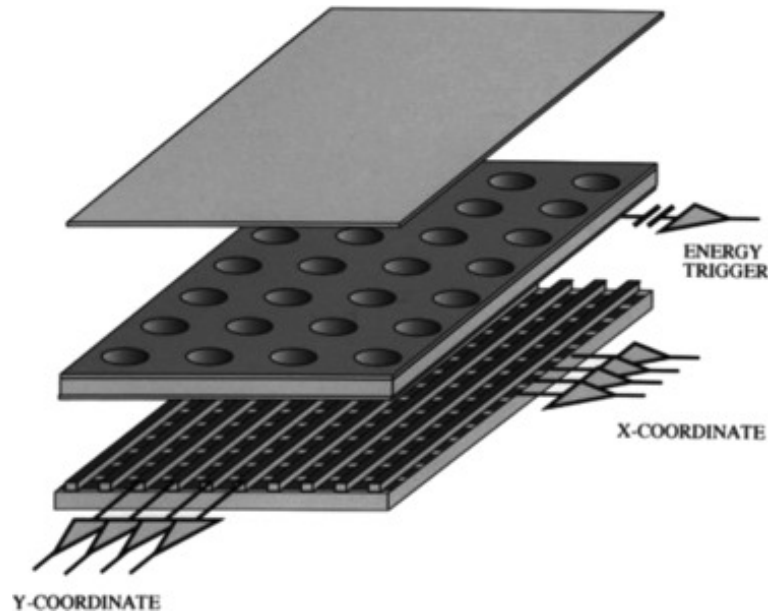


Figure 3.11: Schematics of single GEM detector with Cartesian two-dimensional strip readout.

proportional gains without the occurrence of discharges.

3.4.2 Triple-GEM detector

An unique feature of GEM devices is that, with an appropriate choice of the fields, the fraction of amplified electrons transferring to the gas gap following a first electrode can be injected and multiplied in a second foil, and yet again in a cascade of GEM electrodes. The noticeable advantage of multiple structures is that the overall gain needed for detection can be attained with each of the electrodes operated at much lower voltage, therefore much less prone to discharges. In Figure 3.12 a comparison for gain and discharge probability is given.

A Triple-GEM detector is shown schematically in Figure 3.13. The device has three identical GEM electrodes, a Printed Circuit Board (PCB) anode, a drift cathode. This is the result of thorough optimization studies aimed at realizing detectors with high rate capability and reliability. In general, there are no exclusions on the choice of gas mixtures for operation of any gaseous detector but to detect ionizing particles and radiations noble gases are best candidates due to their shell configuration. Due to the electro-negativity of Carbon-dioxide (CO_2), electrons are attracted and attached to its molecules, therefore it works as a quencher in the gas mixture. A typical choice for gas mixture is given by Argon (70%) and CO_2 (30%).

A standard triple GEM detector prototype has a *drift gap*, two *transfer gaps* (TR1, TR2), and an *induction gap* of 3 mm, 1 mm, 2 mm, and 1 mm respectively. Therefore, a detailed analysis of the aforementioned regions is given in the following:

- The ionization produced in the drift gap, once multiplied by three GEM foils, induces most of the signal. In a region of a few hundred μm from the GEM, the lines of the drift electric field connect to those of the GEM channels, which collect

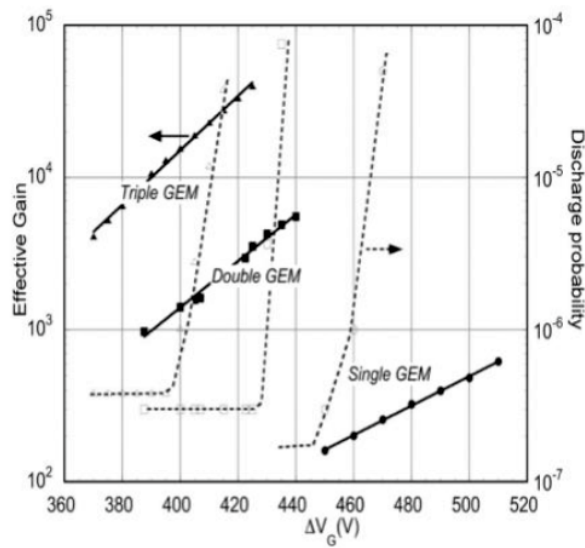


Figure 3.12: Gain and discharge probability as a function of voltage for a single GEM, double GEM and triple GEM detector in Ar – CO₂.

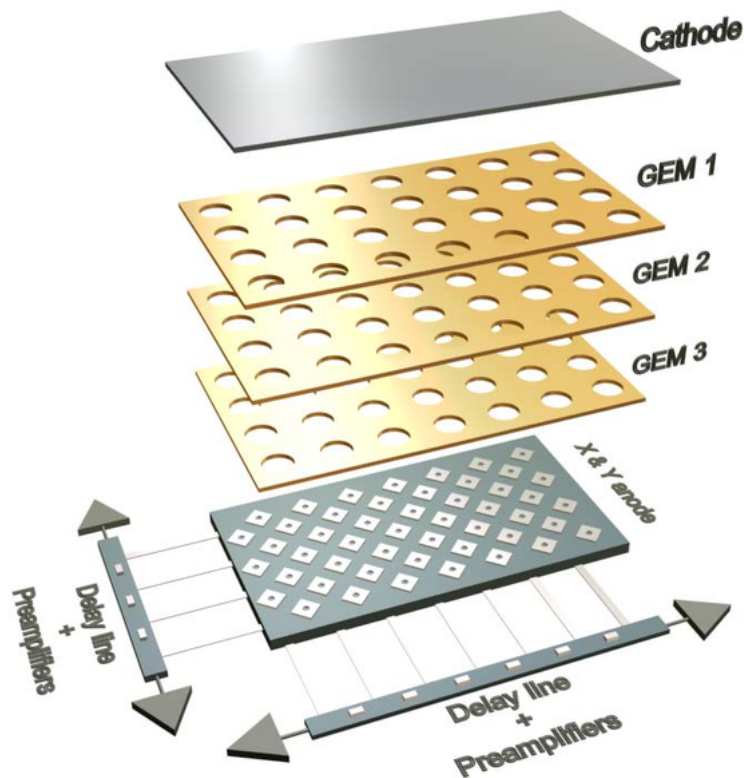


Figure 3.13: Schematics view of a Triple-GEM detector.

the electrons within the holes. The geometry of this region must therefore be carefully chosen and, in the same way, the electric field: a too high field, in fact, would prevent the collecting electrons, causing them to collide with the copper layer.

- In transfer gaps, secondary electrons are extracted from a GEM and transported to the next. Hence, the electric field in the transfer gap (E_T) is an important parameter to optimize charge mobility: a high E_T is necessary to ensure good extraction capacity of the secondary electrons from the upper GEM to the transfer gap; conversely, E_T must be kept low to reduce the defocusing effect and to have a high collection efficiency in the lower GEM.
- In order to maximize the amount of charge collected by the pads, it is necessary increase as much as possible the ability to extract electrons from the third GEM. The induction field E_I must therefore be as high as possible, avoiding however instability of the detector.

3.4.3 Gain of a Triple-GEM detector

Gain is defined as the average number of electrons reaching the anode per primary electron. It is a fundamental parameter of a triple GEM detector and contains information on the electrical and geometric characteristics of the device, as well as on the composition of the gas mixture used. Part of the electrons is sometimes absorbed by the electrodes of the GEM foils: this leads to a decrease in the gain and is the reason why the *intrinsic gain* is distinguished from the *effective gain* of a Triple-GEM detector. The intrinsic gain of a triple GEM detector is characterized by the following relation of proportionality:

$$G_{int} \propto \prod_{k=1}^3 e^{\langle \alpha \rangle \cdot V_k} \propto e^{\langle \alpha \rangle \cdot \sum_{k=1}^3 V_k} \quad (3.18)$$

where V_k is the relative voltage applied on a single GEM foil, $\sum_{k=1}^3 V_k$ is the sum of the voltage differences on each GEM foil, $\langle \alpha \rangle$ is the mean value of the first Townsend coefficient along the electron path in each hole. The *Effective Gain* depends on some main parameters:

- the intrinsic gain;
- the fraction of electrons lost due to recombination with ions or attachment, which depends on the composition of the gas and the electric field between the GEMs;
- the loss of electrons on the electrodes of the GEM foil. This quantity is strongly linked to the electron *collection efficiency* ($\epsilon_k^{collection}$) as well as the *extraction efficiency* ($f_k^{extraction}$). The ratio between the number of electrons entering the holes and electrons lost on copper is called collection efficiency; the ratio between the number of electrons that coming out from the holes and electrons lost on copper is called extraction efficiency.

The effective gain for a Triple-GEM detector, hence, is defined as:

$$G_{eff} \propto G_{int} \cdot \prod_{k=1}^3 \epsilon_k^{collection} \cdot f_k^{extraction} \quad (3.19)$$

It is therefore possible to balance the voltage applied to each GEM for a given gain value. In fact, since the gain depends on the tension differences applied to each GEM foil, it is in principle possible to choose suitably the voltage values to achieve optimal performances however, being careful not to cause permanent damage to the detector due to discharges. In the triple GEM detector, it is possible to increase the voltage applied to the first GEM and decrease that applied to the third GEM; under these conditions, the charge that reaches the third GEM is larger, but the electronic diffusion due to a lower voltage and therefore to a lower field, redistributes the charges over a greater number of holes, reducing the discharge probability.

3.4.4 Timing Resolution

Time resolution of GEM detectors is determined by the spread in signal formation time for different events. Time resolution depends on several factors, the most important being the electron drift velocity. Drift velocity depends on the gas type and the electric field value. For a charged particle, the number of the created ionization clusters follows the Poisson distribution with an average value that depends on the energy of the particle and gas mixture. In particular, for a MIP, the average value essentially depends on the properties of the mixture. Hence, the distance x of the cluster of ionization closest to the first GEM follows a distribution given by

$$P(x) = ne^{-nx} \quad (3.20)$$

where n is the number of ionization clusters per unit length. In the ideal situation, where the first cluster is always revealed, the temporal resolution of the detector will be

$$\sigma(t) = \frac{1}{n \cdot v_{drift}} \quad (3.21)$$

The other clusters of ionization have a probability distribution with $\sigma(x)$ greater than first cluster, but still proportional to $1/n$. Therefore, in order to optimize the time performance of the detector, a mixture is required that favors high drift speed and high clustering.

3.5 Common features of CMS Triple-GEM detector systems

The GE1/1 chambers installed for the Muon System upgrade of CMS consist of Triple-GEM with trapezoidal structure placed between a drift and a reading electrode and filled with gas, as shown in 3.14.

The Triple-GEM structure allows to reach a multiplication factor of $\sim 10^5$ with modest voltages, since the total gain is given by the product of the gain of each foil. The amplified charge induces a signal on the electrodes which are segmented into 384 strips in the direction of muon curvature ϕ to allow the detector to be position sensitive. Furthermore, the chambers are divided into 3 parts along ϕ and 8 along η , identifying 24 sectors, each having 128 strips. Inside GE1/1, a pair of triple GEM chambers of this type are overlapping for form a ‘superchamber’. Each ‘superchamber’ providing redundancy,

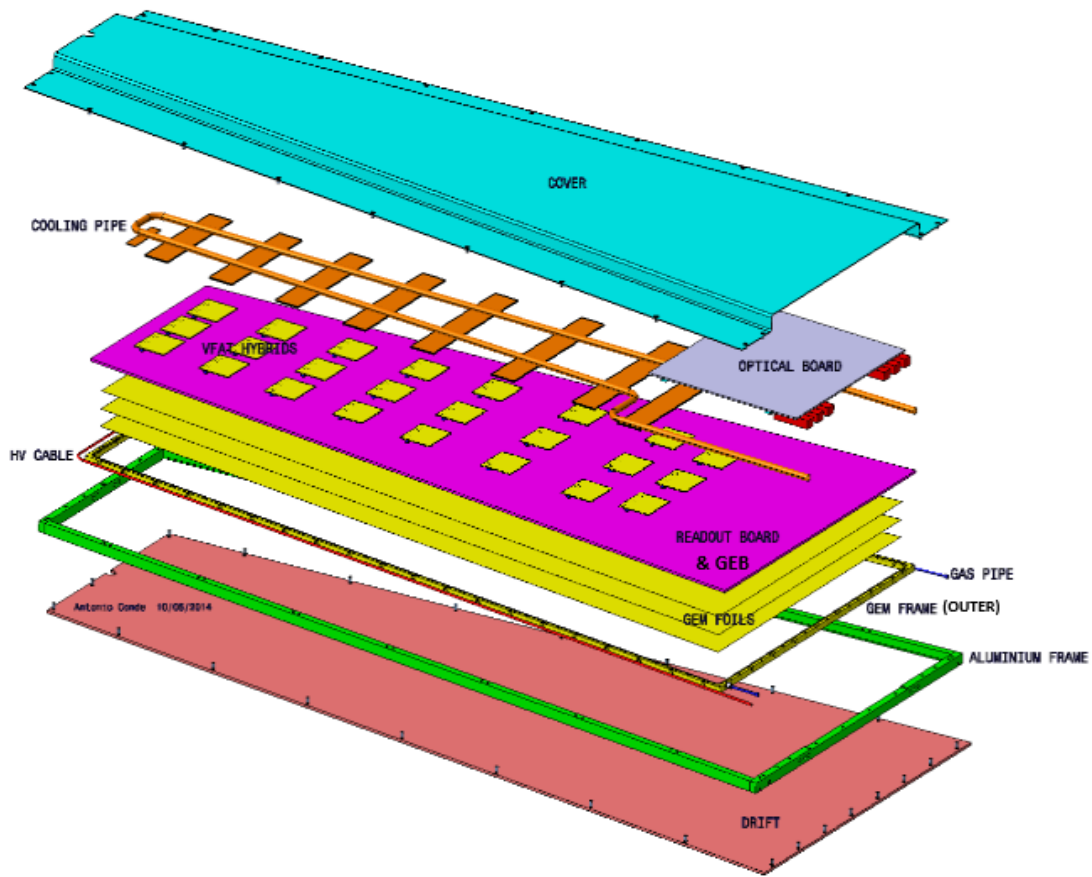


Figure 3.14: Exploded view of the mechanical design of a single CMS triple-GEM module.

enhanced triggering and reconstruction capabilities and cover slightly more than 10° in GE1/1. For both endcaps, 72 superchambers will be needed for GE1/1. The two readout planes of the superchambers are separated by 20 mm in z , and the total thickness is 88 mm. The GE1/1 superchambers alternate in ϕ between long and short versions: the long ones cover an η range of 1.5-2.18 while the short ones cover an η range of 1.6-2.18. The location of these chambers is shown in Figure 3.15. The assembly and sealing of the detector are entirely mechanical. No glue is applied during assembly, which makes it possible to open a detector again for repairs if needed. It also speeds up the assembly of the module since there are no wait times due to curing of glue. The drift board features a single drift cathode on its inner side and a solid ground plane on the outside of the module for RF shielding purposes. It provides connections to external high voltage supply lines via HV noise filtering circuitry. The drift board routes a total of seven different potentials to the various GEM electrodes and to the drift cathode.

3.5.1 Readout Methods

The reading electrode of Triple-GEM detectors contains 3072 strips organized in groups of 128 channels connected to 128 pin connectors distributed over the 8 sectors of the chamber. The chambers have also 8 segments in η direction, for a total of 24 indepen-

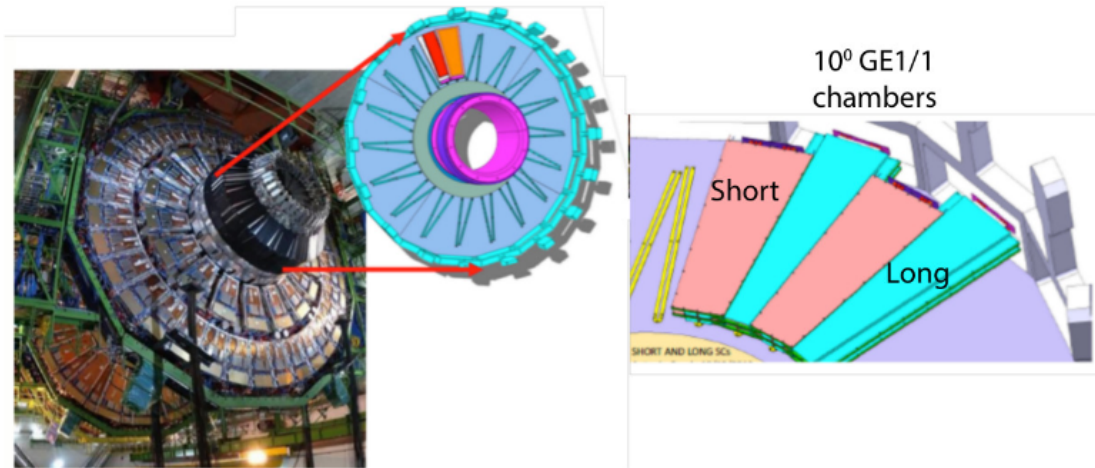


Figure 3.15: Location of the GE1/1 detectors (left) and detailed view of the overlapping of GE1/1 superchambers (right).

dent segments. A total of 24 128-channel front-end chips, called Very Forward ATLAS TOTEM chips or simply VFAT3, are hence needed for the read-out of a single GEM chamber. The VFAT3 architecture, reported in Figure 3.16, is composed of 128 channels, each comprising a charge sensitive preamplifier and shaper. This is followed by a constant fraction discriminator per channel. Following the discriminator is a synchronisation unit which synchronises the comparator result with the 40 MHz clock of LHC. The data then splits into two paths, one with a fixed latency for trigger signals, and the second for tracking data which is non-synchronous. All communication with VFAT3 occurs through the E-port. This includes synchronisation to the LHC clock, slow control commands as well as fast trigger commands, data packets, calibration and monitoring. The chip is highly programmable to offer maximum flexibility. The data from the VFAT3 chips are sent to

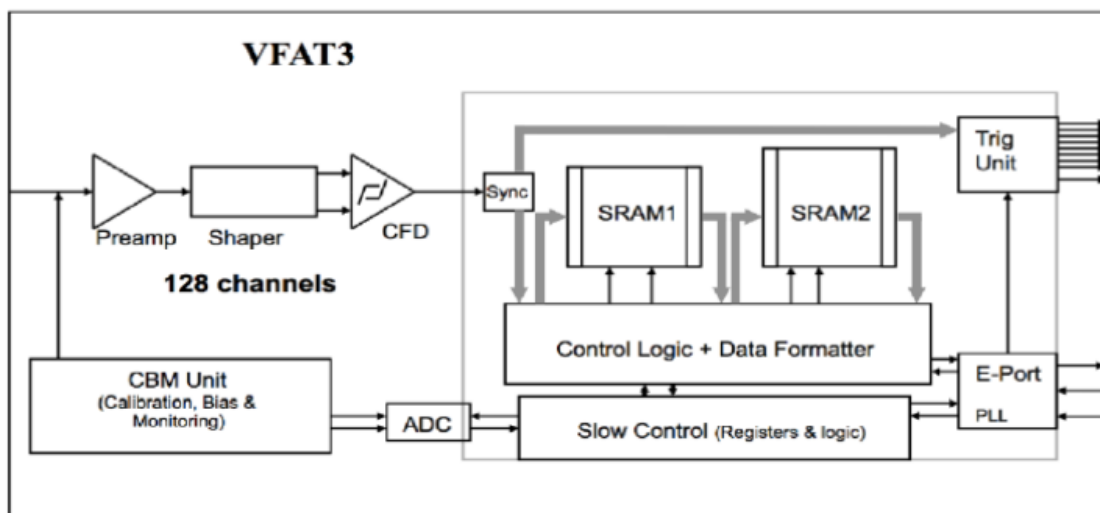


Figure 3.16: Block diagram of reading ASIC of the front-end VFAT3.

the GEM Electronics Board (GEB) which delivers power and communication signals to and from the VFAT3 as well as providing the connection to the GEM strips. From the

GEB, data are transmitted to one FPGA board, called the GEM OptoHybrid (OH), located on the wide end of the GEM chamber. One of the main components of the OH is a Xilinx Virtex 6 FPGA, which has been shown to be radiation-hard to levels at least two orders of magnitude higher than the expected radiation dosage. The system is designed such that one optical fibre can read out the tracking data from one GEM column, while all trigger data are carried out by a dedicated additional fibre. A single GEM chamber has three optical fibres to take the tracking and trigger data to and from the CMSGEM DAQ system. For the off-detector electronics, the μ TCA standard and the CMS MP7 and AMC13 μ TCA boards are used. Data are transmitted between the on- and off-detector electronics through optical fibers using the CERN GigaBit Transceiver (GBT) protocol.

3.5.2 Pulse Formation and Shape

The GEM signal on the detector readout depends exclusively on the motion of the electrons in the induction region. Taking on a field constant electric, the signal induced on a pad by an electron that drift in the induction gap for a time $t_{drift} = g_i/v_{drift}$, it is a pulse in current of intensity $I = e/t_{drift}$ and duration t_{drift} , where g_i represents the size of the induction gap. The total signal induced on a pad by a track that crosses the GEM, is given by the sum of the signals due to the individual ionization electrons, amplified by the multiplication that occurs through the planes of the GEM. Each e^- is delayed by the corresponding drift time t_{drift} in the drift gap. The total signal must be convolved with the response of an amplifier to obtain the input signal to a discriminator. The time of the event is given from the moment in which the rising edge of the signal exceeds the discriminator threshold. The rising edge of the signal to the amplifier has a profile step; each step corresponds to the signal of an ionization cluster. Consequently, the temporal resolution will be determined by the temporal distribution of the first ionization clusters and their respective ones fluctuations in the amplitude of the signal, both in the ionization process and during multiplication through the GEM.

3.5.3 Physics performances

The performances of the different generations of GE1/1 prototypes were studied in a series of beam tests at CERN and Fermilab [8]. The main features the GE1/1 system are high efficiency, good time resolution, high rate capability, and low discharge probability. During the R&D of the final detector, two gas mixtures were considered in proportions Ar/CO₂/CF₄ 45:15:40 and Ar/CO₂ 70:30. Different tests have been performed to choose the best between the two gas mixtures and the latter has been chosen as the candidate for the final setup.

Efficiency

Efficiency, which represents the probability to record a signal when a particle crosses the detector, is estimated by recording the total number of triggers N generated by the coincidence of the three scintillators and the number of hits N_1 , generated by a test region. However, due to possible misalignment of the test region and particle scattering, the number of hits N_2 are also observed from neighboring regions. Therefore, the efficiency is calculated by removing these additional hits from the total number of triggers using the

formula $\epsilon = N_1/(N - N_1)$. The results for both the gas mixtures are reported in Figure 3.17.

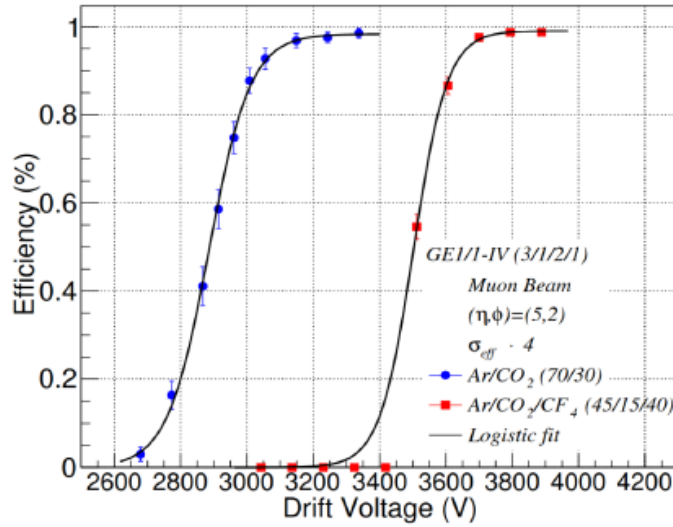


Figure 3.17: Efficiency of a GE1/1 detector for the gas compositions Ar/CO₂ 70:30 and Ar/CO₂/CF₄ 45:15:40. Points represent the data and solid lines represent parametric fits. The error bars on data represent Gaussian one sigma uncertainty. The drift bias to reach the efficiency plateau is lower for the gas mixture without CF₄ due to the quenching effect of CF₄

Time resolution

The time resolution [9] is another important feature of any detector. This parameter is dependent mainly by the drift velocity due to unavoidable fluctuations in the position of the primary ionization cluster formed in the drift region, as shown in Section 3.4.4. The time resolution is measured as the standard deviation of the distribution of the time intervals that occur between the trigger and the detector signal, measured by a time to digital converter (TDC). Figure 3.18 reports the results of the time resolution as a function of the drift voltage [10].

Rate capability

The rate capability gives a measure of the maximum flux of incoming particles that can be detected by the chamber before it is completely saturated by the secondary ionisation charges [11]. The flux in the CMS endcaps is not expected to exceed 10 kHz/cm² and the nominal operating gain of a GE1/1 detector is expected to be $\sim 7 \times 10^3$. Using an intense source of X-ray photons, the rate capability is assessed by measuring the gain as a function of rate R:

$$G = \frac{I}{R \cdot \eta_T \cdot e} \quad (3.22)$$

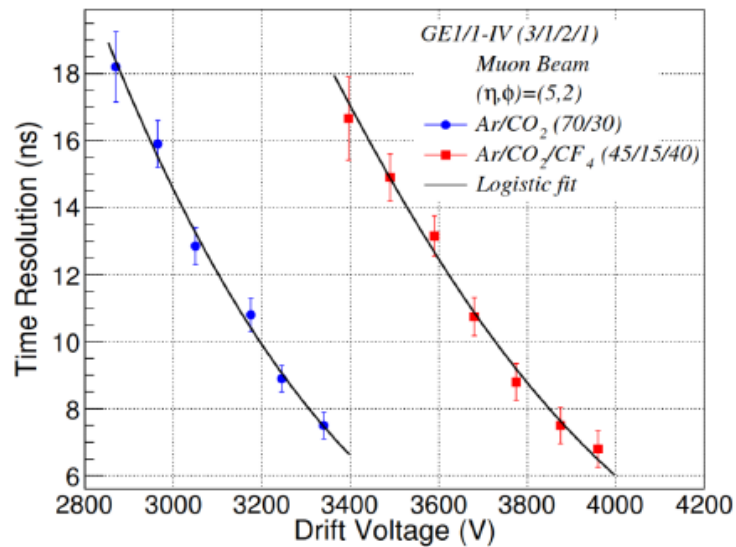


Figure 3.18: Time Resolution of a GE1/1 detector for the gas compositions Ar/CO₂ 70:30 and Ar/CO₂/CF₄ 45:15:40. Points represent the data and solid lines represent parametric fits. The error bars on data represent Gaussian one sigma uncertainty.

where e is the elementary charge and η_T depends on the energy released by the incident particle and on the gas mixture. The amplified current is measured using a pico-ammeter⁵ connected to the anode of the detector as the incident particle flux is varied using copper attenuators. The measurements show that the effective gain of a full-size GE1/1-IV

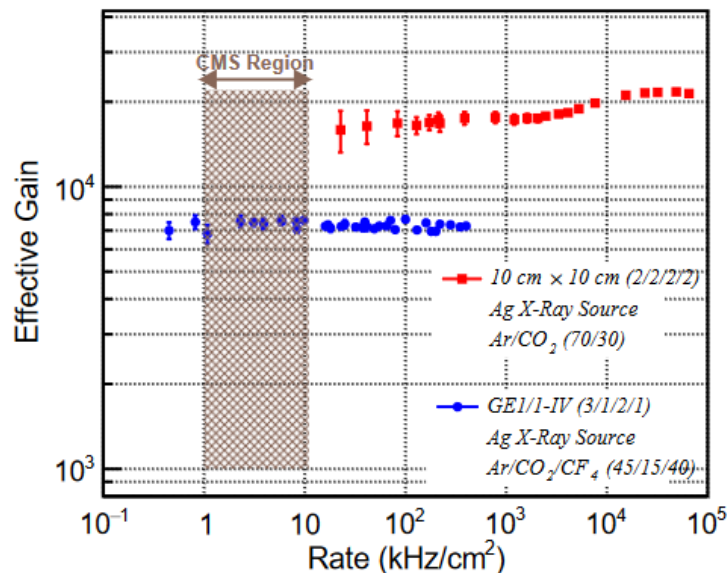


Figure 3.19: Rate capabilities of a GE1/1-IV chamber. The shaded **CMS Region** spans the range of particle flux expected in CMS for HL-LHC.

detector remains stable up to several hundreds of kHz/cm, as shown in Figure 3.19.

⁵see Chapter 4

Discharge Probability

The GE1/1 detectors will operate at sufficiently high gain to ensure maximum detection efficiency while maintaining timing performance. However, with high gains, intense particle fluxes, and densely ionizing particles, the probability increases for producing discharges that could damage the detectors. Discharges are initiated when local charge exceeds the Raether limit resulting in variations in the local electric field, as shown in Section 3.3.2. Several features of the chamber design reduce the probability of a discharge and limit the damage from those that occur: the asymmetric distribution of charge-amplifying electric fields over the three GEM foils, sectorization of the GEM foils, and use of protection resistors to limit the available energy in case of a discharge. The three amplification stages of a GE1/1 chamber are set to slightly different gains by applying different voltages across the foils. The voltage across the first GEM foil is 3% higher than the second GEM foil, which itself is 5% higher than the third foil. The measured dis-

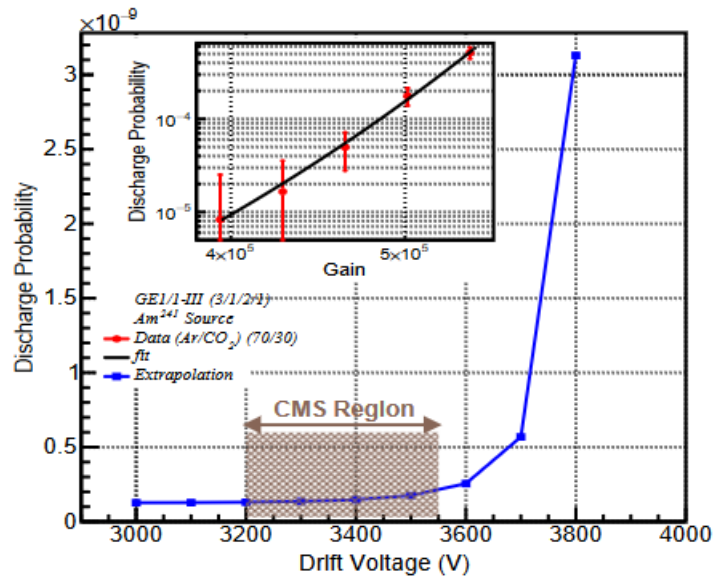


Figure 3.20: Discharge probability for the gas composition Ar/CO₂

charge probability versus gain for a GE1/1-III detector is shown in Figure 3.20. The data are also displayed as discharge probability versus drift potential, with the **CMS Region** indicated.

Chapter 4

PICO: a high voltage seven independent channel pico-ammeter

Introduction

The Triple-GEM detectors deployed in the phase I upgrade of the CMS Muon System constitute a novel state-of-the-art technology that will require careful commissioning and dedicated studies. A precise monitoring of the currents through the three GEM foils in particular would allow an in-depth understanding of the gain of the chamber, and potentially allow to diagnose issues like electric discharges that might cause the chamber to malfunction. A suitable tool for carrying out such measurements is the multi-channel pico-ammeter, named PICO, developed by the INFN whose design perfectly fits this task. In this section we want to describe PICO and its features and explain the procedure implemented to determine its the resolution. We will see that current and voltage measurements are slightly correlated to the temperature variation of the ADCs present in PICO. Over the course of these studies, corrective factors have been derived as well as the voltage and current resolution of the device.

4.1 Description of the device

The device is a high voltage voltmeter/pico-ammeter made of 7 independent channels and it is able to perform non-destructive measurements of voltage and current. PICO has been completely designed, assembled and tested at INFN Napoli. As mentioned before, its original purpose was to act as current and discharge monitor of GEM detector for the CMS experiment, however its design allows it to work as a general purpose device, with a wide range of possible applications. For example, it can serve as a gas detector charge spectrum measurement device or TPC electrodes current monitor device.

The maximum current readout rate is about 480 Hz to be compared with the 1-2 Hz rate provided by the standard high-voltage power supply used in CMS [12]. Hence, PICO is able to monitor with high sampling speed voltage and current independently on each of the 7 channels. Each channel works up to 5 kV. The system is built in a way to allow for upgrades to the readout rate and improving this feature in case necessary for the application at hand. The block diagram of PICO is shown in Figure 4.1, and is composed

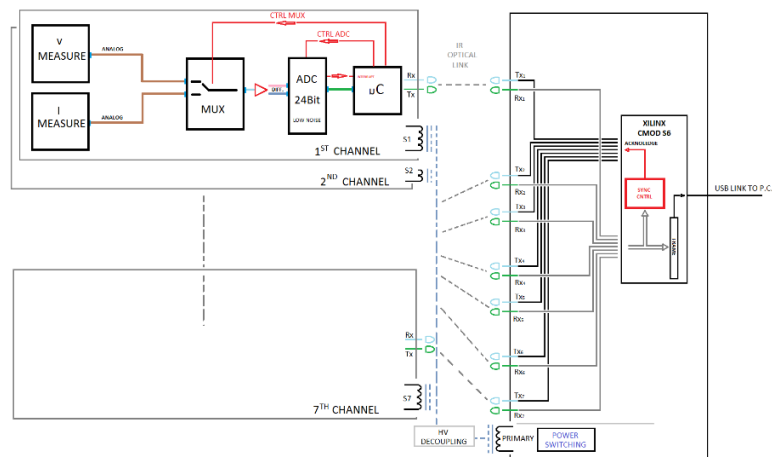


Figure 4.1: Block diagram of the PICO device. From left to right: the HV measurement block, the power switching and HV decoupling block, the collector block.

of three parts, housed on a common motherboard:

- the front-end/HV measurement block;
- the power switching and HV decoupling block;
- the collector block;

Each HV measurement board is equipped with a 24-bits ADC, a multiplexer (MUX) and a micro-Controller (μ C) Arduino. The HV measurement blocks send data to the collector block. Those two blocks are opto-coupled, through an infra-red transfer system (IRDA), in order to keep the high-voltage separated (HV measurement board reference ground) to the readout. The collector block is consist of a Spartan6 Xilinx FPGA and it commands the 7 Arduino (μ C)s installed on the HV measurement boards, it receives data from the measurement channels through a bus, it manages the data and it sends them to the PC, via a USB port. The power switching and HV decoupling block provides the floating supply voltage with high galvanic isolation to the HV measurement block, through two custom-made transformers made by using cables with HV isolation. In Figure 4.2 a CAD drawing of the motherboard is shown and that also hosts:

- the bus lines for the T_x - R_x communication between the FPGA and the Arduinos;
- a voltage regulator that generate the 5V needed to power the infrared equipment on the FPGA side;
- the switching drivers (LT3999) of the transformers that don't need a feedback net.

4.1.1 The internal and external structure of PICO

The Figure 4.4 shows an image of the device and its internal structure. The box, with dimensions $50 \times 20 \times 15$ cm, is equipped with a HV Amphenol male input connector (9 pin) and a HV Amphenol female connector (9 pin) as a output, to perform non-destructive

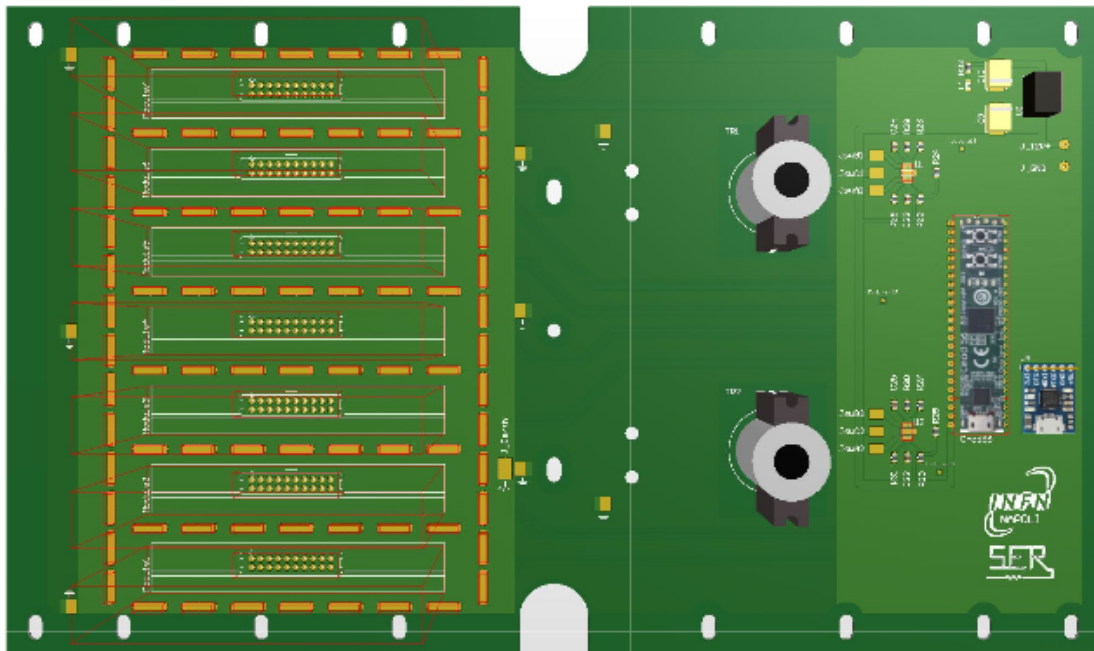


Figure 4.2: CAD drawings of the motherboard. On the left are hosted the XX pin connectors of the 7 HV measurement channels, in the middle are visible the 2 supports of the transformers, and on the right is shown the FPGA connector and the USB port's card.

current and voltage measurements. The measurements of input HV and current, through PICO, are carried out to power the detector under test.

In Figure 4.5 a picture of the front panel of PICO is shown. It hosts:

- a connector for the 12 V power supply,
- the power switch,
- the switch ON LED indicator,
- the USB port that provide the connection to the PC (UART),
- a terminal (*Shield*) connected to the HV cable Shield,
- the PICO's GND reference terminal.

4.2 Characterization of PICO

In order to perform precise current measurements, suitable for optimizing the electric fields of the Triple-GEM detector presented in Chapter 5, it was necessary to fully characterize the pico-ammeter.

In this section the device characterization procedure is described. Data acquisition involves the connection of PICO to the PC through a USB cable, where data can be read directly by using a custom-developed LabView software, that performs the task to convert



Figure 4.3: Picture of the device.



Figure 4.4: View of the internal structure of PICO.



Figure 4.5: Front panel of PICO.

the information to a text file. The digital output of PICO is therefore recorded on a file that contains for each entry, 7 current and 7 voltage values, i.e. one for each channel of the device and the timestamp. The LabView software enables us also to set the *downsample* factor, which regulates the fraction of data to be registered. By setting a downsample equal to 1 all data taken are recorded on the file.

In Figure 4.6 the control panel of the LabView software used for the acquisition is shown. In the upper part are visible the commands for enabling the connection to PICO, starting the data acquisition, and choosing the filename. In the upper right part indicators are positioned displaying the DAQ information, like DAQ rate, events loss, etc. In the middle is shown the graph containing the 7 voltage channels as a function of time, while in the bottom is shown the graph for the current channels.

In the following, the channels of the pico-ammeter will be referred to as 'CH'. Once PICO is connected to a GEM detector, each channel will correspond to one of 7 GEM electrodes.

PICO does also monitor the temperature of its internal ADCs. Once per every one

hundred recorded entries, PICO does register a temperature value instead of the voltage by using an ad hoc numbering convention.

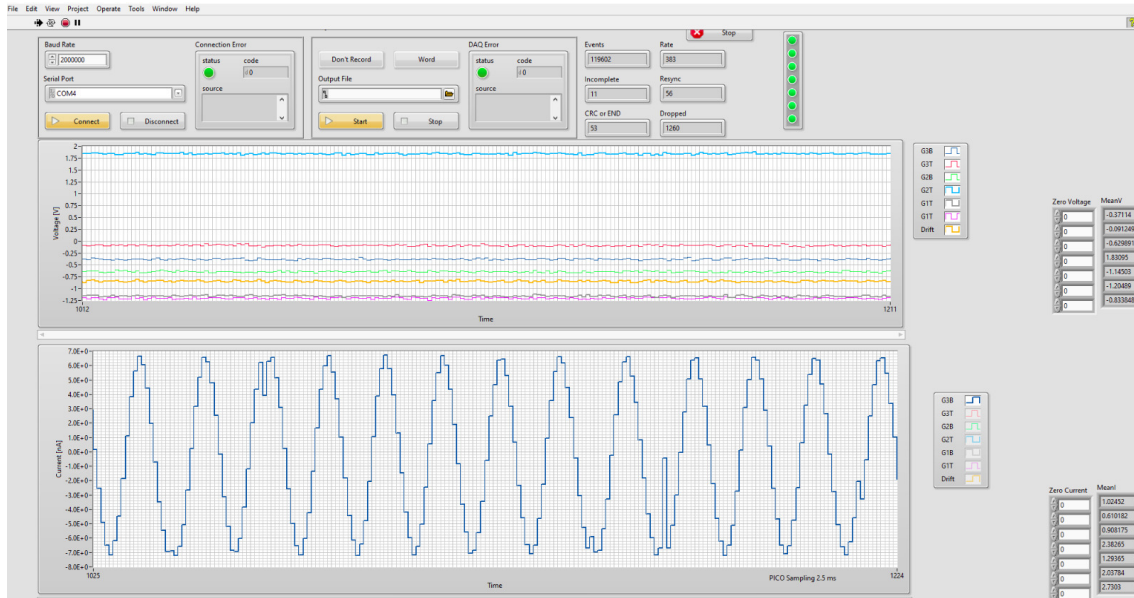


Figure 4.6: Control Panel of the LabView software: on the top the section used to start data acquisition and recording. In the upper right part indicators are positioned displaying the DAQ information, like DAQ rate, events loss, etc. In the middle is shown the graph containing the 7 voltage channels as a function of time, while in the bottom is shown the graph for the current channels.

At first, a study of thermal dependence of the output of the device over time was performed. The current and voltage measurements do carry a dependence on the variations in temperature undergone by the device, therefore it is necessary to keep track of the temperature variation for an a posteriori correction. The variation of the temperature over time was first monitored with the following setup:

- PICO switched ON and disconnected to A1515 (HV = 0),
- acquisition time: 72 h,
- downsample: 1.

The conversion formula from Arbitrary Units [AU] to °C is:

$$T(^{\circ}\text{C}) = \frac{x \cdot 3.3V}{1.024} - 500 \quad (4.1)$$

In Figure 4.7 the variation of the temperature over time for CH1 of PICO is shown. The horizontal axis corresponds to a time interval of data taking of 38 hours. At time

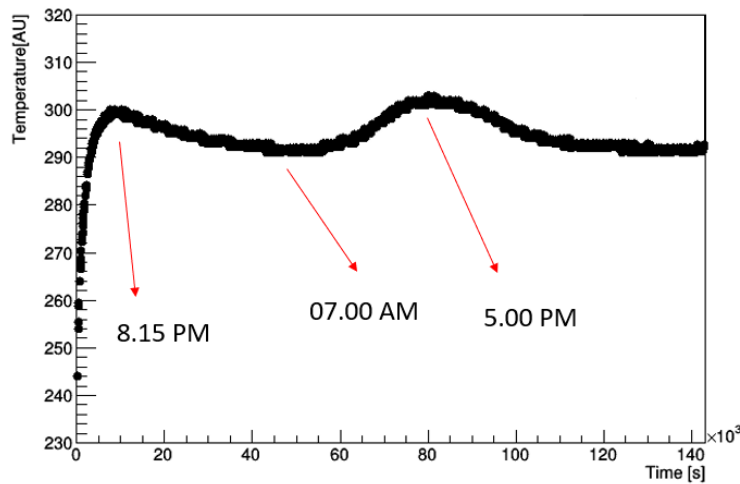


Figure 4.7: Temperature variation over time for CH1 of PICO: a steep increase in temperature is visible with a consequent fluctuating trend corresponding to the day-night cycle, as highlighted by the specific times indicated on the plot. The horizontal axis corresponds to a time interval of 38 h. On the vertical axis the temperature is expressed in AU: from the initial value registered at time of switching ON, the temperature gap has risen by about 20 °C i.e. from 28.6 °C to 48 °C (see Equation 4.1).

0 (6.15 PM) the device has been switched ON. As expected, in the first 2 hours (up to 8.15 PM) after the switch ON, a steep increase in temperature (about 20 °C) occurred. Later, the temperature results more stable and it fluctuates in a range of 3-4 °C. This fluctuation is mostly due to the change of the temperature in the laboratory building (day/night effect). From the initial value registered at time of switching ON, the temperature gap has risen by about 20 °C i.e. from 28.6 °C to 48 °C (see the Equation 4.1). A similar trend in temperature was observed for all channels of the pico-ammeter, as is depicted in Figure 4.8.

At the same time, we performed a study, for each channel of PICO, of the stability as a function of time of the output current and voltage for a null input. Figure 4.9 shows the output of current and voltage, respectively on the left and on the right, as a function of time. Those plots can be compared with the Figure 4.7. A decrease in the current and voltage output can be observed in correspondence with an increase of temperature. In particular, from the left plot we can see that the maximum variation in temperature of $\approx 20^\circ$ corresponds to a current variation of about 1 nA in Figure 4.9 (left) and of 0.3 V in Figure 4.9 (right). It is very important to highlight that after the steep thermal variation due to the switching ON of PICO, the output voltage (current) fluctuates only of about 0.1 V (0.25 nA). Although the output of PICO seems to retain its dependence on the thermal variation, the temperature variations become less pronounced. This effect will be studied in detail in the following sections, and appropriate corrections to the output current and voltage will be derived to take into account this residual dependence.

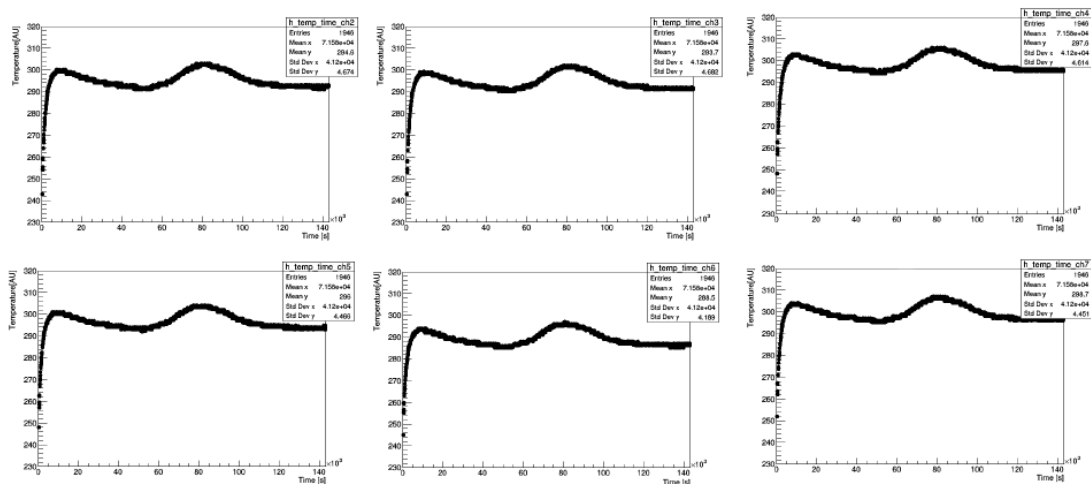


Figure 4.8: Temperature variation over time for the channels of PICO from CH2 to CH7: a steep increase in temperature is visible with a consequent fluctuating trend corresponding to the day-night cycle. The horizontal axis corresponds to a time interval of 38 h. On the vertical axis the temperature is expressed in AU: from the initial value registered at time of switching ON, the temperature gap has risen by about 20 °C i.e. from 28.6 °C to 48 °C (see Equation 4.1).

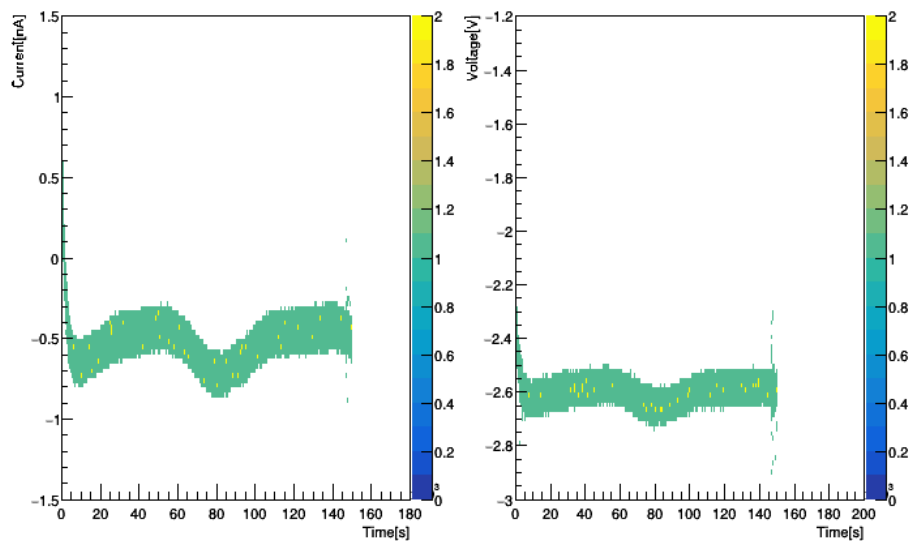


Figure 4.9: On the horizontal axis there is a time interval of 50 hours for both plots. On the left the output of current for null input as a function of time for CH1 of PICO: a variation of about 1 nA is observed in a temperature range of about 20 °C. On the right the output voltage for null input as a function of time for CH1 of PICO: a variation of about 0.3 V in the same temperature range.

4.2.1 Electronic noise of PICO

During the deployment phase of PICO, particular care was needed to reduce the possible sources of electronic noise by working on the ground connections. In Figure 4.10 is shown

the distribution of the output current (for CH1) for null input for a data taking of about 80 h. The double peak structure implies a sinusoidal noise detected by the device. From Figure 4.6 we measured that its frequency was about 50 Hz. Eventually, this issue was solved with a better grounding of the experimental setup and by using a copper foil shield around the pico-ammeter.

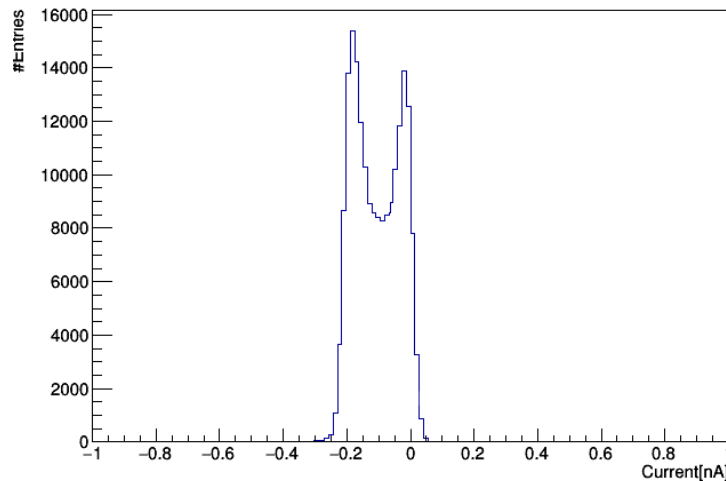


Figure 4.10: Distribution of the output current, for CH1 of PICO, for null input for a data taking of about 80 h. The double peak structure comes from a sinusoidal noise (50 Hz frequency) detected by the device. This sinusoidal noise is evident in Figure 4.6 which in the panel below shows the current output at null input. This issue was solved with a better grounding of the experimental setup and by using a copper foil shield around the pico-ammeter.

4.2.2 Evaluation of the resolution and of the thermal dependence of the output current

Once the 50 Hz noise issue was solved, we started the data taking campaign to model the dependence of the output current from the temperature. The data taking was performed in the following conditions:

- PICO ON from 24 h, disconnected from the A1515 (HV = 0) board and shielded by using a copper foil,
- acquisition time: 2 h,
- downsample: 1.

At first, the distribution of the current values recorded by the pico-ammeter during the 2 hours of data taking was observed for all channels of the device. Instead of finding a Gaussian shape distribution, as expected in the case of a distribution of white noise, we have found, for the CH1, the histograms shown in Figure 4.11. The shape of the

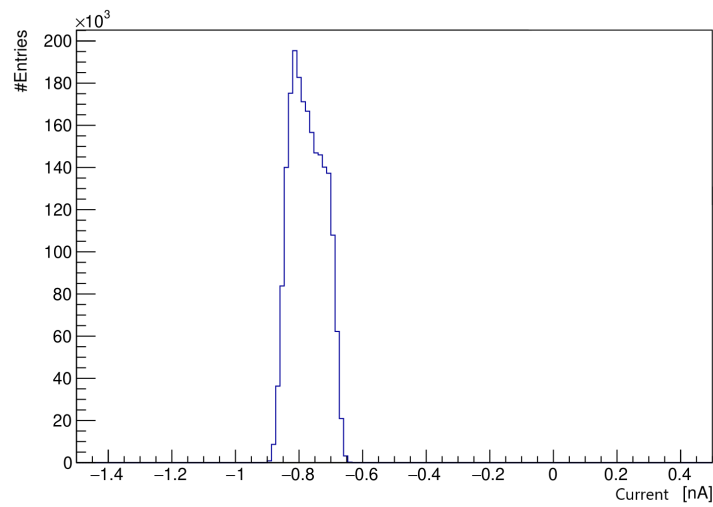


Figure 4.11: Distribution of the output current for null input, expressed in nA, recorded by the CH1 of the pico-ammeter during the 2 hours of data taking for null input: the values have a non-Gaussian shape due to thermal variation.

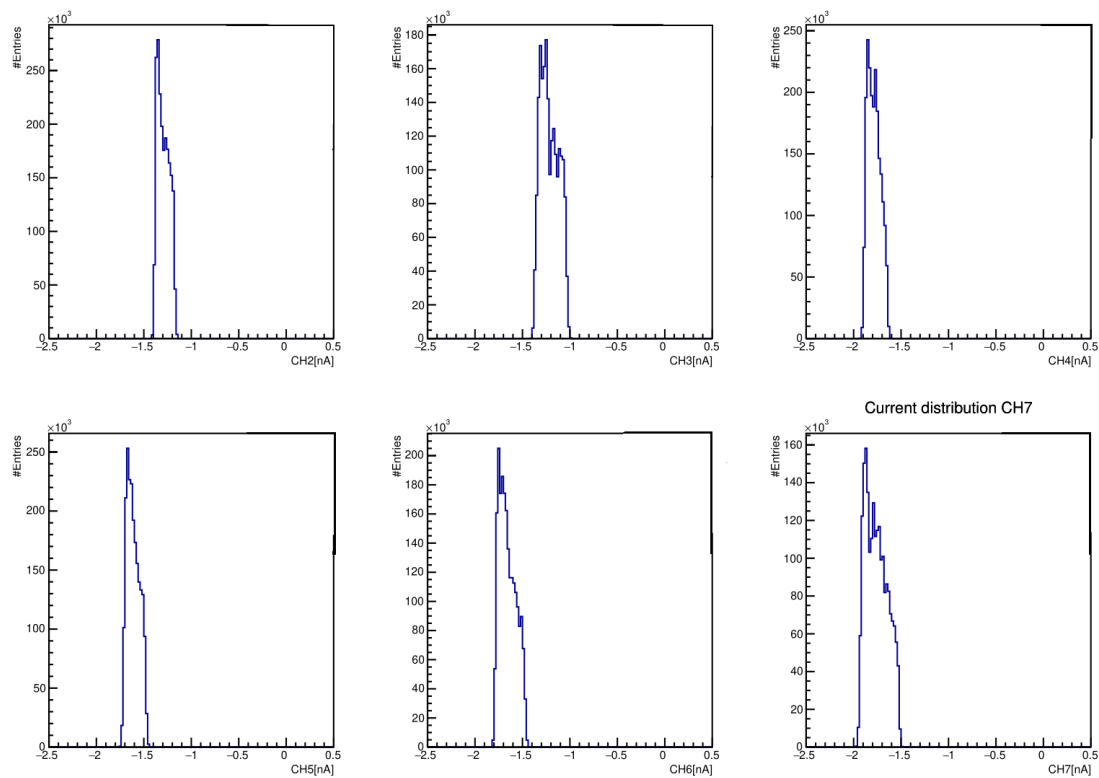


Figure 4.12: Distribution of the output of current for null input, expressed in nA, recorded by the other channels from CH2 to CH7 of the pico-ammeter during the 2 hours of data taking: the values have a non-Gaussian shape due to thermal variation.

distribution was found to be very similar for all the output channels (see Figure 4.12).

This non-Gaussian shape is due to the thermal variation dependence.

To derive an appropriate parametrisation for the correction, in order to avoid introducing systematic effects and correctly evaluate the resolution, the output current as a function of the temperature was observed, as shown in Figure 4.13: this trend was reconstructed only for the points for which the temperature is known. In the Figure 4.14 there is the same trend constructed so that each point corresponds to the average value of the current values contained within each bin present in Figure 4.13. The uncertainty was instead deduced from the RMS of the distributions. A linear dependence was assumed and a χ^2 fit was performed: this procedure was carried out for each channel of the pico-ammeter. The value of the correction factor was obtained by multiplying the intercept of the fit line by the value of the temperature to which the value of the slope of the fit line was added.

The parameter $p_1 = -0.029 \pm 0.003 \text{ nA/[AU]}$ expresses the current variation in correspondence with a temperature variation of 1 AU, which correspond to a variation of $0.3 \text{ }^\circ\text{C}$. Consequently, this factor has been subtracted from each current value recorded by PICO. The current correction procedure was performed for each channel of the device. The value of the last temperature reading by PICO was associated with the points corresponding to unknown temperatures.

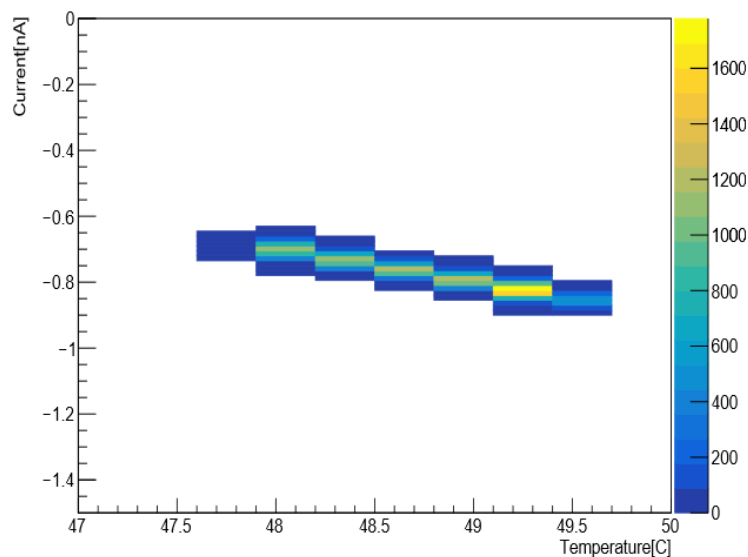


Figure 4.13: The output current at null input as a function of temperature for points for which the temperature is known. The horizontal axis corresponds to a temperature range from $47 \text{ }^\circ\text{C}$ to $50 \text{ }^\circ\text{C}$. The output current has an offset of about 0.6 nA .

The fit parameters used for the correction are evaluated in the temperature range from $47.5 \text{ }^\circ\text{C}$ to $49.5 \text{ }^\circ\text{C}$; the correction therefore was also applied to data acquired in a different temperature range, to assess the validity of the linear model by extrapolating outside the fit range. Figure 4.15 is a proof, for the CH1, of the validity of the correction: the *zero adjustment* is correctly reproduced through the evaluated fit parameters in the temperature range from $32 \text{ }^\circ\text{C}$ to $48 \text{ }^\circ\text{C}$.

In Figure 4.16 it is possible to observe the distribution of the output current following the temperature correction for CH1 of PICO. A Gaussian shape distribution is present as expected in the case of a distribution of white noise. From the fit parameters we evaluate

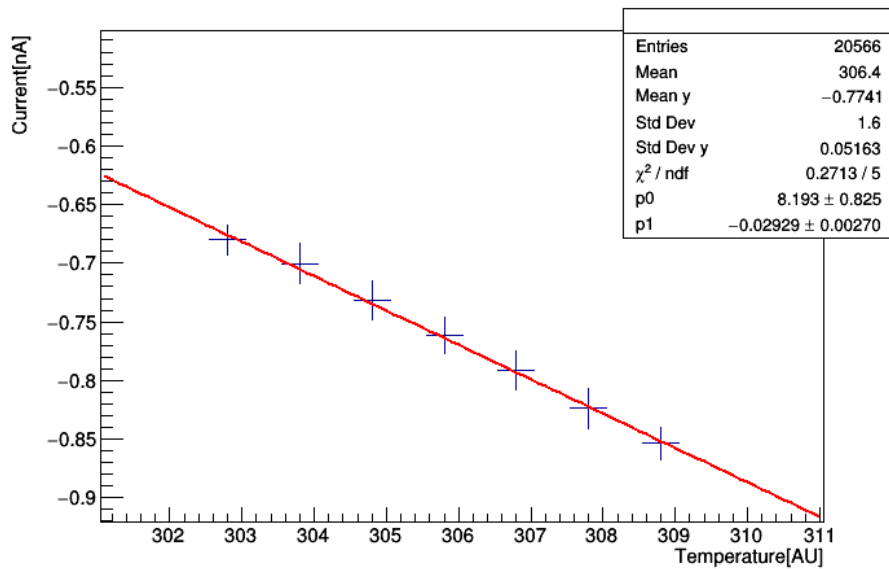


Figure 4.14: The output current as function of temperature: the fit parameters were used to obtain the corrective factor for the current values. The parameter $p_1 = -0.029 \text{ nA}/[\text{AU}]$ expresses the current variation in correspondence with a temperature variation of 1 AU which correspond to a variation of $0.3 \text{ }^\circ\text{C}$. This corresponds to a current variation of about 0.1 nA per unit $^\circ\text{C}$.

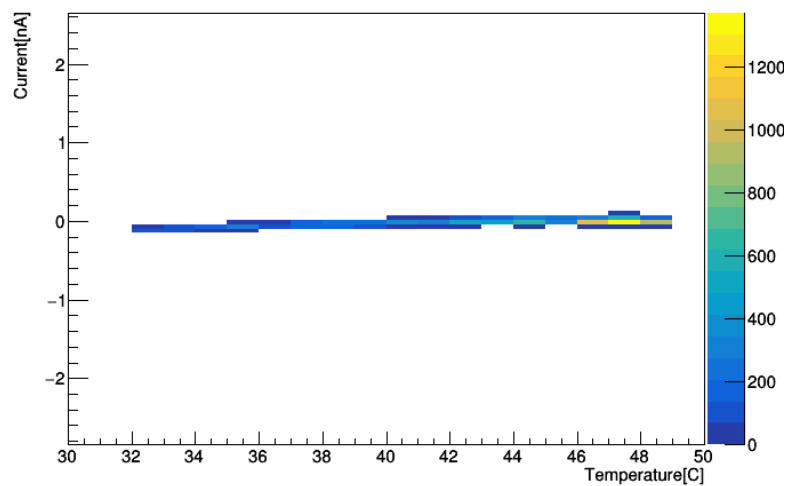


Figure 4.15: Current behavior after the correction for the temperature range from $32 \text{ }^\circ\text{C}$ to $48 \text{ }^\circ\text{C}$ for CH1 of PICO. The *zero adjustment* is satisfactory.

the resolution of the output current for CH1 of PICO, that results to be equal to $16.3 \pm 0.1 \text{ pA}$.

Eventually, the resolution for all channels of PICO is evaluated by fitting (with a Gauss function) all the distributions shown in Figure 4.17, 4.18, 4.19, 4.20, 4.21, 4.22 after the thermal correction. Results are reported in the Table 4.1. The device shows a very good resolution, better than 30 pA for all channels.

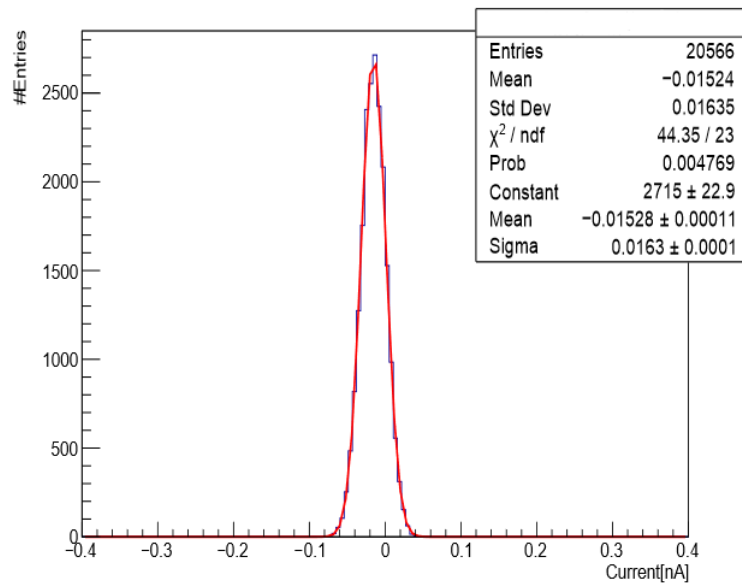


Figure 4.16: Output current at null input after temperature correction: resolution for CH1 of PICO is 16.3 ± 0.1 pA. A Gaussian shape distribution is present as expected in the case of a distribution of white noise.

4.2.3 Evaluation of the resolution and of the thermal dependence of the output voltage

Similarly to what was explained in the previous Section 4.2.2, the procedure to retrieve the parameters for the thermal correction of the output voltage were carried out in the following conditions:

- PICO switched ON;
- A1515 power supply was disconnected by the pico-ammeter (HV = 0 V);
- PICO was shielded using a copper foil;

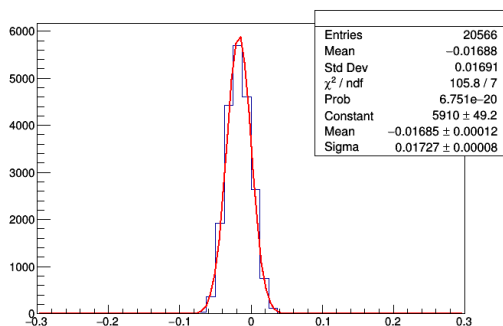


Figure 4.17: Output current at null input after temperature correction: resolution for CH2 of PICO is 17.30 ± 0.08 pA.

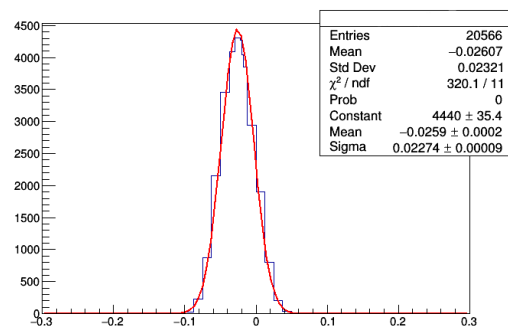


Figure 4.18: Output current at null input after temperature correction: resolution for CH3 of PICO is 22.70 ± 0.09 pA.

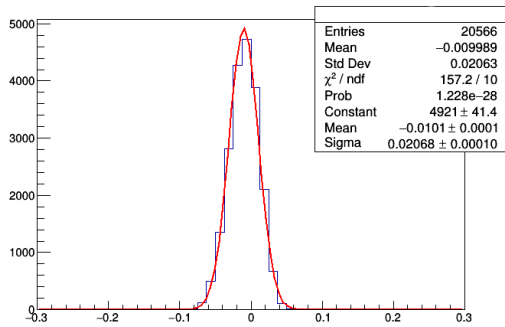


Figure 4.19: Output current at null input after temperature correction: resolution for CH4 of PICO is 20.7 ± 0.1 pA.

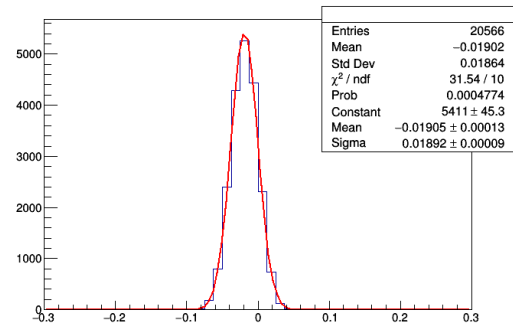


Figure 4.20: Output current at null input after temperature correction: resolution for CH5 of PICO is 18.90 ± 0.09 pA.

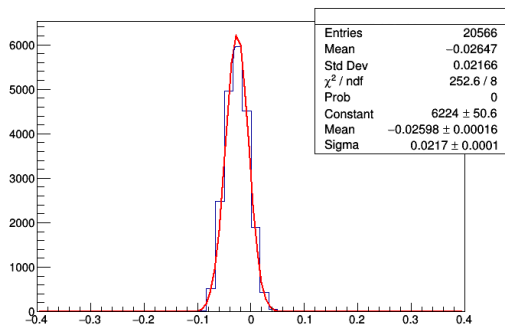


Figure 4.21: Output current at null input after temperature correction: resolution for CH6 of PICO is 21.7 ± 0.1 pA.

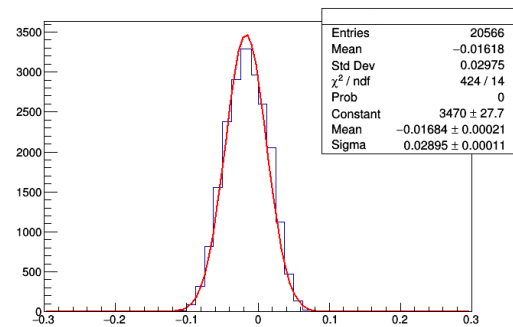


Figure 4.22: Output current at null input after temperature correction: resolution for CH7 of PICO is 27.95 ± 0.11 pA.

HV[V]	Channel	σ (pA)
0	CH1	16.30 ± 0.10
0	CH2	17.30 ± 0.08
0	CH3	22.70 ± 0.09
0	CH4	20.70 ± 0.10
0	CH5	18.90 ± 0.09
0	CH6	21.70 ± 0.10
0	CH7	27.95 ± 0.11

Table 4.1: Current resolution for all channel of PICO for null input: the device has an overall current resolution below 30 pA.

- Acquisition time: 72 h;
- Downsample: 1.

Figure 4.23 shows the output voltage values recorded for CH1. The histogram shows a distribution that have a non-Gaussian shape due to thermal variation, retrieving a similar trend as the one of the output current.

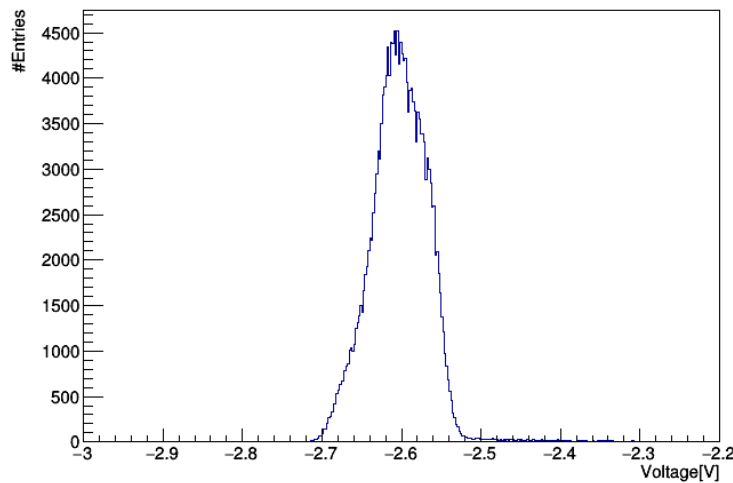


Figure 4.23: The output voltage recorded by the CH1 of PICO disconnected from A1515 (HV = 0): the histograms shown a distribution that have a non-Gaussian shape due to thermal variation.

The thermal correction procedure for the output voltage was implemented starting from the trend of the voltage as a function of temperature, analogously to what has been described for the current (see Section 4.2.2). Also in this case, the correction parameters were retrieved by means of a linear fit performed separately for each channel.

In Figure 4.24 the fit function used for the voltage correction is shown: the parameter $p_1 = -0.0073 \pm 0.0050 \text{ V/[AU]}$ expresses the voltage variation in correspondence with a

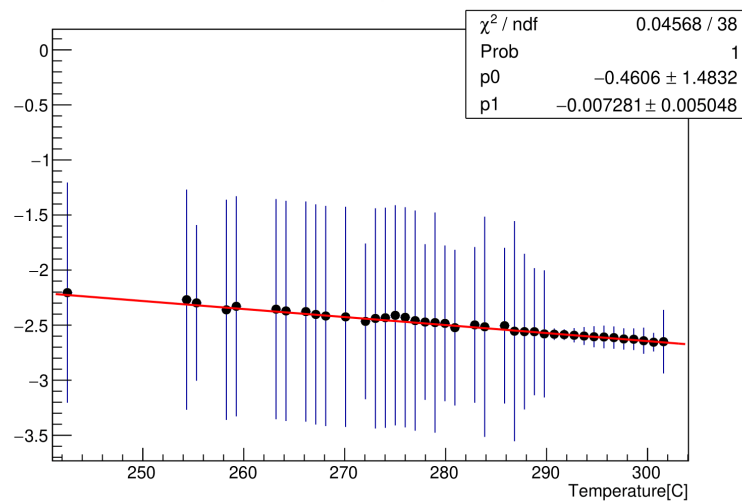


Figure 4.24: The output voltage as function of temperature: the fit parameters were used to obtain the corrective factor for the voltage values. The parameter $p_1 = -0.007 \text{ nA}/[\text{AU}]$ expresses the current variation in correspondence with a temperature variation of 1 AU which correspond to a variation of $0.3 \text{ }^\circ\text{C}$. This corresponds to a voltage variation of about 24 mV per unit $^\circ\text{C}$.

temperature variation of 1 AU which correspond to a variation of $0.3 \text{ }^\circ\text{C}$. This involves a voltage variation of the order of 15 mV per unit $^\circ\text{C}$.

The output voltage resolution for CH1 of PICO after the temperature correction is shown in Figure 4.25. As expected, the distribution shows a Gaussian shape and the output voltage resolution is equal to $12.9 \pm 0.02 \text{ mV}$. The resolution for all the channels,

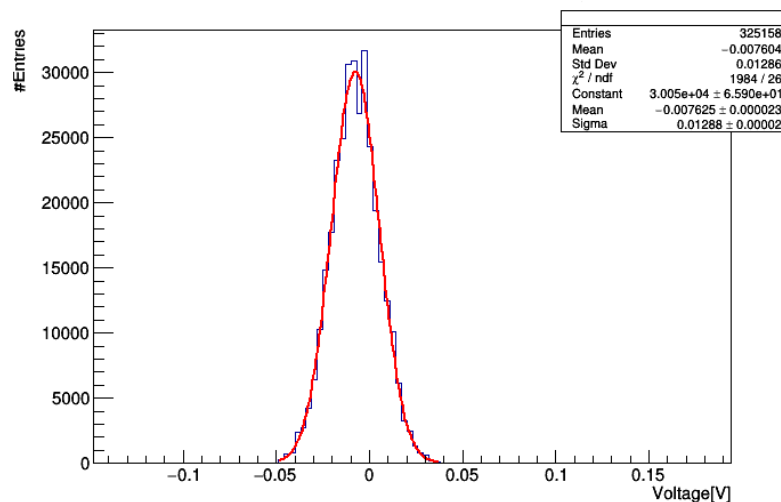


Figure 4.25: The output voltage after temperature correction for CH1 of PICO: resolution for CH1 of PICO is $12.9 \pm 0.02 \text{ mV}$. This value is in accordance with what is reported in the technical specifications of the A1515: a maximum Voltage Ripple equal to 15 mV is reported.

after the thermal correction, is reported in Table 4.2. As a summary, for a null input, the device shows a very good voltage resolution better than 14 mV overall the channels.

HV[V]	Channel	σ [mV]
0	CH1	12.9 ± 0.02
0	CH2	12.8 ± 0.02
0	CH3	12.9 ± 0.02
0	CH4	13.7 ± 0.02
0	CH5	12.8 ± 0.02
0	CH6	13.6 ± 0.02
0	CH7	12.2 ± 0.02

Table 4.2: Voltage resolution for all channel of PICO: the device has an overall resolution below 15 mV in accordance with the max voltage ripple value reported in the technical specifications of the A1515.

In order to verify if the resolution of the device is comparable to that obtained in the case of null input (HV=0 V), the procedure has been repeated after setting a voltage of 250 V on each PICO electrode. The data taking was performed with the following conditions:

- PICO switched ON;
- PICO connected to A1515 powerd up at (HV = 250 V on each channel);
- PICO was shielded by using a copper foil;
- Acquisition time: 2 h;
- Downsample: 1.

As a cross check, the output voltage thermal correction was implemented also for the case with the HV switched ON, by using the same procedure as previously described. In Figure 4.23 the output of the voltage values recorded by the CH1 of PICO connected to the A1515 (HV = 250 V) is shown. This electrode was powered at -1500 V. By means of a linear fit, the thermal parameters were retrieved. In the Figure 4.27 the fit line used for the voltage correction is shown: the parameter $p_1 = -0.0053 \pm 0.0015$ V/[AU] is consistent with the value of p_1 of the fit line in Figure 4.24, taken at an input HV=0.

The voltage resolution for CH1 of PICO after the temperature correction is shown in Figure 4.28: the distribution of the voltage values following the correction have a Gaussian shape and the voltage resolution is equal to 32.4 ± 0.02 mV. Output voltage resolution for all channels, at $HV^{\text{input}}=250$ V are reported in Table 4.3.

The slight increase in the sigma of the output voltage distributions from $HV^{\text{input}}=0$ V and $HV^{\text{input}}=250$ V, can be ascribed to the electronic noise (ripple) of the A1515 board.

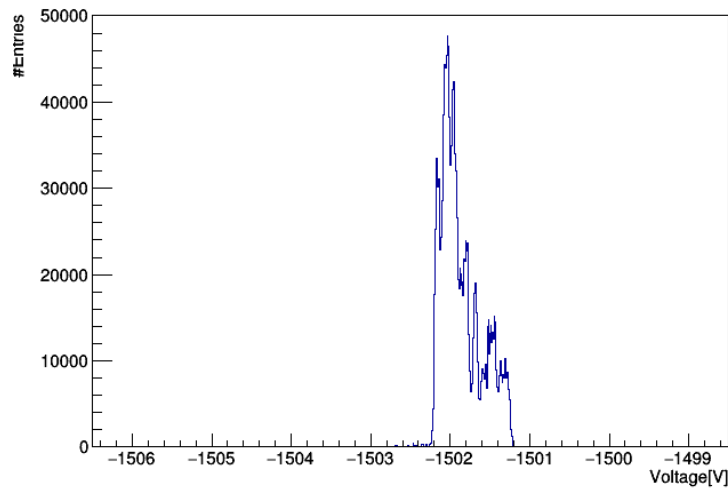


Figure 4.26: The output of the voltage values recorded by the CH1 of PICO connected to the A1515 (HV = 250 V): the histogram have a non-Gaussian shape due to thermal variation. In particular, the electrode corresponding to the CH1 should have an average value centered around -1500 V.

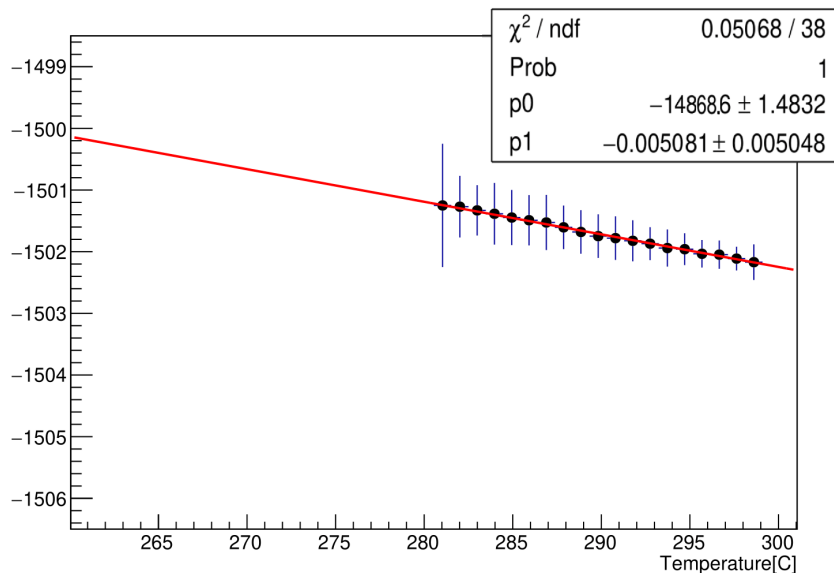


Figure 4.27: The output voltage as function of temperature: the fit parameters were used to obtain the corrective factor for the voltage values. The parameter $p_1 = -0.005 \text{ nA}/[\text{AU}]$ expresses the current variation in correspondence with a temperature variation of 1 AU which correspond to a variation of $0.3 \text{ }^\circ\text{C}$. This corresponds to a voltage variation of about 17 mV per unit $^\circ\text{C}$.

HV[V]	Channel	σ (mV)
-1750	CH7	32.4 ± 0.02
-1500	CH1	35.7 ± 0.02
-1250	CH2	24.5 ± 0.01
-1000	CH3	24.6 ± 0.01
-750	CH4	21.5 ± 0.01
-500	CH5	15.6 ± 0.01
-250	CH6	14.8 ± 0.01

Table 4.3: Voltage resolution for all channel of PICO: the instrument has an overall resolution below 40 mV. The resolution values are not appreciably different from those reported in Table 4.2.

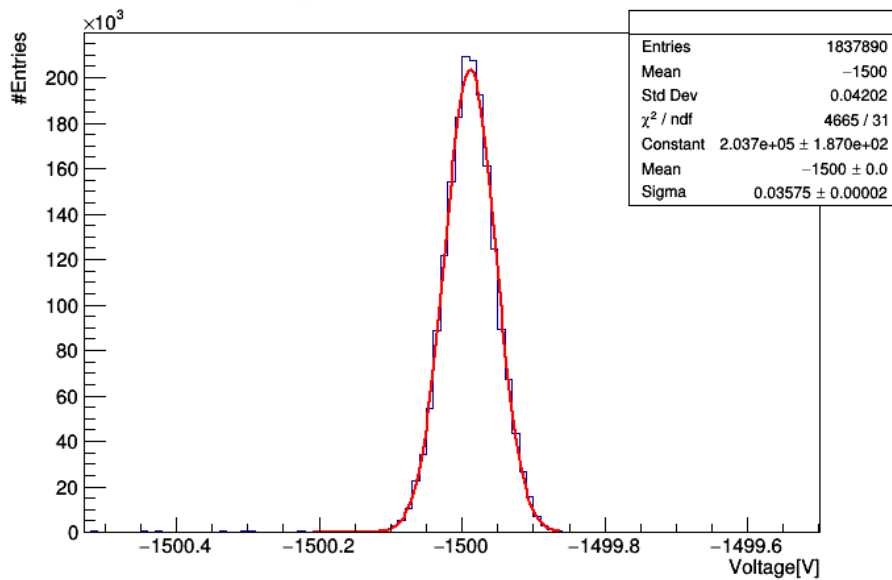


Figure 4.28: The output of the voltage values recorded by the CH1 of PICO connected from A1515 (HV = 250 V): the histograms have a Gaussian shape following the temperature correction. In particular, the electrode corresponding to the CH1 have an average value centered around -1500 V as expected.

Chapter 5

Characterization of a Triple-GEM detector prototype for the CMS Muon System Upgrade

Introduction

After the phase II HL-LHC upgrade, the collision rate and the background rate will significantly increase particularly in the high η region, as we have seen in Section 2.4. To improve both the tracking and triggering of muons, the CMS collaboration installed and will install new station of Triple-GEM detectors in the CMS muon endcaps.

During this thesis work, a characterization of a Triple-GEM detector prototype for the CMS Muon System Upgrade was carried out. This prototype has very similar characteristics to the Triple-GEM used by the CMS collaboration. However, the two detectors differ in:

- size: the prototype used has a much smaller sensitive area than the GEM cameras used by the CMS collaboration;
- read-out plan: it is possible to providing a 2D information on the position of the signal unlike the 1D reading of the CMS chambers.

Moreover, this prototype allows to set up an analysis with PICO: most of the studies carried out during this thesis work required the use of PICO, taking into account the evaluations made in the previous chapter. The study of the detector response was therefore carried out using PICO and a digitizer. The results obtained in the optimization of the electric fields inside the Triple-GEM prototype are then displayed. Eventually, gain measurements and gain uniformity of the prototype were carried out.

5.1 Experimental Setup

The experimental setup used for the characterization of the Triple-GEM detector is schematized in the Figure 5.1 and hosts:

- PICO (described in the previous chapter),

- a Power Supply (SY4527) with a single width board (A1515),
- an advanced DC power supply with single or triple output (QL355TP),
- a digitizer (DT5725),
- an oscilloscope,
- gas cylinders containing respectively N or Ar – CO₂ (70:30),
- a shielding box containing the HV filter, the Triple-GEM detector and the amplifier,
- a flow meter through which it is possible to regulate the quantity of gas to be injected inside the Triple-GEM detector.

The Triple-GEM detector setup in working conditions makes use of Ar – CO₂ mixture as ionizing medium while the electric fields, that allow multiplication, are powered by the HV system.

The gas is injected from the Ar – CO₂ gas cylinder, connected through a tube and a flow meter to the shielding box that contains the Triple-GEM prototype. Hence, Ar – CO₂ (70:30) is the mixture used under data taking conditions. During the inactivity phases nitrogen is sometimes fluxed in order to clean the chamber from any dust deposited inside the detector. Through the flow meter it is possible to set the gas flux to be injected. The detector is equipped with a gas outlet pipe connected to a second flow meter placed on the opposite side of the box. The two flow meters makes possible to supervise any gas leaks. During this thesis work, the gas flux was chosen equal to 0.3 *Litres per Minute* (LPM).

The high-voltage HV necessary for the detector to reach working conditions is provided by a power supply via the single A1515 board. The board is connected via cables to the shielding box. The HV then goes through to a HV filter before reaching the detector. By connecting the A1515 as PICO input and the latter in input to the HV filter, it is possible to observe the voltage/current response of the detector through the use of a custom developed LabView software as shown in Section 4.2. The Triple-GEM also sends out 4 analog signals in correspondence of 4 sets of reading strips (see Section 5.2). An amplifier, located inside the shielding box, is connected to the Triple-GEM output to enhance its signal. The output can be read trough an oscilloscope or digitizer thanks to the 4 sets of reading strips present on the Triple-GEM read-out electrode. Similarly, In the following sections, a more detailed description of the tools used is provided.

Power Supply (SY4527) and Board (A1515)

The SY4527 is a power supply (PS) system. It represents the state-of-the-art for what concerns CAEN's High Voltage and Low Voltage Power Supplying. It allows the housing, in the same mainframe, of a wide range of boards with different functions, such as High/Low Voltage boards, generic I/O boards (temperature, pressure monitors, etc.). The mainframe hosts the *Board Section*, with 16 slots to house boards, distributors and branch controllers. The A1515 [12] are single width boards that house 16 independent, fully floating high voltage individual channels and witch are perfectly suited for GEM detectors. A view of PS and A1515 is shown in Figure 5.3.

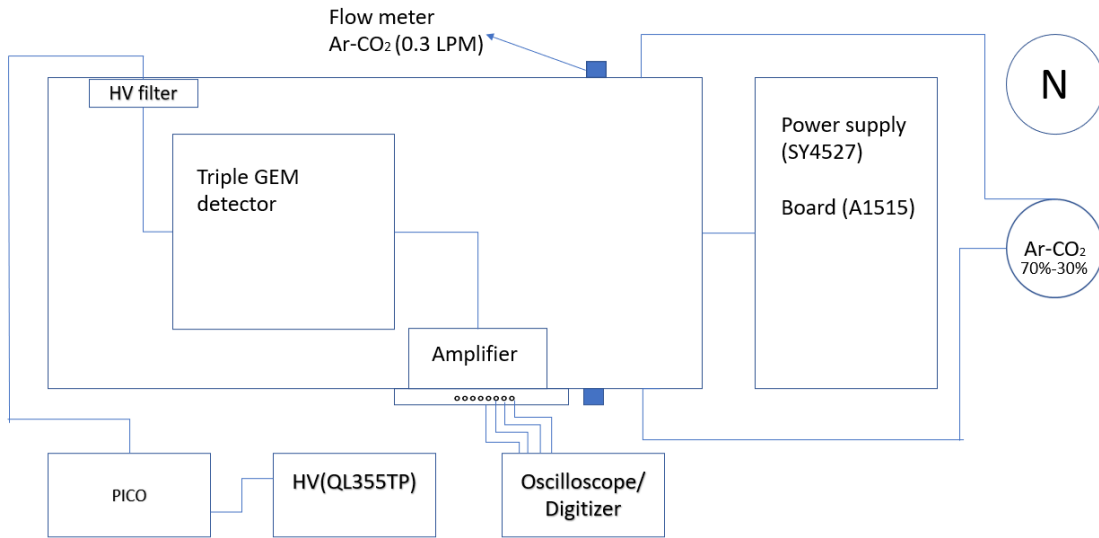


Figure 5.1: The Experimental Setup.



Figure 5.2: Power Supply (SY4527).



Figure 5.3: Board (A1515).

Advanced DC power supply QL35TP

In the linear DC power supply QL35TP (Figure 5.4) voltage and current are controlled using 16 bit DACs enabling voltages to be set to 1 mV resolution, even at full output voltage.

Digitizer DT5725

The Digitizer DT5725 [13] is a 8-channel device with independent acquisition for each one. The incoming pulses are read by a flash-ADC with 14 bit resolution and sampling rate of 250 MS/s. It is characterized by 0.5 and 2 V_{pp} selectable input dynamic range with programmable DC offset adjustment. The DC offset can be identified with the average signal amplitude: if the mean amplitude is zero this will also be the DC offset. Using the DPP (Digital Pulse Processing) firmware, it is possible to acquire physical parameters such as integrated charge, to discriminate the pulse shape with very fine time resolu-



Figure 5.4: The advanced DC power supply QL35TP.

tion, to perform pulse height analysis. In Figure 5.5 an image of the device is shown. Eventually, the acquisition of the output data from the digitizer is carried out using the CoMPASS (CAEN Multi-PARameter Spectroscopy Software) software [14]. CoMPASS is the DAQ software from CAEN able to implement a Multiparametric Data Acquisition for Physics Applications: the detectors can be connected directly to the digitizers inputs and the software acquires energy, timing, and PSD spectra at the same time.



Figure 5.5: The Digitizer DT5725.

5.2 Triple-GEM detector prototype: main features

The operating principle of a generic gas detector and, specifically, the main characteristics of a Triple-GEM detector have been described in detail in Chapter 3. In this section, an accurate description of the Triple-GEM detector prototype used during this thesis work is provided, highlighting its peculiarities and structure.

In Figure 5.6 a scheme of the Triple-GEM prototype is reported. The device has 7 electrodes, in addition to the read-out one, which we will indicate below with Drift, GE1T, GE1B, GE2T, GE2B, GE3T, GE3B. Conventionally, the 3 GEM foils, GE1,

GE2 and, GE3, have been numbered starting from the foil facing the cathode, distinguishing the top side from the bottom side of the single GEM detector. Given the distance between the electrodes, the structure of this Triple-GEM prototype is defined as *standard* or ‘3:1:2:1 structure’. The values respectively represent the thickness of the zones of DRIFT, Transfer 1 (TR1), Transfer 2 (TR2) and, INDUCTION.

When a charged particle passes through the Triple-GEM detector, electron-ion pairs are created as seen in Section 3.3.

The ionization produced in the drift gap, once multiplied by three GEM foils, induces most of the signal. In transfer gaps, secondary electrons are extracted from a GEM and transported to the next. Hence, the electric field in the transfer gap (\vec{E}_{TR}) is an important parameter to optimize charge mobility. A high \vec{E}_{TR} is necessary to ensure good extraction capacity of the secondary electrons from the upper GEM to the transfer gap; conversely, \vec{E}_{TR} must be kept low to reduce the defocusing effect and to have a high collection efficiency in the lower GEM. Eventually, the induction field \vec{E}_I must be as high as possible, avoiding however instability of the detector, to increase the ability to extract electrons from the third GEM.

The amount of electron collected with respect to the read-out electrode and, consequently, the effective gain of the detector as defined in Section 3.4.3, depends on the intensity and the overall structure of the electric field inside the GEM. The electric field in fact varies in intensity and shape inside of the Triple-GEM detector. The electric field is determined by the potential difference applied between the triple-GEM electrodes thanks to the HV system. We therefore define the potential differences applied between the top and bottom side of the GEM foil as ΔV_{GE1} , ΔV_{GE2} and, ΔV_{GE3} .

The detector has a $10\text{cm} \times 10\text{cm}$ sensitive area. It structurally consists of a read-out plane (anode), 3 GEM foils, spacer frames used to increase the gas flow, a drift plane (cathode) and, a cover system as shown in Figure 5.7.

The insulating polymer used for each foil is Kapton, with a thickness of $50\ \mu\text{m}$ coated on both sides from $5\ \mu\text{m}$ of copper. The read-out plane hosts 256 strips read in groups of 128 in both x and y direction unlike the Triple-GEM used in CMS in which the reading occurs in one direction only. This allows the 4 reading channels to be connected to the oscilloscope/digitizer providing a 2D information on the position of the signal. Figure 5.8 shows the complete assembly scheme for the detector used.

When a voltage is applied between the top and bottom side of the GEM foil, a current flows from top to bottom which is mainly driven by the surface conductivity of the foil (also called *leakage current*). This current highly depends upon the defects and contamination in the foil. Each GEM foil is tested at every assembling stage to check the resistivity r with the Megger MIT420 (see Figure 5.9). The check is done to ensure the two layers are not accidentally put in contact because of impurities of the insulator. Typical values for the resistivity are $r > 50\ \text{G}\Omega$ for $\Delta V_{applied} = 250\ \text{V}$ or $r > 100\ \text{G}\Omega$ for $\Delta V_{applied} = 500\ \text{V}$. The working point of the foil is selected roughly equal to $\Delta V_{applied} = 450\ \text{V}$.

In the following sections, the optimization of the electric fields are explained as well as the current-voltage curves for GE1, GE2, GE3.

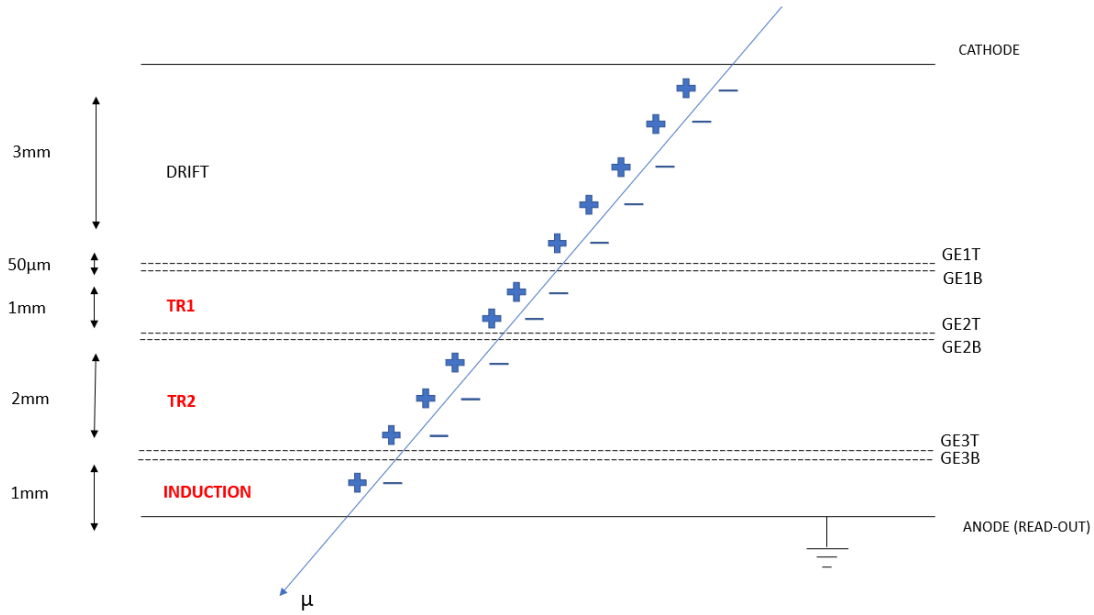


Figure 5.6: Diagram of the Triple-GEM detector prototype: the structure has 7 electrodes, in addition to the read-out one. The Triple-GEM prototype is defined as *standard* or ‘3:1:2:1 structure’. The values respectively represent the thickness of the zones of DRIFT, Transfer 1 (TR1), Transfer 2 (TR2) and, INDUCTION. The ionization produced in the drift gap induces most of the signal. In transfer gaps, secondary electrons are extracted from a GEM and transported to the next. The electric field varies in intensity and shape inside of the Triple-GEM detector. A high \bar{E}_{TR} is necessary to ensure good extraction capacity of the secondary electrons from the upper GEM to the transfer gap; conversely, \bar{E}_{TR} must be kept low to reduce the defocusing effect and to have a high collection efficiency in the lower GEM. Eventually, the induction field \bar{E}_I must be as high as possible, avoiding however instability of the detector, to increase the ability to extract electrons from the third GEM.

Current measurements and source used

For the current measurements it was used ^{55}Fe as X -ray source. ^{55}Fe decays via electron capture as ^{55}Mn with a half-life of 2.737 years. As X -rays pass inside the detector, they interact with gas molecules through photoelectric absorption. In the majority of the cases a photoelectron and an Auger electron are emitted and the full energy is deposited in the sensitive volume of the detector and thus detected. The peak position in an energy spectrum is proportional to the energy of the X -ray: the main peak of ^{55}Fe is at 5.9 KeV. In most of the cases the whole photon’s energy is absorbed and used to produce primary ionization electrons. Sometimes the photon extracts an electron from the inner K-shell of Ar and the vacancy is filled by an electron, with the emission of another X -ray photon of 2.9 KeV. In the ^{55}Fe spectrum this peak is called *escape peak*. The use of this source therefore guarantees the maximization of the interaction rate as well as the efficiency of the detector. For more details on the emission spectrum of ^{55}Fe see Section 5.7.

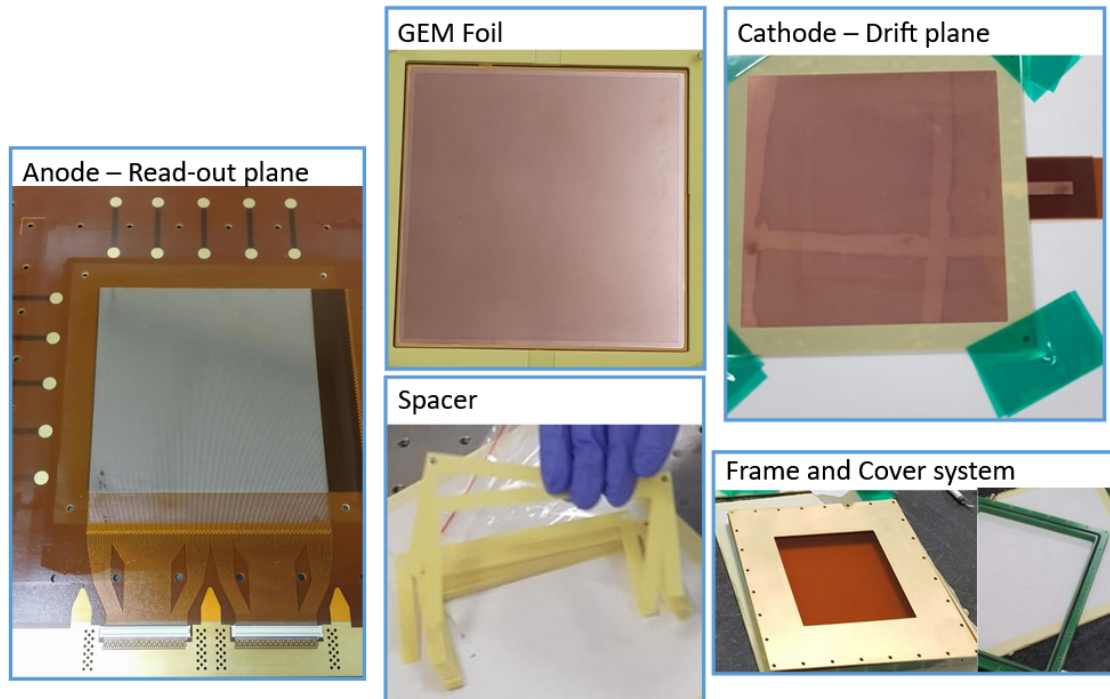


Figure 5.7: The Triple-GEM components.

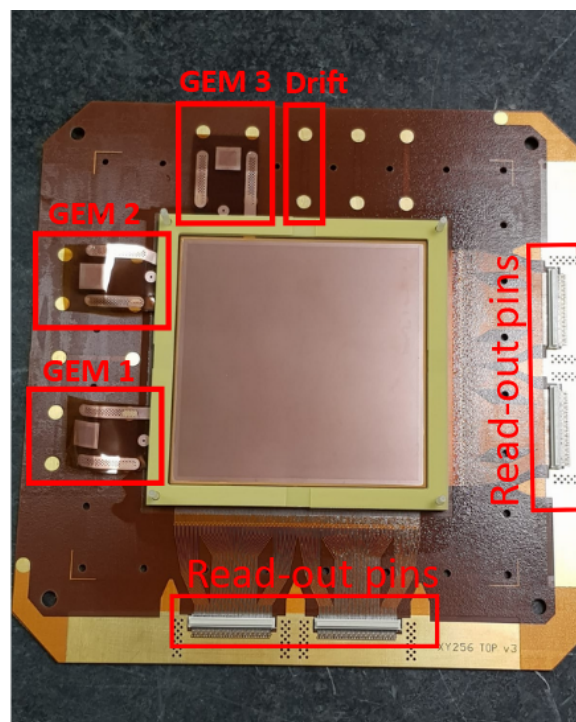


Figure 5.8: The Triple-GEM structure: the outputs related to the 3 GEM foils, the drift and read-out pin corresponding to the two groups of 128 strips both along the horizontal and vertical axis are shown. The 4 reading channels can be connected in input to an oscilloscope/digitizer to view the detector output.



Figure 5.9: The Megger MIT420.

5.3 Optimization of Electric Field

In order to maximize the amount of electrons that are collected on the read-out electrode, it is crucial to choose the electric fields appropriately. In particular, the value of the electric field must allow a good electron extraction efficiency from the lower electrode of the previous GEM foil. At the same time, \bar{E} must guarantee a good electron transfer efficiency towards the top electrode of the next GEM.

This section then describes the procedure for optimizing the electric fields starting from the measurement of the initial current I_{GE3T} that can be read at the electrode corresponding to the top layer of the last GEM foil. For the current measurements which will be discussed in this section, the pico-ammeter, described in Chapter 4, was used. The system was set up so that the electrodes from GE1T to GE3B will correspond respectively to the channel from CH1 to CH6 of the pico-ammeter, the Drift electrode will correspond to the CH7.

We start by describing the procedure to optimize the electric field in TR1. The procedure was carried out as follows:

- The electric field related to section TR1, \bar{E}_{TR1} , has been varied from 0 to 5 kV/cm. \bar{E}_{TR2} and \bar{E}_I was set respectively equal to 1.95 kV/cm and 3.9 kV/cm.
- Current measurements were carried out by placing an ^{55}Fe source in the center of the sensitive area of the Triple-GEM. The absolute value of the current depends on

geometric acceptance of the detector, angular distribution of the source radiation and its activity.

- Given the output current values recorded by PICO, suitably corrected according to the procedure explained in the Section 4.2.2, the average value of I_{GE3T} was considered for each of the 19 data acquisition performed.

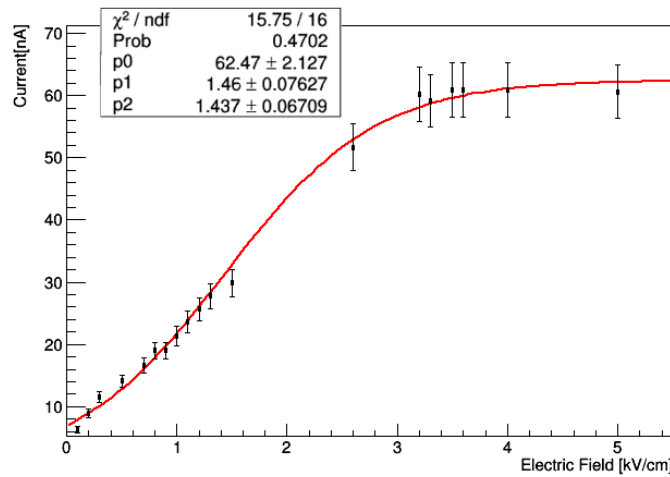


Figure 5.10: Optimization of Electric Field for TR1. The average value of I_{GE3T} , expressed in nA, as function of the electric field, expressed in kV/cm: the current measurement assumes a value approximately equal to zero in correspondence with a null field. As the electric field increases, the intensity of the current increases: a plateau zone is reached which corresponds to the optimal electric field value for the amount of electrons collected to the read-out. For the TR1, the plateau is reached for electric field values approximately equal to 3.5 kV/cm.

In Figure 5.10 the average value of I_{GE3T} as function of the electric field is shown. As expected, the current measurements assumes a value approximately equal to zero in correspondence with a null field. For low values of the electric field, $\bar{E}_{TR1} < 2$ kV/cm, the transport of electrons towards the anode is not very efficient. In this case, in fact, the electrons are extracted from the hole of the first GEM, but they are collected on the electrode GE1B. As the rise of the electric field, the intensity of the current increases. A plateau zone is reached which corresponds to the optimal electric field value for collecting electrons. For the TR1, the plateau is reached for electric field values approximately equal to 3.5 kV/cm. The fit function has been implemented as follows:

$$\text{Sig}(\bar{E}) = \frac{p_0}{1 + \exp[-p_1 \cdot (x - p_2)]} \quad (5.1)$$

where the parameter p_0 corresponds to the plateau value of the current. The uncertainty on each current value is chosen equal to the RMS of the current output distribution.

The optimisation of the electric field for TR2 was carried out with a similar procedure. In Figure 5.11 the average value of I_{GE3T} as function of the electric field is shown. As expected, the current measurement assumes a value approximately equal to zero in correspondence with a null field. As the electric field increases, the intensity of the current

increases. In this case, however, it was not possible to observe the plateau zone. In fact, the increase in the intensity of the field involves an increase in the probability of discharge inside the detector. In order to avoid permanent damage to the detector, it was decided not to increase the intensity of the electric field beyond 3.3 kV/cm.

Similarly to the previous case, the fit function used is the sigmoid function in the Equation 5.1. In this case, however, the implemented function does not exactly meet the requirements for the plateau zone due to the impossibility of its achievement.

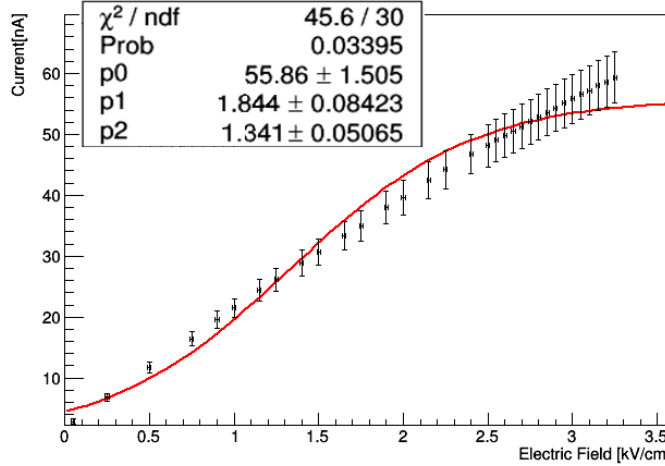


Figure 5.11: Optimization of Electric Field for TR2. The average value of I_{GE3T} , expressed in nA, as function of the electric field, expressed in kV/cm: the current measurement assumes a value approximately equal to zero in correspondence with a null field. As the electric field increases, the intensity of the current increases. In this case, however, it was not possible to observe the plateau zone. In fact, the increase in the intensity of the field involves an increase in the probability of discharge inside the detector. In order to avoid permanent damage to the detector, it was decided not to increase the intensity of the electric field.

5.4 Current voltage curve for GE1, GE2, GE3

Following the field optimization procedure, current measurements were carried out to provide information on the gain of the detector. The effective gain of a Triple-GEM is defined as the average number of electrons reaching the anode for each primary ionization, as we have seen in Section 3.4.3. Hence, this quantity will be proportional to the current I_{GE3B} immediately present at the output of the GE3B electrode (see diagram in Figure 5.6). We have seen that at low electric field values the current collected by the read-out is about zero. As the potential difference at the ends of each GEM increases, an increase in current occurs, following the three amplification stages.

Hence, in order to obtain the voltage-current curves for the GE1, GE2, and GE3 of the detector, the procedure was carried out:

- The values of ΔV_{GE2} and ΔV_{GE3} have been set respectively equal to 390 V.

- Current measurements were carried out by placing an ^{55}Fe source in the center of the sensitive area of the Triple-GEM detector.
- 31 sets of measurements were carried out with ΔV_{GE1} varying from 1 V to 390 V in steps of 10 V for which we reported the output of current I_{GE3T} of the GE3T electrode.

In Figure 5.12 the voltage-current curve for the GE1 is shown. On the vertical axis the values of the output current are expressed in nA, on the horizontal axis the ΔV_{GE1} expressed in V. For low values of ΔV_{GE1} , the recombination of electrons in proximity to the cathode prevails; the electrons, in fact, are not sufficiently accelerated and consequently the read-out current is minimal. In correspondence of ΔV_{GE1} higher than 250 V, an exponential increase in the current is observed. The fit function has been implemented in

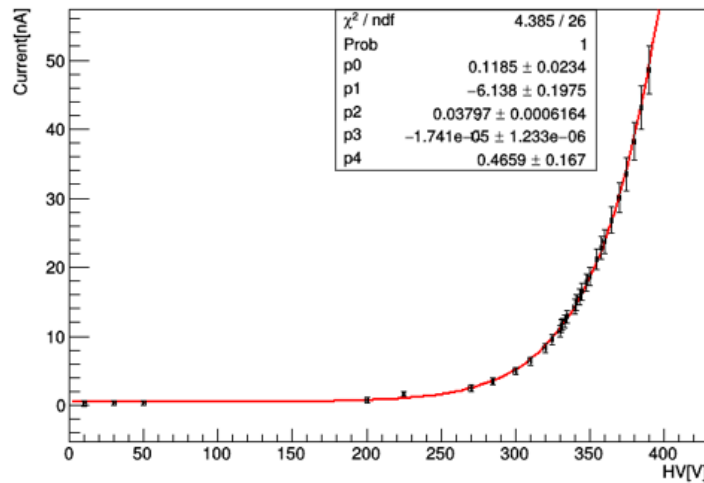


Figure 5.12: Voltage-Current curves for the GE1: for low values of ΔV_{GE1} , the recombination of electrons in proximity to the cathode prevails; the electrons, in fact, are not sufficiently accelerated and consequently the read-out current is minimal. In correspondence of ΔV_{GE1} higher than 250 V, an exponential increase in the current is observed. The fit function is the Equation 5.2. The uncertainty on the average value of the current is equal to the RMS of the distribution.

the following way:

$$f(HV) = p_4 + p_0 \cdot \exp[p_1 + p_2 \cdot x + p_3 \cdot x^2] \quad (5.2)$$

This function allows to unify two different regimes: the low voltage regime corresponding to approximately zero current and the exponential increase regime of the current.

The procedure was repeated for GE2 and GE3, by varying respectively ΔV_{GE2} and ΔV_{GE3} . In both cases the potential differences of the other two GEM foils were set at 390 V. The corresponding curves are reported in Figures 5.13 and 5.14.

The Figure 5.15 instead, shows the trend observed for ΔV_{GE3} values higher than 300 V: the current as a function of ΔV_{GE3} in this case presents a purely exponential trend as

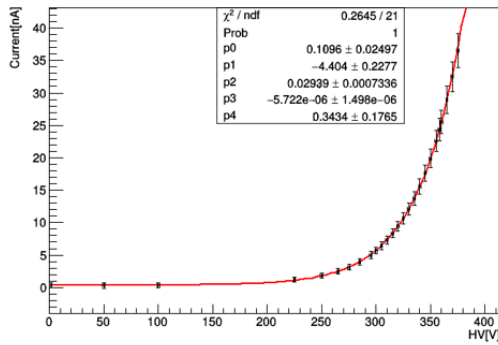


Figure 5.13: Voltage-Current curves for the GE2.

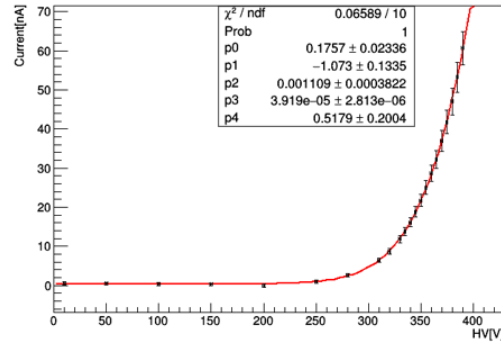


Figure 5.14: Voltage-Current curves for the GE3.

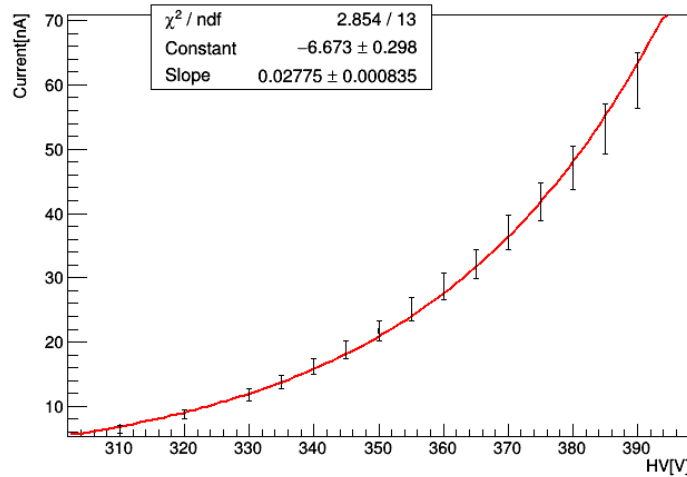


Figure 5.15: Current as a function of ΔV_{GE3} : purely exponential trend as expected following the increase of the amount of electrons collected by the read-out is shown. The uncertainty on the average value of the current is equal to the RMS of the distribution.

expected following the increase of the amount of electrons collected by the read-out. The uncertainty on the average value of the current is equal to the RMS of the distribution.

As cross check about the current resolution of PICO in case the device is connected to the Triple-GEM prototype and to the A1515, the outputs current for two different values of ΔV_{GE3} was reconstructed as shown in Figures 5.16 and 5.17. A worse resolution in current can be observed. The current fluctuation in this case depends on the activity of the source used. Therefore the resolution observed is linked to the statistical process of production of primary electrons and of the amplification of the three gem sheets. It also depends on the electronics and any errors in this area. therefore this resolution is not linked simply to PICO but to the Triple-GEM detector.

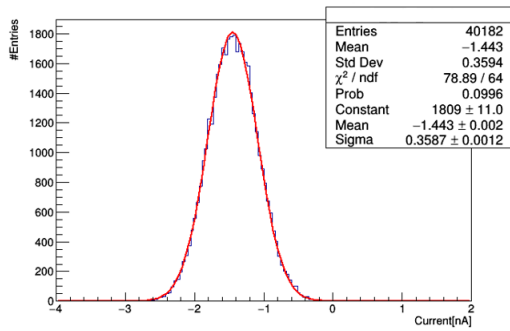


Figure 5.16: Output current for $\Delta V_{GE3} = 250$ V.

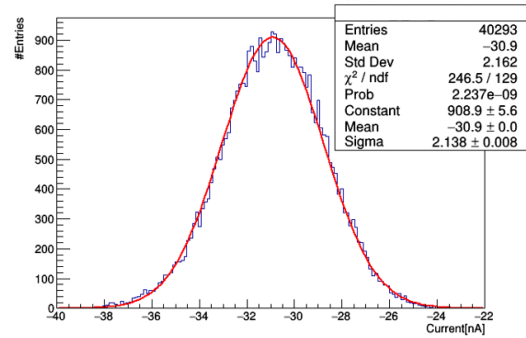


Figure 5.17: Output current for $\Delta V_{GE3} = 370$ V.

5.5 Uniformity gain measurements

In order to evaluate the gain uniformity of the detector, the sensitive area of the Triple-GEM was divided schematically in 9 cells, denominated 1C through 9C, as shown in Figure 5.18.

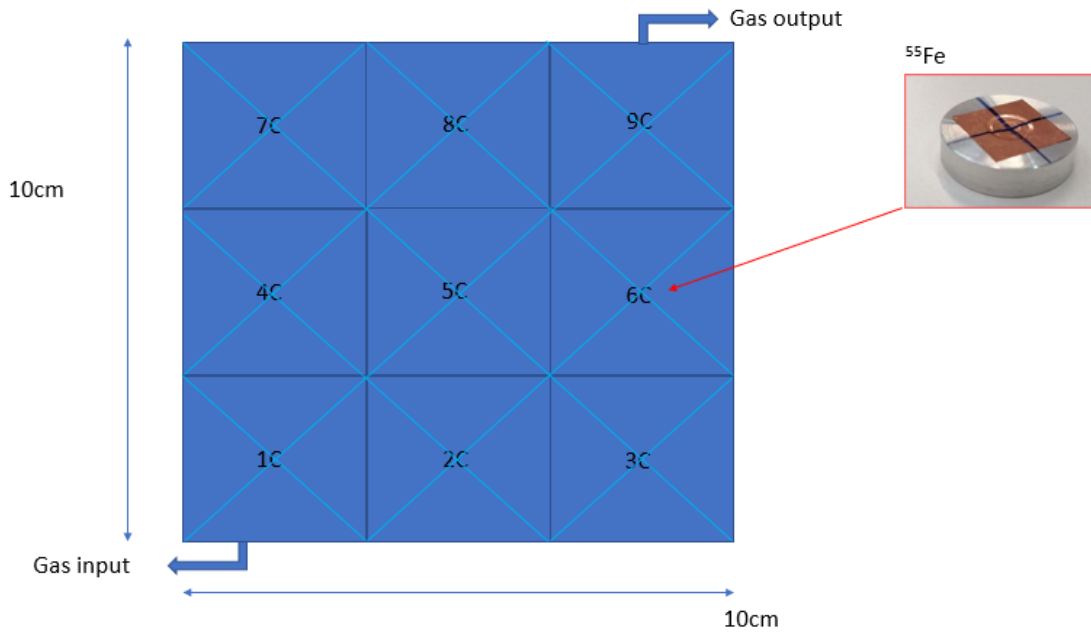


Figure 5.18: Division of the sensitive area of the Triple-GEM detector into 9 cells. An iron source (^{55}Fe) was placed in the center of each cell in order to carry out, through PICO, current measurements to evaluate the uniformity of the gain as the cell varies.

For the division a thin, suitably squared support was used, with dimensions equal to those of the sensitive area of the detector and positioned on top of it as shown in Figure 5.19. The gain is defined as the average number of primary electrons collected by the read-out electrode, as we have seen in Section 3.4.3. Hence, this quantity will be proportional to the current I_{GE3B} immediately present at the output of the GE3B electrode (see diagram in Figure 5.6).

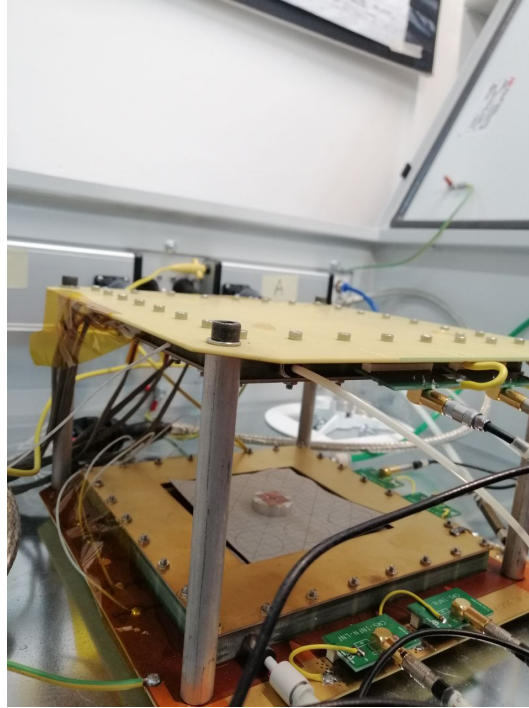


Figure 5.19: Experimental setup of uniformity gain measurements: the sensitive area of the Triple-GEM was divided schematically in 9 cells, denominated 1C through 9C. For the division a thin, suitably squared support was used, with dimensions equal to those of the sensitive area of the detector and positioned on top of it.

The current measurements were performed using PICO and the data taking procedure was carried out as follows:

- The values of ΔV_{GE1} , ΔV_{GE2} and, ΔV_{GE3} have been set respectively equal to 375 V, 375 V and, 385 V, typical values under standard conditions of use of the detector.
- Current measurements were carried out by placing an ^{55}Fe source in the center of each cell.
- 2 sets of measurements were carried out, each characterized by 9 acquisitions of the current values at the output of the GE3B electrode.

For the first set of measurements, the data analysis procedure was carried out as follows:

- Given the output current values recorded by PICO, suitably corrected according to the procedure explained in the Section 4.2.2, the average value of I_{GE3B} was considered for each of the 9 runs performed.
- The maximum was extracted from the 9 average values, which we indicate with $\text{Max}(I_{GE3B})$.
- The relative gain G_{rel} will therefore be proportional to the ratio $\frac{I_{GE3B}}{\text{Max}(I_{GE3B})}$.

In Figure 5.20 the result of the uniformity gain measurement for the first measurement set is shown: the cells 3C and 9C are those with lower gain. This effect is presumably

due to a worse gas flow in correspondence with the cell 3C. In correspondence with the cell 9C, on the other hand, the presence of the gas outlet pipe could lead to a decrease in gas flow with consequent worsening of the gain. This effect, however, could depend on a mis-alignment of the source with respect to the center of the cell.

The same analysis procedure was carried out for the second measurement set. In Figure 5.20 the result of the uniformity gain measurement for the second measurement set is shown: also in this case the cells from 1C to 3C and those on the vertical axis from 3C to 9C exhibit a lower gain than the other cells, however it is overall higher than the first set of measurements.

The mean value of the current I_{GE3B} was then reported as a function of the measurement set. As example, in Figure 5.22 the mean value of the I_{GE3B} as function of the measurement set is shown for the position 5C. The difference in current value between different sets, of the order of 0.7 nA, may depend on variation in pressure, temperature or gas flux within the Triple-GEM detector.

Eventually, the two measurements were combined by considering the non-weighted average for each each position.

Consequently, for each position from 1C to 9C, the value $I_{GE3B_{mean}}$ was obtained. Given the maximum of nine values, the value of $G_{rel} \propto I_{GE3B_{mean}} / \text{Max}(I_{GE3B_{mean}})$ has been reported in correspondence of each cell as shown in Figure 5.23. Also in this case, the cells 3C and 9C are those with lower gain.

The result of this procedure is that the overall relative gain is higher than 87% of the maximum value, while the average gain, from the average of the values, is greater than 94.6% of the maximum value.

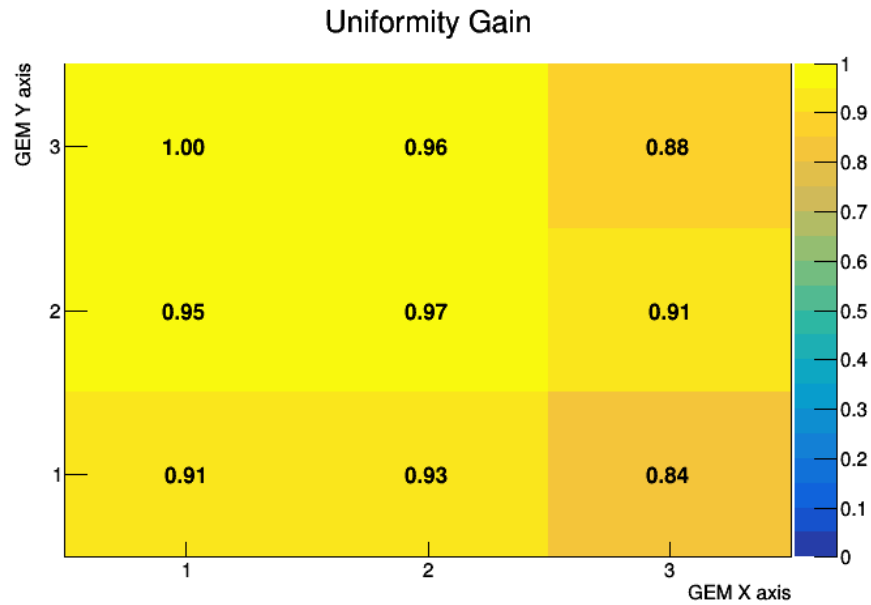


Figure 5.20: Result of the uniformity gain measurement for the first measurement set: the cells 3C and 9C are those with lower gain. This effect is presumably due to a worse gas flow in correspondence with the cell 3C. In correspondence with the cell 9C, on the other hand, the presence of the gas outlet pipe could lead to a decrease in gas flux with consequent worsening of the gain.

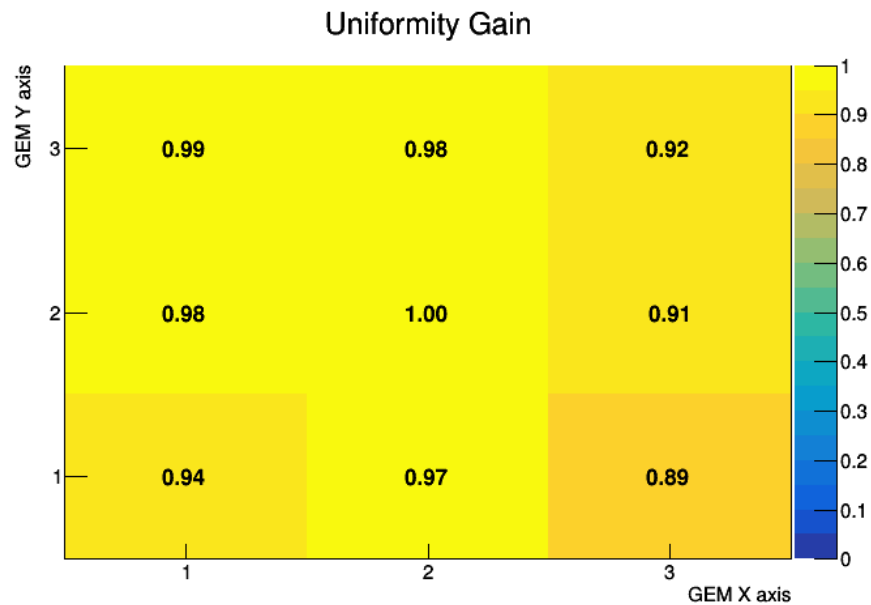


Figure 5.21: Result of the uniformity gain measurement for the second measurement set: the cells from 1C to 3C and those on the vertical axis from 3C to 9C exhibit a lower gain than the other cells, however it is overall higher than the first set of measurement shown in Figure 5.20.

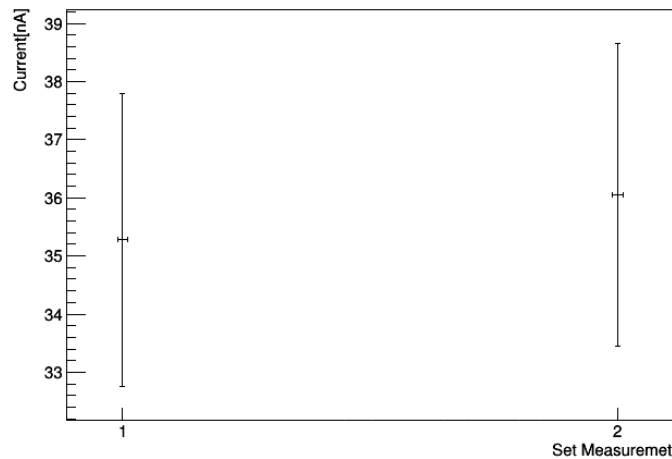


Figure 5.22: Mean value of the I_{GE3B} as function of the measurement set for the position 5C: the difference in current value between different sets, of the order of 0.7 nA, may depend on variation in pressure, temperature or gas flux within the Triple-GEM detector.

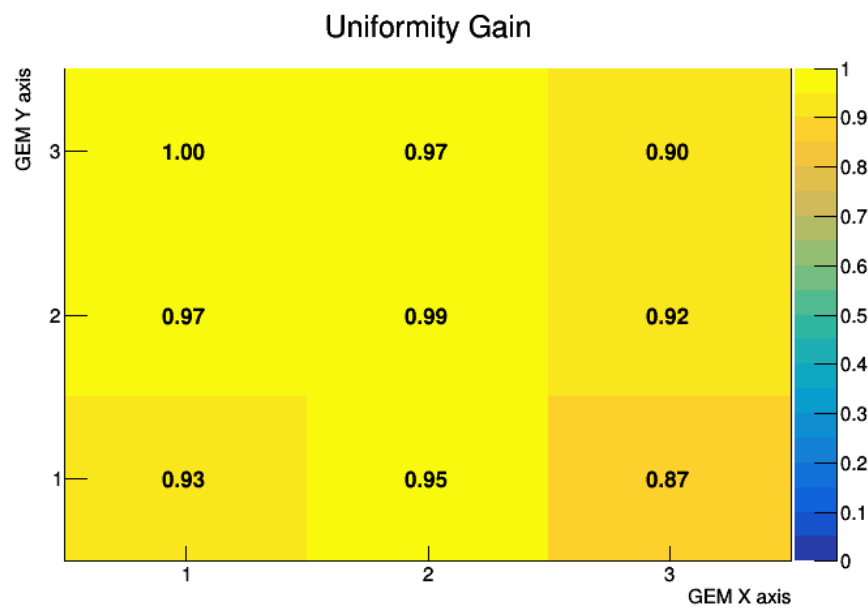


Figure 5.23: Result of the uniformity gain measurements: the two measurements were combined by considering the non-weighted average of current for each position. The result of this procedure is that the overall relative gain is higher than 87% of the maximum value, while the average gain, from the average of the values, is greater than 94.6% of the maximum value.

5.6 Calibration of Charge Sensitive Pre-Amplifier

A further study of the Triple-GEM detector response in terms of gain can be carried out by using a digitizer. The 4 reading channels of the read-out plane in fact, can be connected

to the oscilloscope/digitizer as shown in Section 5.2. In order to obtain the gain curves for the GE3, it was necessary to calibrate a Charge Sensitive Pre-Amplifier (CSP) for the conversion of the digitizer output, expressed in ADCcount, into charge expressed in fC.

A pulse generator (TGP110 10MHz Pulse Generator), an amplifier (A1422 Charge Sensitive Pre-Amplifier), and a digitizer (DT5725) were used for the calibration. The CSP test has been done by injecting pulses to the pre-amplifier input with an electronic pulser or waveform generator. Charge sensitive pre-amplifiers expect a brief pulse of current injected into the input. This was done by capacitively coupling a square wave generator to the pre-amplifier input.

The circuit works as a capacitive coupling, whose schematic diagram is shown in Figure 5.24. In our case, C_t is the test capacitance of 1 pF; V_{out} it will then be input to the digitizer. The wave generator is used to generate a square wave, applied to the CSP input

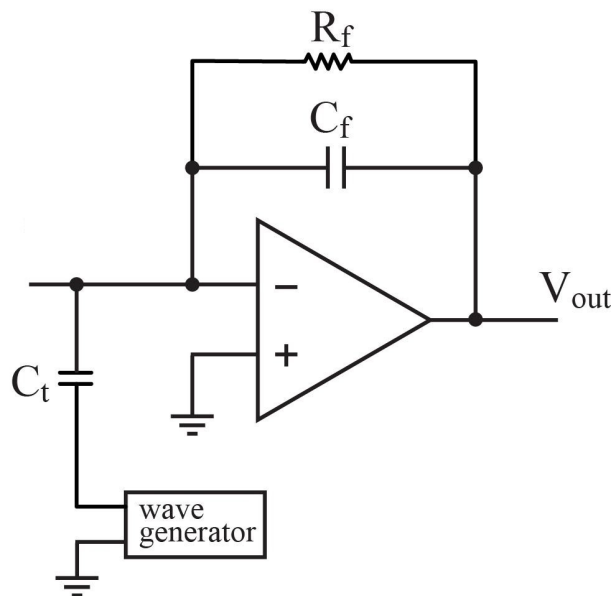


Figure 5.24: A capacitive coupling, through a test capacitance C_t , of an amplifier and a waveform generator: the easiest way to perform CSP test, in fact, is by injecting pulses to the pre-amplifier input with an electronic pulser or waveform generator. V_{out} it will then be input to the digitizer.

to provide a series of current spikes with alternating polarity: each time the square wave changes state, a brief current pulse is injected into or out of the CSP input through the test capacitor C_t . The amount of charge injected into the pre-amplifier input is the product of the test capacitance C_t and the peak to peak square wave voltage V_{pp} . V_{out} , as mentioned above, is the input for the digitizer. Hence, the amount of charge in input to digitizer is known and it is

$$Q = V_{pp} \cdot C_t \quad (5.3)$$

For the pre-amplifier calibration, the data taking procedure was therefore carried out as follows:

- 13 different acquisitions were made using the digitizer as the voltage V_{pp} varied, set by the waveform generator. In particular, a step waveform was used, the amplitude of which was observed under the oscilloscope.

- V_{pp} has been varied from 50 mV to 330 mV.
- Approximately 10,000 events were acquired for each run performed using the CoM-PASS software: in this way it was possible to acquire the distribution of the ADC peak values, recording the maximum value for each event in a root file. The peak values distribution for channel 0 of the digitizer is shown, as an example, in Figure 5.25: on the horizontal axis there is the output of the digitizer in $ADCcount$: for each run performed and for each channel, the average value of this distribution was considered.

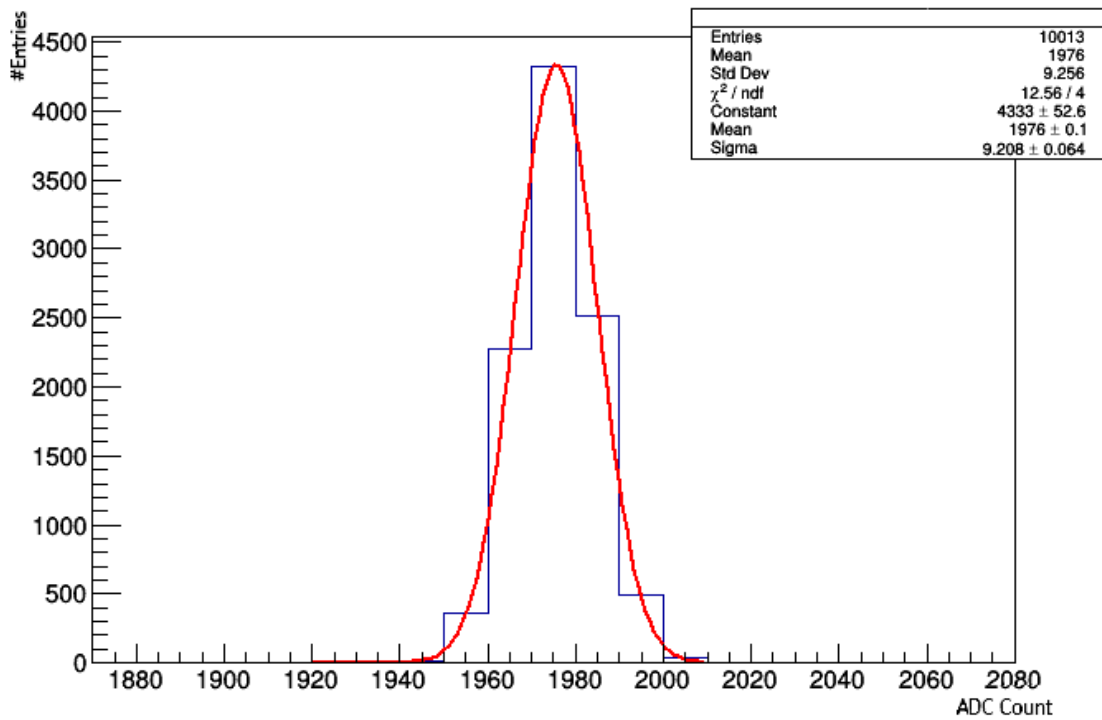


Figure 5.25: Peaks value distribution for channel 0 of the digitizer: on the horizontal axis there is the output of the digitizer in $ADCcount$: for each run performed and for each channel, the average value of this distribution was considered.

The average value of the peaks value distribution shown in Figure 5.25 can be converted into charge Q through a χ^2 fit using a linear model as following: the i - th value expressed in $ADCcount$ corresponds to the value $Q = p_1 \cdot i + p_0$. The p_0 and p_1 are respectively the intercept and the slope of the calibration curve. Hence, in Figures 5.26 and 5.27 the calibration curve are shown. On the horizontal axis there is the main value of the distribution peaks shown in Figure 5.25, on the vertical axis there is the charge in input of the pre-amplifier (see Equation 5.3).

To appreciate the effect of the procedure and its physical meaning, in the Figure 5.27 the correspondence between $ADCcount$ and charge Q in the case of the passage of a cosmic muon μ is shown as example. Supposing that the passage of a μ inside the detector produces 200 roughly primary e^- . Assuming that each GEM foil has a gain approximately equal to 20, we would obtain a charge corresponding to about 256 fC being $1fC = 4625 e^-$. This result would therefore represent the charge at the pre-amplifier input.

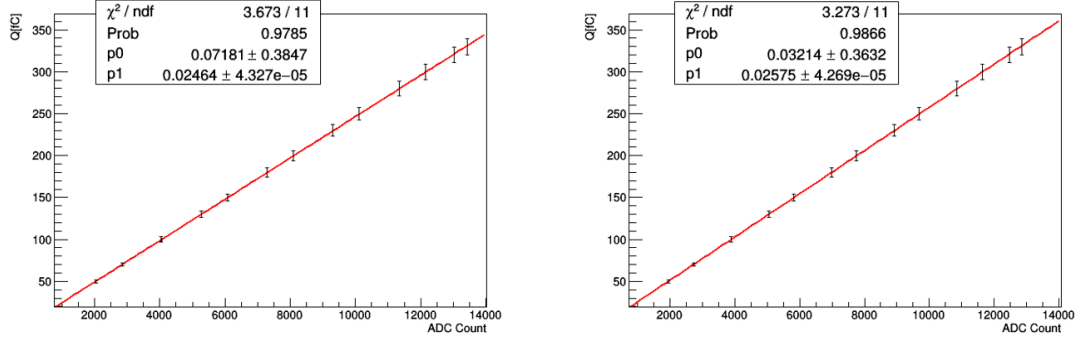


Figure 5.26: Left: calibration curve for channel 0 of the digitizer. Right: calibration curve for channel 1 of the digitizer. For both plots, on the horizontal there is the output values of digitizer expressed in ADCcount, on the vertical axis there is the charge in input of the pre-amplifier expressed in Equation 5.3.

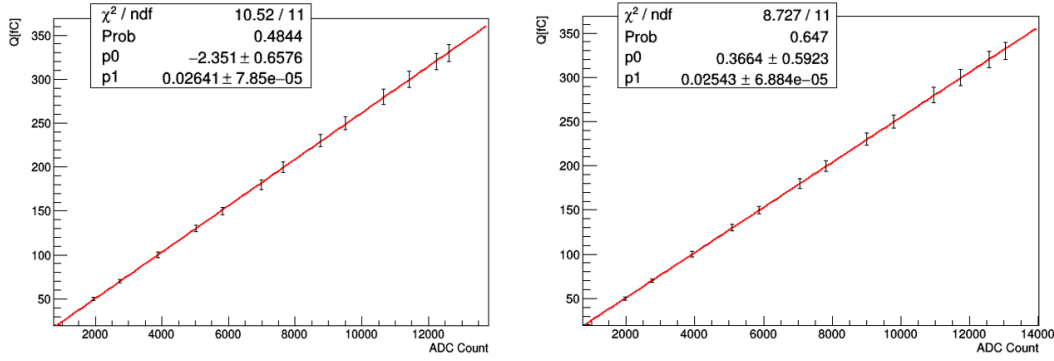


Figure 5.27: Left: calibration curve for channel 2 of the digitizer. Right: calibration curve for channel 3 of the digitizer. For both plots, on the horizontal axis there is the output values of digitizer expressed in ADCcount, on the vertical axis there is the charge in input of the pre-amplifier expressed in Equation 5.3.

5.7 Gain Curve of GE3 of the Triple-GEM detector prototype

Once the amplifier has been calibrated, it is possible to carry out the data acquisition procedure through the use of a digitizer, in order to build the gain curve for the GE3 of the Triple-GEM detector. The data taking procedure was therefore carried out as follows:

- Considering the diagram in Figure 5.18, the iron source was positioned on the 1C cell. One of the 4 channels of the detector read-out plane is located in correspondence with this cell. This channel has been conventionally associated with the channel 0 of the digitizer. Consequently, in the following, reference will be made to the output of this single channel.
- The values of ΔV_{GE1} , ΔV_{GE2} was set respectively equal to 390 V; the value of ΔV_{GE3} was varied from 355 V to 390 V.
- 8 measurement sets were carried out, approximately 40,000 events were acquired

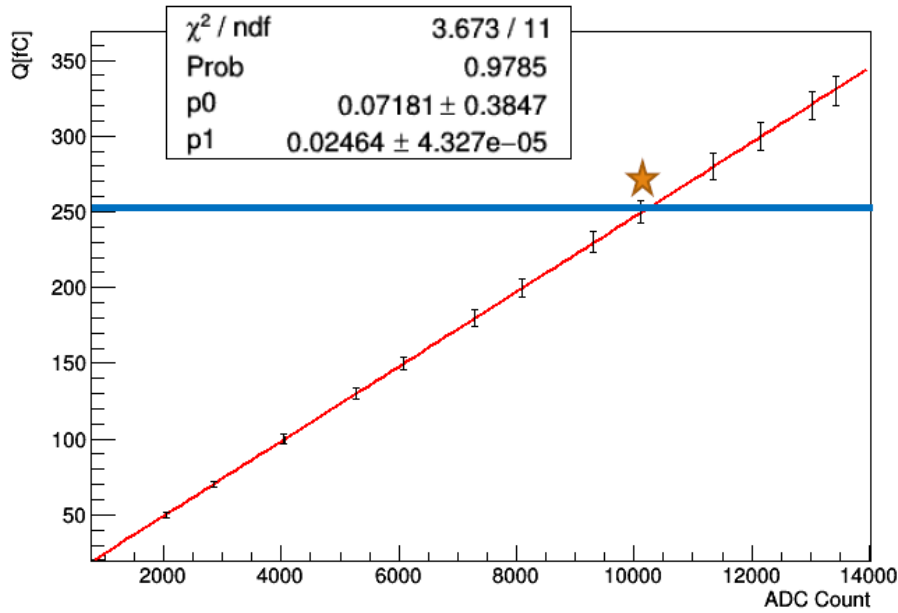


Figure 5.28: Correspondence between $\text{ADC}_{\text{count}}$ and charge Q in the case of the passage of a cosmic muon μ : supposing that the passage of μ inside the detector produces roughly 200 primary e^- and that each GEM foil has a gain equal to 20, we would obtain a charge corresponding to about 256 fC being $1\text{fC} = 4625 e^-$. This result would therefore represent the charge at the pre-amplifier input.

for each run performed, using the CoMPASS software.

The Figure 5.29 shows an example of the ^{55}Fe spectrum acquired using the CoMPASS software for the channel 0 of the digitizer. The main peak and the escape peak correspond respectively to 5.9 KeV and 2.9 KeV as shown in Section 5.2.

On the horizontal axis there is the output of the digitizer suitably converted by the parameters p_0 and p_1 of the calibration curve of the channel 0 shown in Figure 5.28. The conversion was made up through the Equation 5.3.

In order to obtain the gain curve for GE3, the average value of the main peak was obtained through a fit given by a sum of two Gaussian distributions. The procedure was performed for each run as the value of ΔV_{GE3} varies: in Figure 5.30 the charge Q as a function of the ΔV_{GE3} value is shown. An exponential fit was performed, the error of each charge value was considered equal to the σ of the distribution in the Figure 5.29.

As a cross check, the same gain curve was obtained considering the average value of the escape peak. This value correspond to the fit parameter p_1 of the fit in Figure 5.29. In Figure 5.31 the average values of the main peak distribution as function of ΔV_{GE3} .

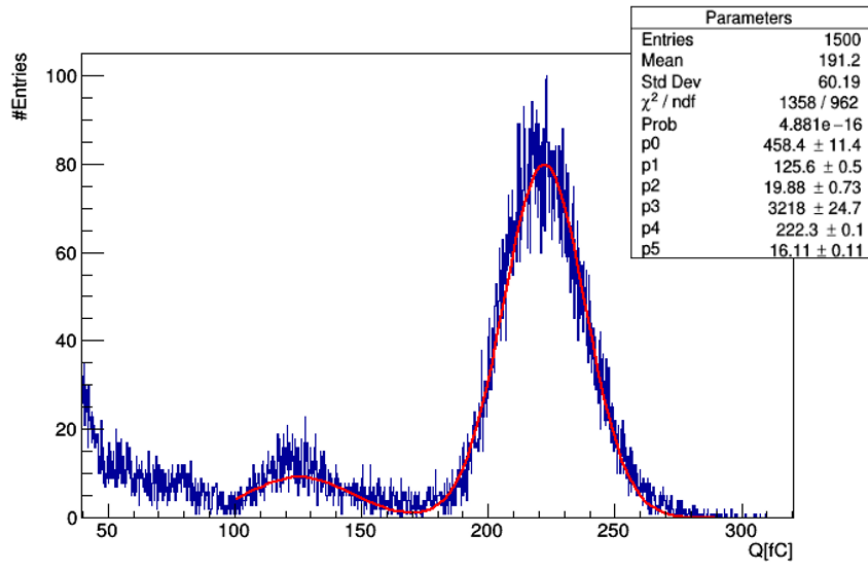


Figure 5.29: Emission spectrum of ^{55}Fe : on the horizontal axis there is the output of the digitizer suitably converted by the parameters p_0 and p_1 of the calibration curve of the channel 0 shown in Figure 5.28. The conversion was made up through the Equation 5.3.

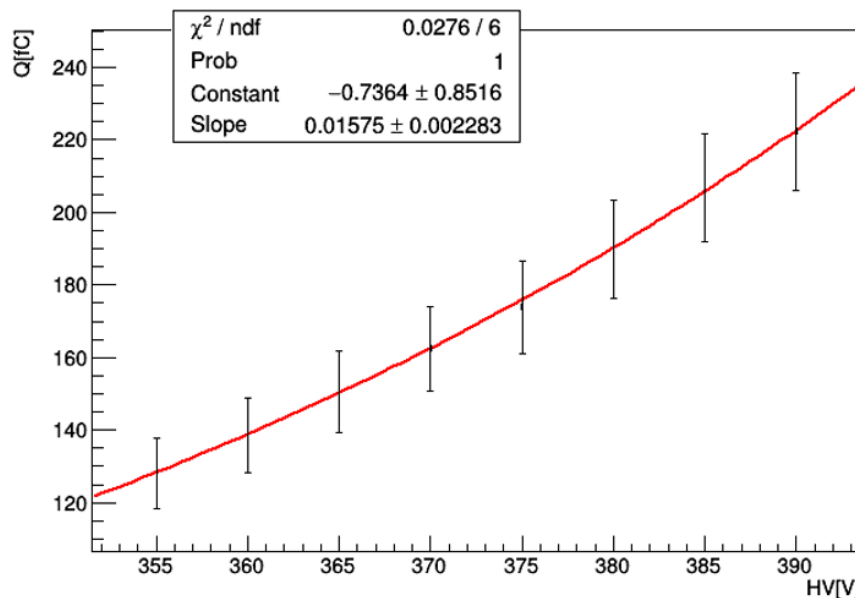


Figure 5.30: Charge Q as a function of the ΔV_{GE3} value: the average value of the main peak was obtained through a fit given by a sum of two Gaussian distributions. An exponential fit was performed, the error of each charge value was considered equal to the σ of the distribution in the Figure 5.29.

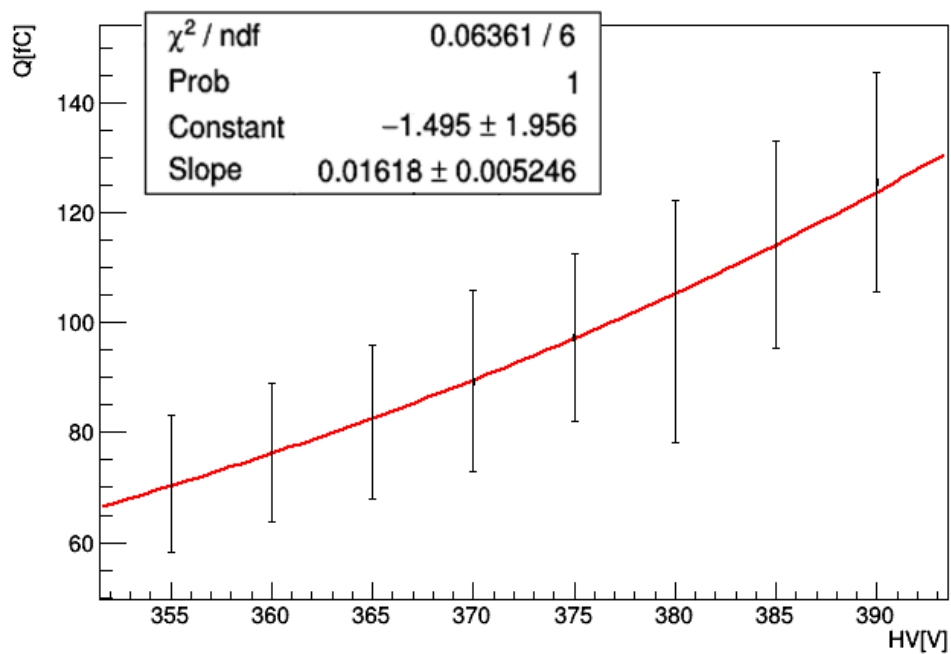


Figure 5.31: Charge Q as a function of the ΔV_{GE3} value: the average value of the escape peak was obtained through a fit given by a sum of two Gaussian distributions. An exponential fit was performed, the error of each charge value was considered equal to the σ of the distribution in the Figure 5.29.

Conclusion

During this thesis work a characterization of a Triple-GEM detector prototype for the CMS Muon System Upgrade was performed. The Triple-GEM detectors constitute a novel state-of-the-art technology that will require careful commissioning and dedicated studies. A precise monitoring of the currents through the three GEM foils in particular would allow an in-depth understanding of the gain of the chamber, and potentially allow to diagnose issues like electric discharges that might cause the chamber to malfunction. A suitable tool for carrying out such measurements is the multi-channel pico-ammeter named PICO. In order to perform precise current measurements suitable for optimizing the electric fields of the Triple-GEM detector in fact, it was necessary to fully characterize the pico-ammeter. The device is a high voltage voltmeter/pico-ammeter made of 7 independent channels and it is able to perform non-destructive measurements of voltage and current. Such measurements are correlated to the temperature of the ADCs present in PICO. Consequently, temperature corrective factors have been derived as well as the voltage and current resolution of the device. After having obtained the resolution values in current and in voltage for the pico-ammeter, it was possible to proceed with the characterization of the Triple-GEM prototype. This prototype has very similar characteristics to the Triple-GEM used by the CMS collaboration in the Muon System Upgrade, although the two detectors differ in size and for the read-out plane. The procedure for optimizing the electric fields inside the detector was then carried out using an iron source. In order to maximize the amount of electrons that are collected on the read-out electrode, it is crucial to choose the electric fields appropriately. In particular, the value of the electric field must allow for a good electron extraction efficiency from the lower electrode of the previous GEM foil. At the same time, the Electric Field must be sufficiently high to guarantee a good electron transfer efficiency towards the top electrode of the next GEM. Optimization of Electric Field for the areas of Transfer 1 and Transfer 2 was carried out using an iron source. Subsequently, the chamber gain and its uniformity were evaluated over the whole sensitive area of the Triple-GEM prototype, obtaining an average uniformity higher than 90% of the maximum value registered in the chamber. The information on the gain was also studied through the use of a digitizer, whose response was studied and its output in ADC count was converted into charge by performing a calibration procedure making use of a pre-amplifier, which allows to amplify the output charge of the Triple-GEM prototype. From the calibration curves it was therefore possible to convert the response of the digitizer into an electric charge and finally observe the spectrum of the iron source in order to obtain the gain curve for the third gem foil. Therefore, two gain curves, for the GE3 have been constructed starting respectively from the main and escape peak present in the emission spectrum of the iron source: the slope of the two curves is comparable within the errors. This work has allowed to carefully characterize Triple-GEM in standard work-

ing conditions, and is the first step towards in-depth studies of the chamber resolution, electron-ion recombination measurements, and studies of potential discharges. Future developments could allow to use the pico-ammeter to promptly identify discharges in the chamber, acting as a veritable discharge-precursor, and ensure stable operating conditions for Triple-GEM chambers also in the more challenging HL-LHC environment.

Bibliography

- [1] *The CMS tracker: addendum to the Technical Design Report*. Technical design report. CMS. CERN, Geneva, 2000.
- [2] *The CMS electromagnetic calorimeter project: Technical Design Report*. Technical design report. CMS. CERN, Geneva, 1997.
- [3] CERN Burkhard Schmidt. The High-Luminosity upgrade of the LHC . *Conference Series 706(2016) 022002*, 3, 2015. Also published by CERN Geneva in 2010.
- [4] Priyanka Kumari. Improved-rpc for the cms muon system upgrade for the hl-lhc, 2020.
- [5] D. Abbaneo, M. Abbrescia, P. Aspell, S. Bianco, K. Hoepfner, M. Hohlmann, M. Maggi, G. De Lentdecker, A. Safonov, A. Sharma, and M. Tytgat. A gem detector system for an upgrade of the high-eta muon endcap stations ge1/1 + me1/1 in cms, 2012.
- [6] Stephen D. Butalla and Marcus Hohlmann. Electronics integration for the ge2/1 and me0 gem detector systems for the cms phase-2 muon system upgrade, 2021.
- [7] Yasser Assran and Archana Sharma. Transport properties of operational gas mixtures used at lhc, 2011.
- [8] S Chatterjee, S Roy, A Sen, S Chakraborty, S Das, S K Ghosh, S K Prasad, S Raha, and S Biswas. Long term stability study of triple gem detector using different argon based gas mixtures: an update, 2021.
- [9] A. Amoroso, R. Baldini Ferroli, I. Balossino, M. Bertani, D. Bettoni, A. Bortone, A. Calcaterra, S. Cerioni, W. Cheng, G. Cibinetto, and et al. Time performance of a triple-gem detector at high rate. *Journal of Instrumentation*, 15(06):P06013–P06013, Jun 2020.
- [10] A. Amoroso, R. Baldini Ferroli, I. Balossino, M. Bertani, D. Bettoni, A. Bortone, A. Calcaterra, S. Cerioni, W. Cheng, G. Cibinetto, and et al. Time performance of a triple-gem detector at high rate. *Journal of Instrumentation*, 15(06):P06013–P06013, Jun 2020.
- [11] M. Abbas, M. Abbrescia, H. Abdalla, A. Abdelalim, S. AbuZeid, A. Agapitos, A. Ahmad, A. Ahmed, W. Ahmed, C. Aimè, C. Aruta, I. Asghar, P. Aspell, C. Avila, J. Babbar, Y. Ban, R. Band, and at al.l. Performance of a triple-gem demonstrator in *pp* collisions at the cms detector, 2021.

[12] <https://www.caen.it/products/a1515b/>.

[13] <https://www.caen.it/products/dt5725/>.

[14] <https://www.caen.it/products/compass/>.